Towards a Predictive Understanding of Hematite Crystallization in the Solution

Guomin Zhu

A dissertation

submitted in partial fulfillment of the

requirements for the degree of

Doctor of Philosophy

University of Washington

2020

Reading Committee:

James De Yoreo, Chair

Brandi Cossairt

Lucien Brush

Program Authorized to Offer Degree:

Materials Science and Engineering

University of Washington

Abstract

Towards a Predictive Understanding of Hematite Crystallization in the Solution

Guomin Zhu

Chair of the Supervisory Committee:
Professor Dr. James J De Yoreo
Department of Materials Science and Engineering

Crystallization by particle attachment (CPA) is a common mechanism of colloidal crystallization resulting in hierarchical morphologies[1-4]. It has been exploited to create nanomaterials with unique, emergent properties[4-6] and implicated in the development of complex mineral textures[1, 7]. Oriented attachment (OA)[7-8], a form of CPA in which crystalline primary particles align and attach along specific crystallographic directions, produces structures (typically referred to as mesocrystals) that diffract like single crystals, even though the constituent particle domains are still discernable[2, 9]. While the existence of mesocrystals has been well documented in a wide range of crystal systems[1-9] and individual particle attachment events have been directly visualized[10], the mechanism by which these seemingly random events lead to well-defined, self-similar morphologies remains a mystery, as does the role of organic ligands, which are ubiquitous in nanoparticle systems[3, 9, 11].

In chapter 1, we discussed the difference between classic nucleation and growth vs. crystallization by particle attachment. Among the crystallization by particle attachment, we highlighted the pathway of mesocrystal formation and oriented attachment. We laid out different views on mesocrystal formation in the literature. We briefly introduced in situ liquid phase TEM as an important technique in revealing the mechanism in various fields.

In chapter 2, we focused on the crystallization of hematite (Hm, Fe_2O_3) from ferrihydrite (Fh) as an example to understand the formation mechanism of mesocrystal and role of starting phase. Multiple techniques, primarily TEM, have been applied to understand the crystallization mechanism. We applied ex-TEM to characterize the Hm formation, the results of which are verified by cryo-TEM on the crystallization process. The Hm mesocrystal has a spindle shape consisting of nm sized primary particles that are atomically aligned, as observed by HRTEM, HRSTEM, cross section HRTEM, and 3D STEM tomography. We developed a freeze-and-look approach using indexed TEM grids to cycle samples between the growth reactor and the TEM in order to track the pathway of crystallization at identical positions over time. We found that Hm grows into the solution with a half-spindle shape suggesting that Hm is growing from the solution, and Fh is dissolving to supply the solutes. Most importantly, we applied in situ liquid phase TEM (LP-TEM) at 80°C to visualize the crystallization process. We found that Fh is dissolving and Hm grows by nucleation of new-born particles a few nanometers away from Hm/solution interface, and then attach to the surface. Based on ATR-FTIR measurements of the relative binding strength of oxalate to the (001) and (012) faces, and calculations of chemical potential gradients near the interface, we proposed that oxalate plays the role of inhibiting classical monomer-by-monomer growth of the hematite particles while promoting the nucleation of new hm particles close to the hm/solution interface.

In chapter 3, we discussed several limitations that face the powerful LP-TEM technique which includes beam induced particle dissolution and motion, particle-membrane adhesion, contamination, triggering of reaction and replication difficulties. We described our efforts to address these challenges by modifying solution and interface chemistry, changing beam parameters, maintaining solution flow, performing post *in situ* analyses and applying controlled heating. We believe overcoming these limitations will largely empower the technique in many fields.

In chapter 4, we listed two examples of applying in situ TEM to investigate dissolution and deformation properties of Hm materials. Further structure characterization of the Hm structure were rationalized to their dissolution and deformation properties.

Chapter 5 is the summary of the thesis, along with my vision of utilizing and developing in situ methods to explore the synthesis-structure-property relationship of materials.

TABLE OF CONTENTS

LIST OF FIGURES

LIST OF TABLES

Glossary

Hm: hematite

Fh: ferrihydrite

Ox: oxalate

SiN: silicon nitride

TEM: transmission electron microscopy

HRTEM: high resolution transmission electron microscopy

STEM: scanning transmission electron microscopy

LP-TEM: liquid phase transmission electron microscopy

SAED: selected area electron diffraction

EDX: energy dispersive X-ray

HAADF: high angle annular dark filed

AFM: atomic force microscopy

ATR: attenuated total reflection

FTIR: Fourier-transform infrared spectroscopy

CPA: crystallization by particle attachment

OA: oriented attachment

PSS: polystyrene sulfonate

Rhom Hm: rhombohedral hematite

PH: potential of hydrogen

DFT: density function theory

CDFT: classic density function theory

EG: ethylene glycol

CTAB: cetyl trimethyl ammonium bromide

SSP: synthesis-structure-property

Disclaimer

Some passages have been quoted verbatim from the following sources:

1. **Zhu, G.,** Sushko, M., Loring, J., Legg, B., Song, M., Solits, J., Huang, X. P., Rosso, K. , de Yoreo, J., 2020, ***Nature***, in press.
2. **ZHU, G.,,** Reiner, H., Cölfen, H. and De Yoreo, J.J., 2019. Addressing some of the technical challenges associated with liquid phase S/TEM studies of particle nucleation, growth and assembly. *Micron*, *118*, pp.35-42.

ACKNOWLEDGEMENTS

I am deeply thankful for all the small things in the past years. It has been an incredible journey intellectually and joyfully. There are many people that have supported my work and study, and have made my life easier, that I won't able to list all of them. I appreciate all of you!

Special thanks to my advisor, Professor James J de Yoreo. His devotion to science, sharp insights and enormous knowledge has been inspiring me from the beginning and will keep motivating me in the future. I am also particularly impressed by his tremendous support and patient guidance to his students. He is the best advisor that I know of and is a role model that I aspire to be. Also thankful to my committee members, Professor Peter J. Pauzauskie, Professor Lucien Brush and Professor Brandi M. Cossairt. Thank you for their time and valuable comments.

I am especially grateful for my colleagues including my group members and collaborators. They have provided lots of advice, guidance and support on my research. I will always be grateful to have the privilege to spend my PhD time both at UW and PNNL. Both are incredible institutions where I have met inspiring friends, professors and scholars. Their humble and open-minded attitudes have deeply shaped my view towards science and life.

I want to thank my parents for their deep love and support for my decision to study abroad. I can do nothing to match their love for me. Finally, I want to thank my best friend, Qiu. Knowing her has transformed my life and meeting her is the luckiest thing ever.

DEDICATION

To my family

Chapter 1. Narrative

1.1 Vision and significance

Materials with hierarchical nanostructures have wide applications in many different fields including catalysis, electronics and energy related fields. The mechanisms by which these hierarchical materials form are poorly understood and highly debated. In the classic vision of nucleation and growth, crystals nucleate and grow through monomer-by-monomer attachment. However, more and more evidence are showing that in many systems, crystallization could occur via attachment of a whole range of species more complex than simple ions. Due to the complex nature of the crystallization process, which could simultaneously involve both classical and nonclassical pathways, it becomes difficult to relate synthesis conditions to the final crystal, preventing the ability to predictively control the growth and properties of the final crystal. The goal of my PhD project is to establish a general method to investigate the crystallization pathway and understand the non classic crystallization at atomic or nanoscale level. The knowledge gained from this project will facilitate the establishment of a solid framework for the atomic understanding of nonclassical crystallization pathways, and eventually lead to predictive and controlled syntheses of those hierarchical nanostructures.

1.2 Introduction

1.2.1 *Classic nucleation and growth*

Crystallization from a liquid solution is a phenomenon widely observed in biological organisms, the geochemical environments, and industrial fields. It has been an area of active research for centuries. Many crystals of biologic and industrial importance, such as $CaCO_3$, $CaPO_4$,

Fe_2O_3, TiO_2, and ZnO, have been widely investigated[1, 12-13]. A general picture of crystallization from a nucleation event followed by monomeric growth has been developed in which supersaturation of the solution could drive the phase separation, leading to a lower total Gibbs energy. Nucleation is seen as a stochastic event and its simplified energy relationship is described by Eq. 1

$$\Delta G = \Delta G_S + \Delta G_V = 4\pi r^2\sigma + \frac{4}{3}\pi r^3 \Delta g$$

in which the combination interfacial free energy (ΔG_S) and the bulk energy (ΔG_V) governs nucleation events. Δg is the difference of free energy per volume of the supersaturated solution and the bulk crystal, and r is the radius of the crystal and σ is the interfacial free energy. This equation is depicted as a function of reaction progress in Figure 1.1, [14] In the classical nucleation picture there is a barrier due to the interfacial free energy that must be overcome. There are several aspects critical to the nucleation events, e.g. supersaturation, size-dependent interfacial energy, temperature and kinetic factors [15]. Nucleation has been extensively studied with in situ techniques including x-ray, optical, and atomic force microscopy (AFM)[16-17]. However, nucleation events are sensitive to the technique used to detect them and predicting them is an intrinsically challenging problem of coupled length and time scales.

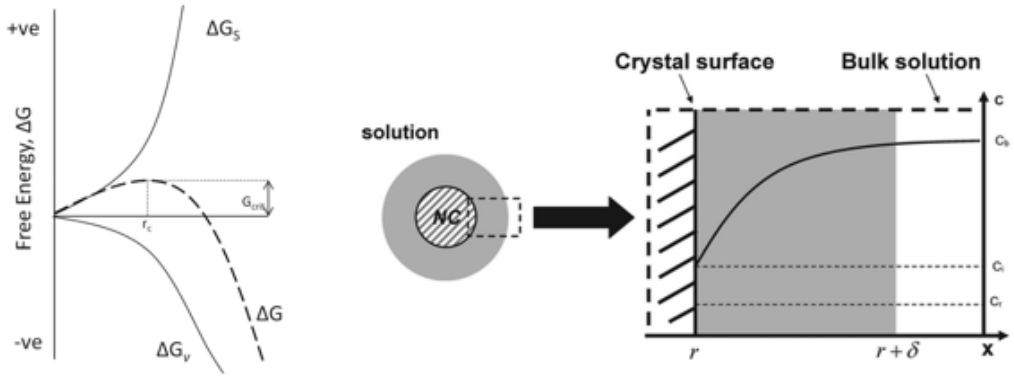

Figure 1.1. Schematic of nucleation barrier accounting for the existence of critical nuclei size (left) and schematic of a post-nucleation growth, in which monomer distribution along the nuclei surface to the bulk solution due to the diffusion from the bulk to the nuclei surface (right). [14]

Nucleation occurs in bulk solutions, at solid-solution interfaces, or inside the solid. Determining the exact location of a nucleation event is challenging but as it mainly indicates the interfacial free energy of the system, which would guide the pathway for further growth. In the case of amorphous-phase-mediated crystallization, nucleation may occur in the bulk solution, in the bulk amorphous phase or on the amorphous phase/solution interface. Nielsen et al.[12] have used liquid cell TEM to reveal the direct and indirect pathways of the nucleation and growth of $CaCO_3$, however, in the case of indirect crystallization, the location of the first nuclei is still a mystery due to the limit of the resolution during the in situ experiments. Work by Ihli et al.[18] reports that that due to the high activation energy, crystallization from amorphous $CaCO_3$ occurs by partial dissolution/recrystallization, mediated by surface water, followed by further particle crystallization by a solid-state transformation. There are numerous ex situ observations of secondary phases in contact with primary crystalline phases and Nielsen et al., [12] reported one instance of calcite crystallizing directly from aragonite.

During classical crystal growth, the nuclei will act as a sink and start to deplete the "nutrients" from the solution, and a diffusion of the nutrients from the bulk solution to the nuclei is expected.

Particle facets are developed by step formation on the crystal surface, where the incoming monomer species diffuse until they reach a location that is thermodynamically or kinetically favorable. The detailed process may be very dynamic and include multiple monomer dissociation and adsorption steps. Coarsening, in which small particles dissolve whereas bigger particles grow, is a major classical growth mechanism that can be quantitatively described due to the difference of solubility based on the Gibbs-Thompson law [15].

The presence of a metastable phase, whether amorphous or crystalline, in the reaction solution may change those views towards crystallization in many different ways. First, for Fh, a poorly crystallized phase, the structure of which is debated [19], let alone their surface structure in the aqueous solution, which might be very unique. Second, the different interfaces present in solution-mediated vs. primary-phase-mediated growth may affect nutrient diffusion. Diffusion at solid-solution interfaces is an area of extensive and ongoing research but very few is known. The interface between the crystallized nuclei and the amorphous phase may also play a major role in the crystallization pathway, but there is currently no clear physical description of this interface. Finally, the local chemical environment may be significantly influenced due to the presence of an amorphous phase and, sometimes, organic additives, both because solutions are structured, and ions segregated near interfaces and because surface charge can impact local ion activities and pH. The primary phase will likely act as a buffer and keep the driving force stable during the reaction. However, due to the aggregated nature of different phases, they may undergo a solid-state-like or extremely localized phase transformation. There is also a possibility that phase transformation is driven starting from the hydrated surface layer. In an example reminiscent of coarsening, Nielsen et al. [12] showed the transformation of Amorphous Calcium Carbonate (ACC) to vaterite in which the newly formed vaterite acted as a sponge and grew at the cost of the ACC.

1.2.2 *Crystallization by particle attachment (CPA)*

In spite of the successes of classical nucleation and growth models [15, 20], there are lots of phenomena associated with crystallization that cannot satisfactorily be explained or predicted either quantitatively or qualitatively. For example, amorphous phases are found to nucleate at a supersaturation well below those predicted by classical nucleation models [21]. Sea urchin embryonic spicules crystallize through accumulation of nanoparticles of an amorphous calcium carbonate (ACC) precursor, and then transforms into a calcite crystal through probably solid phase transformation [22-23]. Similar amorphous-to-crystalline pathways are also reported in many other biominerals [24-26]. More and more evidence are showing that in many systems, crystallization could occur via attachment of a whole range of species more complex than simple ions (monomer), as shown in Figure 1.2. These pathways can involve many intermediate particles, whether crystalline, amorphous, dynamic poly-nuclear clusters or small oligomeric species, that can aggregate in some specific way to lead to the final alignment of the crystal. When those intermediates comprise metastable phases which are usually kinetically stabilized, they can eventually transform to the thermodynamically stable phase. The pathway between the kinetically stable phase and the thermodynamically stable phase is still vigorously debated in the literature[1, 27]. It is worth pointing out that several growth pathways could simultaneously participate in the growth, and the extent to which each pathway plays a role in crystal growth could vary by changing experimental parameters like temperature, concentration or additives. This makes it difficult to gain a predictive understanding of crystallization mechanisms.

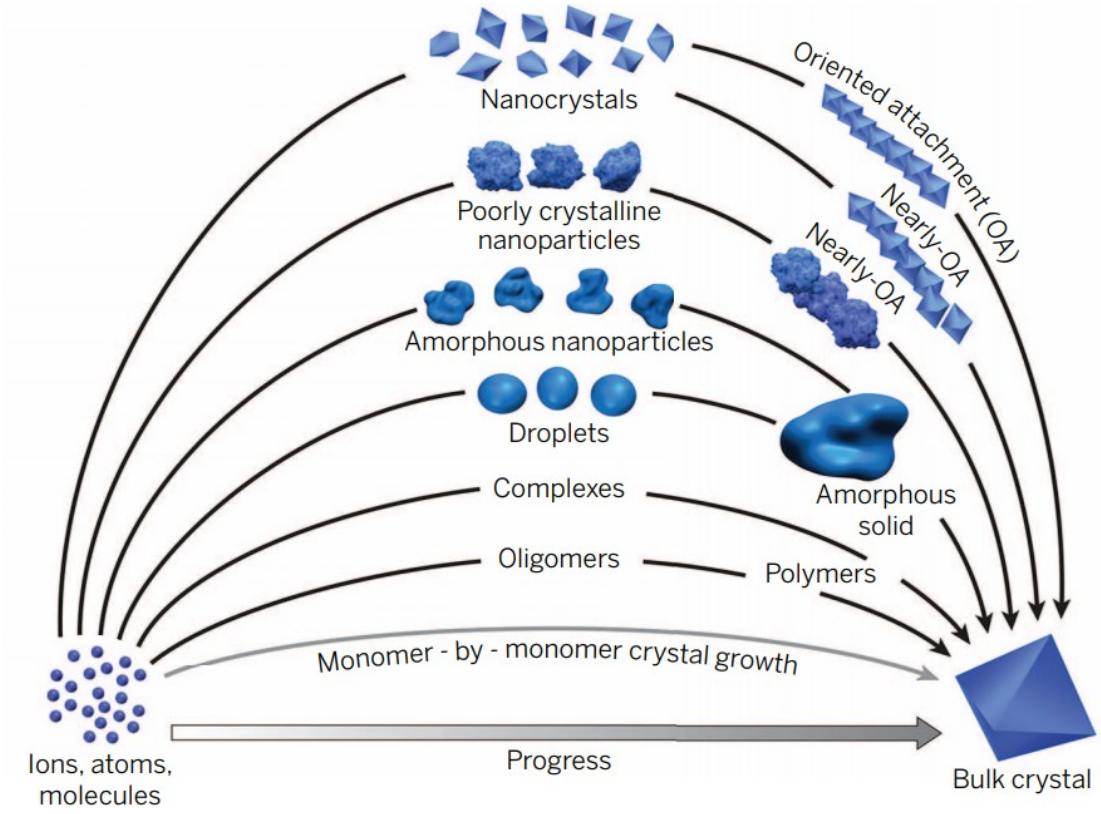

Figure 1.2. Multiple Pathways to crystallization involving particle attachment. Compared to monomer-by-monomer addition as envisioned in classical models of crystal growth (gray curve), CPA occurs by the addition of higher-order species ranging from multi-ion complexes to fully formed nanocrystals. (The final faceted bulk crystal is a schematic representation of a final single-crystal state. [1] Worth noting that several different pathways could coexist in a specific system depending on the system.

1.2.3 *Oriented attachment and mesocrystal*

Among these different pathway as shown in the Figure 1.2, one enormously important process is called oriented attachment (OA), which was first proposed twenty years ago to explain TiO_2 chain-like structures[28]. They hypothesize that particles move in the solution via Brownian motion before the distance between particles reach to certain region and particles attach to each other and form crystal which preserve the primary particle features, as shown in the schematic below (Figure 1.3). Soon after that, various materials with hierarchical structure have been synthesized based on the OA mechanism [10]. The significance of this process lies both in the unique properties that resulting

nanostructures possess, as well as the implications for understanding biological and geochemical phenomena[1]. Usually those material systems have a particle aggregated features, and with many similar-sized domains. These materials commonly have monocrystalline features with electron diffraction spot elongated due to the slight misalignment of domains.

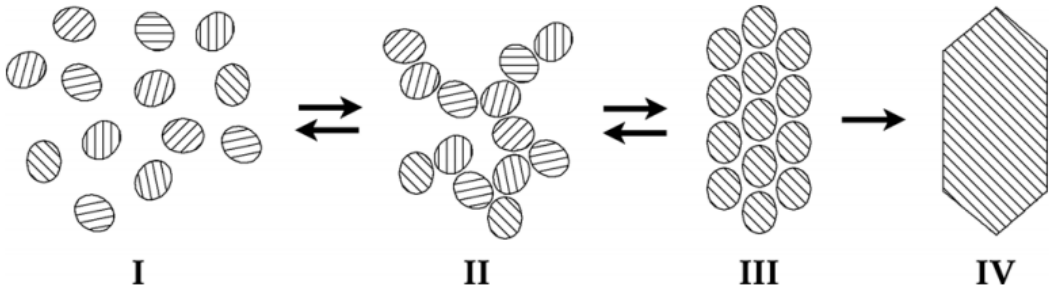

Figure 1.3. Schematic illustrating the process of oriented attachment in the solution. Primary particles (I) reversibly form loose assemblies (II) analogous to outer sphere complexes. Particles in the random assembly rotate and rearrange via Brownian motion until crystallographic alignment is reached (III). The particles can then irreversibly attach to form a continuous crystal (IV). [29] the attachment won't necessarily lead to a crystal with smooth surface as illustrated in IV.

A good example of the system that forms through OA is shown in Figure 1.4 where PbSe nanocrystals aggregated on the liquid/air interface to form a 2D honeycomb superlattices that are atomically coherent over a long physical scale, which is revealed by HAADF-STEM imaging and electron diffraction. It is worth noting that many literatures have over claimed OA mechanism simply by examining the ex-situ structure of the crystal, which can also be formed by classic growth arguments. So in situ methods, such as liquid phase TEM is emerging as critical method in determining the crystallization pathway [12, 30]. Dongsheng Li and coworkers directly observed the details of the attachment process between two particles in the liquid phase environment [10].

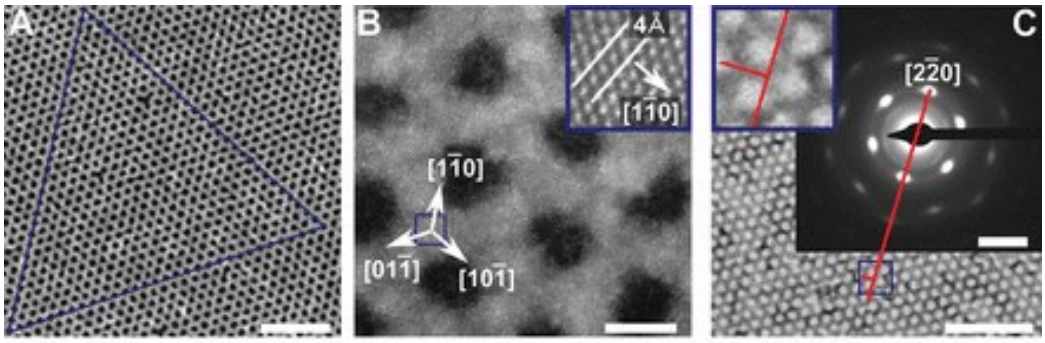

Figure 1.4. Formation of Single-crystalline PbSe honeycomb structures through oriented attachment.(A) HAADF-STEM image of the honeycomb structure. The PbSe nanoparticles are bright again the dark background. The equilateral triangle shows the long-range ordering of the structure. Scale bar, 50 nm. (B) High-resolution HAADF-STEM image showing that the <111> NC axes are perpendicular to the honeycomb plane. (Inset) Zoom-in on the atomic columns indicated by the blue box. Scale bar, 5 nm. (C) ED pattern showing the high degree of crystallinity. TEM image in the background shows the area on which the ED pattern was recorded Red line and inset show the orientation of the diffraction spots with respect to the honeycomb structure. Scale bars, 50 nm (TEM); 5 nm^{-1} (ED).[6]

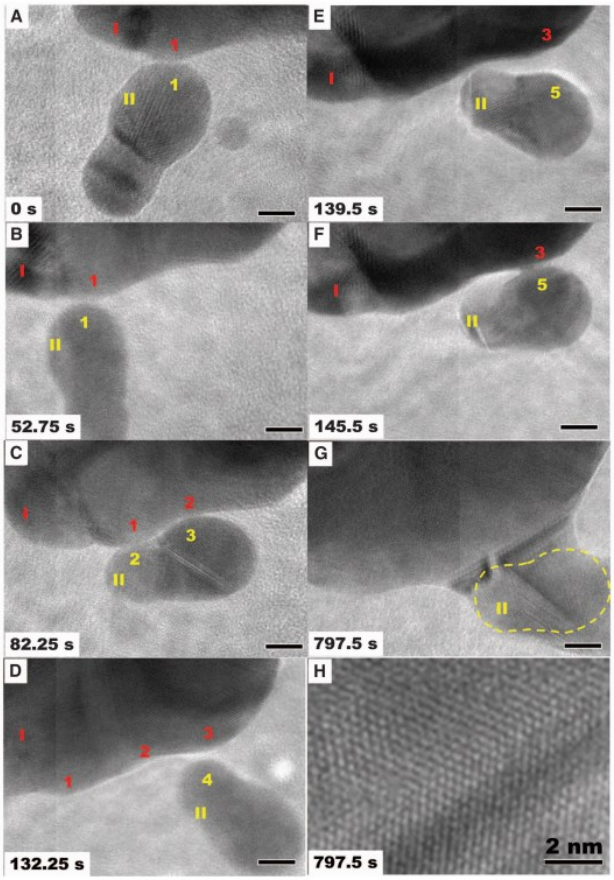

Figure 1.5. (A to G) Sequence of images highlighting typical event of particle attachment process. The surfaces of particles I and II made transient contact at many points and orientations (points 1-

1, 1-2, 2-3, and 3-4) before finally attaching and growing together (points 3-5). (H) High-resolution TEM image of the interface in (G) showing twin structure). The yellow dashed line in (G) shows the original boundary of the attached particle. Scale bars are 5 nm for (A) to (G).[10]

A mesocrystal is defined as "a nanostructured material with a defined long-range order on the atomic scale (in at least one direction), which can be inferred from the existence of an essentially sharp wide angle diffraction pattern (with sharp Bragg peaks) together with clear evidence that the material consists of individual nanoparticle building units" by Cölfen et al[31]. There are several different formation mechanisms proposed to form mesocrystal as shown below, including OA. In many cases, a metastable phase forms first before the formation of mesocrystal, which is probably due to the lower nucleation barrier of the metastable phase. We will address the role of this metastable phase later in our work.

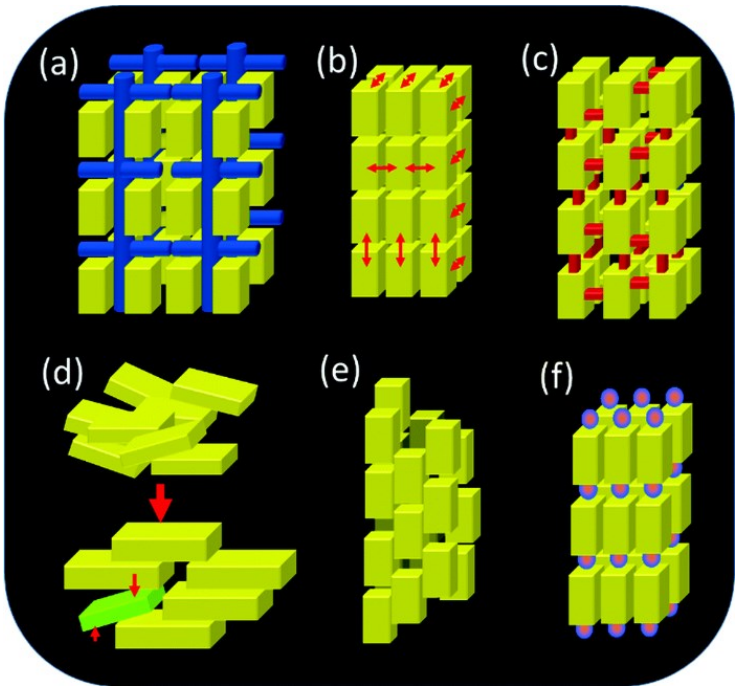

Figure 1.6. Different hypothesized formation mechanisms of mesocrystals. (a) Alignment by the organic matrix; blue lines are the organic matrix (b) alignment by physical forces, (c) crystalline bridges, epitaxial growth and secondary nucleation, (d) alignment by spatial constraints, (e) alignment by oriented attachment (no organic molecules between particles here), (f) and alignment by face selective molecules.[31]

1.2.4 *Classic arguments regarding mesocrystal crystallization*

"Mesocrystal" has been widely used to describe crystals that exhibit nanoparticle substructures, and the formation mechanism is described in the previous chapter involving particle attachment [9, 31]. However, classic arguments have also been applied to account for the formation of similar structure. Kim, et al [32] found that the formation of mesocrystal-like Calcite/polymer without evidence for the assembly of crystalline particles. A schematic in Figure 1.7 shows that a previously proposed mechanism based on oriented attachment, might results from surface roughening without particle attachment. It is worth noting that the nanoparticle morphology of calcite/polymer crystal in this work is only on the surface, but not inside the crystal. So it only looks like a mesocrytal from the outside.

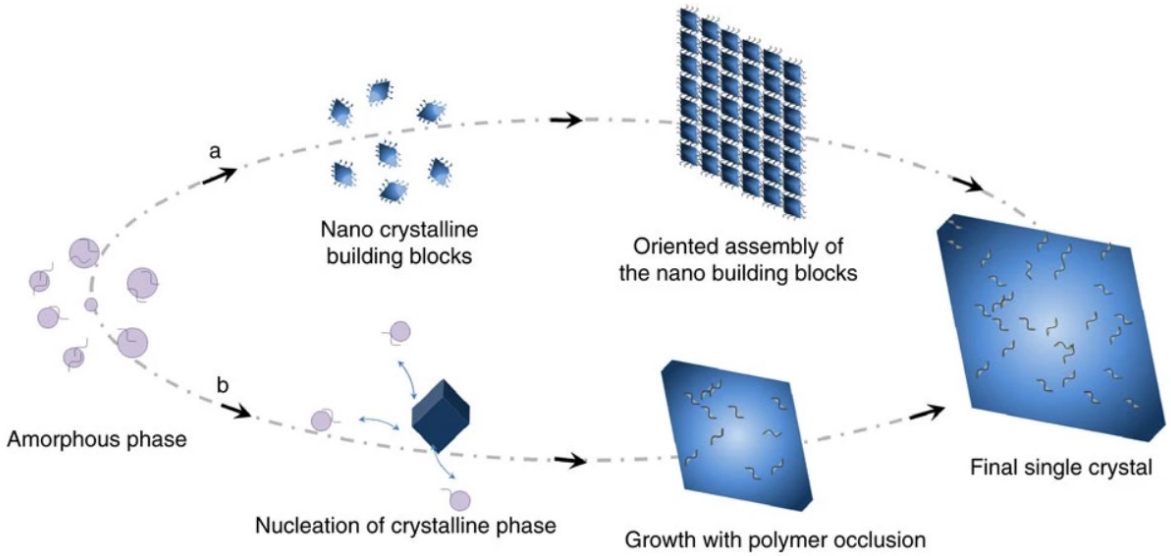

Figure 1.7. (a) The original mechanism proposed to lead to calcite mesocrystal formation, based on formation of nano crystalline nanoparticles first, and then the oriented assembly of crystalline nanoparticles; and (b) the mechanism demonstrated in this paper, where a calcite rhombohedron initially forms, and subsequent growth in the presence of polymer results in a modified morphology and a rough, particulate surface.[32]

Another study by Smeets et al [33] found that by introducing polystyrene sulfonate (PSS) into the system, the $CaCO_3$ started to have particle like features on the surface through stabilization of

new step directions and coupled with surface roughening. As shown in Figure 1.8a, the calcite growth is dominated by spiral growth in the beginning without PSS. After introduction PSS into the system, the surface starts to become roughening and turn to a structure similar to mesocrystal, which is highlighted by a series of AFM images in Figure 1.8c. It is worth noting that the structure presented only looks like mesocrystal from outside. The structure from the inside is not known. Both studies suggest that mesocrystal like structure could form from classic arguments like step pinning and surface roughening. However, the final structure only looks like mesocrystal from the surface. so still there are disputes regarding the formation mechanism of mesocrystal. But it surely suggests that relying on the ex-situ morphology is not be a good way to conclude the growth mechanism. In situ studies are needed to reveal crystallization pathway.

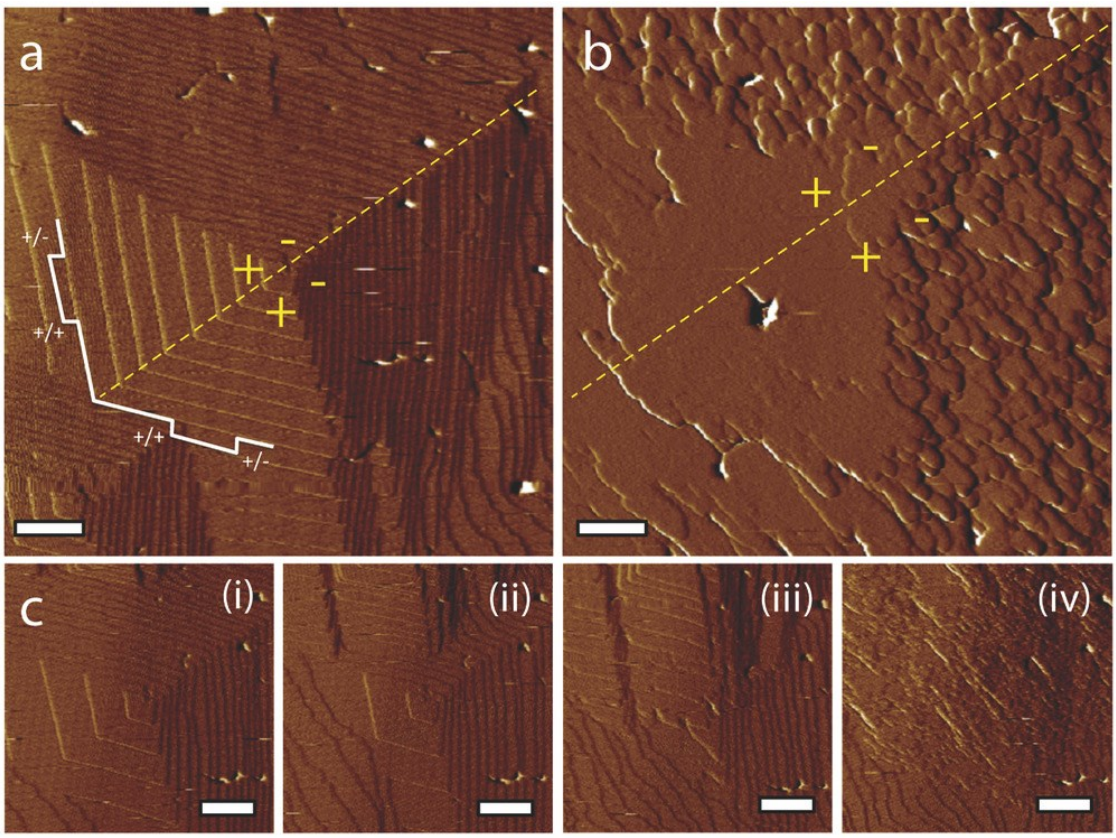

Figure 1.8. Calcite growth modified by adding PSS. a) In situ AFM image of a calcite growth spiral obtained. The c-glide plane is indicated by the yellow dashed line. The minus and plus sign

correspond to the acute and obtuse step directions, respectively, in yellow. b) In situ AFM image of the morphologically modified growth spiral obtained after flowing supersaturated solution (σ_{calc} = 1.70) containing 0.1 g L^{-1} PSS at 0.1 mL min^{-1}. c) Series of in situ AFM images (i–iv), for which influx of the PSS-containing solution begins between images (i) and (ii), showing modifications to obtuse and acute steps (i–iii). By image (iii), the stabilization of pseudo-[001] steps is evident and, by image (iv), the extreme pinning of the acute steps and roughening of the growth surface are shown. Scale bars in (a)–(c) are 500 nm. [33]

1.3 In situ liquid phase TEM

Optical microscopy was invented to overcome the limitation of human eyes and enable us to see micro sized objects, however optical microscopy has resolution limit due to diffraction. Transmission electron microscopy (TEM) overcomes the limitations of spatial resolution in optical microscopy, as electrons have much shorter wavelengths than visible light. The concept of electron microscopy was proposed by Knoll and Ruska in 1932 [34], and the first electron microscope was later built up by Knoll and his group applying an electron beam as the illumination source instead of light. Today TEM is arguably the most efficient and versatile tool for the characterization of materials over spatial ranges of a few atoms to the micrometer scale. The extreme resolution can even go down to sub angstrom, which is well below that of even the highest -resolution light microscopy (about 20nm). It is a powerful and dynamic technique that provides structural and elemental information about the materials. It is widely applied in materials science, chemistry, physics, biology, etc. [13, 35]

In situ TEM utilizes various in situ holders in the TEM to apply external stimulus such as temperature, gas environment, liquid environment, stress, electric or magnetic field to the materials, which enables direct observation of the physical behavior of material under these stimuli [36-38]. Compared to ex-situ methods, in situ TEM can provide fundamental insights into atomic or nanoscale phenomena. It is very ideal to illustrate the structure-property relationship of materials through combination of characterizing the structure (TEM) and examining its properties (applying

stimuli). Due to the recent development of novel technology in semiconductor, many new devices have been integrated into in situ TEM paradigm[37].

In situ liquid phase TEM (LPTEM), among them, is a rapidly flourishing technique developed to image samples in the liquid [39-40] , which is not possible using conventional TEM due to the incompatibility of maintaining a liquid environment under the vacuum conditon. The difficulty of imaging water and other liquids was recognized from the earliest times during the development of TEM. The challenge was to separate the liquid from the high vacuum in the microscope while achieving a controlled liquid layer which will allow premium resolution. Modern semiconductor technology enables a typical fluid cell that has a nm-scale thick water layer sandwiched between Si wafers, which include electron transparent SiN windows separated by a nanometer thick spacer. The spacer may be a solid layer with a channel, or spherical particles. The cell is sealed by either O-ring, glued or water-bonded to make it compatible with the high vacuum of the electron microscope. Many exciting studies have been pursued in a wide range of fields, including nucleation and growth of crystals[41], etching [42-44], particle assembly and fusion [45-47], bubble formation and dynamics [48-49], electrochemistry [50-51], and biomolecule interactions [52-53]. Numerous results have been reported to illustrate the dynamics and pathways that are unachievable by using other techniques[40]. Continuing efforts on equipment and technique are allowing materials and processes to be studied under different stimuli such as heating, gas/liquid mixture, or in magnetic or electric fields.

Figure 1.9 is a schematic of the liquid cell chamber for the LP-TEM and its application for imaging phenomena in materials science, life science and physics.[54] The liquid is enclosed between the windows. TEM relies on electron beam to image the system, however, sometimes the powerful beam could also simultaneously induce some “artifacts”. It can be challenging to interpret those

phenomena due to the complex nature of electron/sample/solution interaction and nature of the system (interfaces, confined space, tiny space). The interaction between the beam and water causes the radiolysis of the water, and lead to many radiolysis products, which could alter the solution chemistry and lead to many observations.

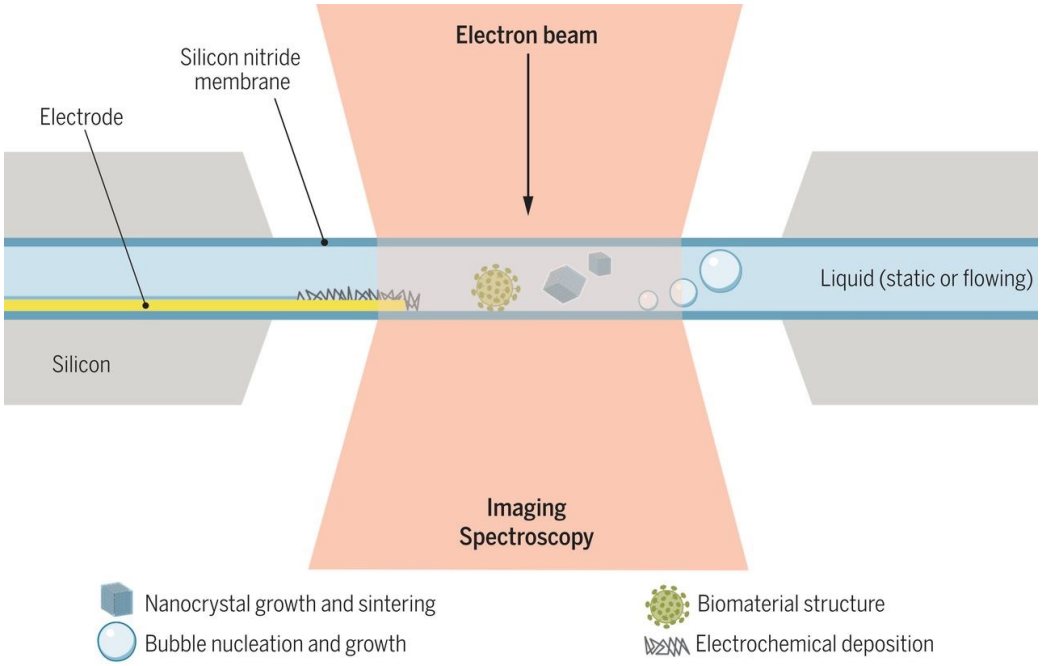

Figure 1.9. Schematic of a liquid cell chamber for the liquid phase TEM and its application for imaging phenomena in materials science, life science, and physics. The chamber is composed of two vacuum compatible electron transparent membranes. The membranes are made of SiN (blue) on a silicon support (gray) in this schematic. A spacer layer (not shown) keeps the membranes at a controlled separation of about 100 nm to 1 mm depending on degree of window bulging. The chamber is filled with the liquid of interest, and the liquid may be flowed using an external pump (not shown). The electron beam (pink) passes through the membranes and liquid to allow recording of images, movies, or spectroscopic data for compositional analysis. Several possible experiments are illustrated: growth of nanocrystals in solution, nucleation and growth of bubbles, imaging biological structures such as whole cells or viruses in liquid water, and imaging electrochemical processes at an electrode (yellow) that is built into the liquid cell. The dimensions of the electron beam and the nanoscale objects are exaggerated and not drawn to scale. [40]

For example, solvated electron could drive beam induced growth by reducing the metallic cations in the solution [30]. Oxidative OH radical could react with the metallic atomic and causing its dissolution [42, 44]. Hydrogen ions could alter the pH of the solution [55]. Hydrogen gas could form gas bubble in the chamber [56]. Those radiolysis products are strongly dependent on the beam dose,

beam dose rate, beam mode (TEM vs. STEM), so playing with those parameters is a good way to evaluate and understand the observations [55]. Most of times the observation should exist in a range of parameters until reaching to some threshold dose or dose rate, in which the phenomena disappear or very slow to observe. It is worth mentioning that the phenomena in the liquid cell happens in such a confined and tiny spatial room, which makes it sensitive to the configuration of the liquid cell chamber, ie. Thickness of the liquid, interface between SiN and solution, precipitation from the solution due to the assembly, impurity from the holder, and beam condition. Very careful and rigorous assembly of the liquid cell procedure and cleaning is highly required to enable repeatable experiment.

Another way to deal with the beam effects is to apply an external stimulus that activates the process of interest. Those stimulus include flowing reactive reagents into the cell [12, 57], or heating the solution in the liquid cell to drive a thermally activated process [58], that is otherwise inaccessible with the electron beam. In the ex-situ scenarios, heating is widely used to activate and speed up the process, so the use of heating in the in situ scenarios could make it more comparable to the ex-situ scenarios. However, very few LP-TEM studies involving heating have been reported because of the technical challenges of heating liquid phase TEM.

1.4 Key questions and hypotheses

The above-mentioned disputes regarding the formation pathway of the mesocrystal, and the nature of oriented attachment lead to a few major questions of my thesis. What is the formation pathway of mesocrystal? What is the role of primary less ordered phase during the crystallization? Can we utilize in situ liquid phase TEM to direct image the crystallization pathway of mesocrystal ? what is the role of ligands?

We have four hypothesized pathways for the mesocrystal formation, which are highlighted in Figure 1.10. The pathway a shows that the less ordered phase first attaches to ordered crystal, and then transform to crystalline phase. While, the pathway b highlights that the less ordered phase will transform to crystalline phase first, and then attach to the crystalline part in an oriented attachment fashion. Pathway c shows that the less ordered phase will transform to crystalline phase, and then dissolve to form new particles on the crystalline particle. Similar to pathway c, the less ordered phase can dissolve, and new crystalline phase nucleate directly on the crystalline phase (pathway d). Due to the small dimension of those phases, and the similarity among the pathways, it is challenging to identify the crystallization pathway without in situ methods. We will apply in situ liquid phase TEM combined with other ex-situ techniques to solve these questions.

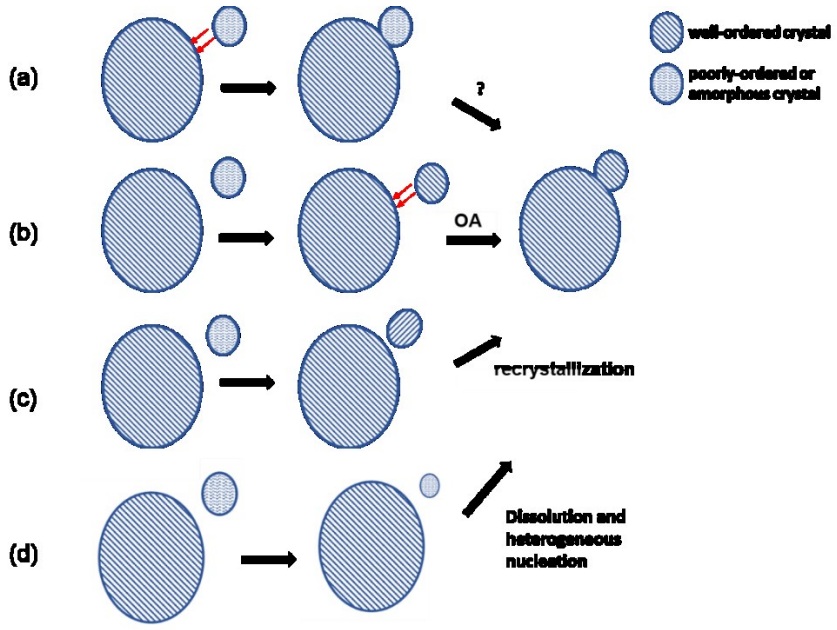

Figure 1.10. Four different pathways that could lead to the formation of mesocrystal. (a) Attachment of less ordered phase (amorphous or poorly-ordered) to the crystalline phase, and then transform to mesocrystal. (b) Transformation of less ordered phase to crystalline phase and then oriented attachment to the other crystalline phase. (c) Transformation of less ordered phase to crystalline phase and then recrystallization. (d) Heterogeneous nucleation and dissolution of less ordered phase.

Chapter 2. Investigate spindle Hm mesocrystal crystallization mechanism

2.1 Abstract

Crystallization by particle attachment (CPA) is a common mechanism of colloidal crystallization resulting in hierarchical morphologies[1-4], and has been both exploited to create nanomaterials with unique, emergent properties[4-6] and implicated in the development of complex mineral textures[1, 7]. Oriented attachment (OA)[7-8], a form of CPA in which crystalline primary particles align and attach along specific crystallographic directions, produces structures — typically referred to as mesocrystals — that diffract like single crystals, even though the constituent particle domains are still discernable[2, 9]. While the existence of mesocrystals has been well documented in a wide range of crystal systems[1-9] and individual particle attachment events have been directly visualized[10], the mechanism by which these seemingly random events lead to well-defined, self-similar morphologies remains a mystery, as does the role of organic ligands, which are ubiquitous in nanoparticle systems[3, 9, 11]. Combining in situ TEM at 80°C with "freeze-and-look" TEM using indexed grids, we tracked formation of hematite (Hm) mesocrystals in the presence of oxalate and interpreted the results using classical density functional theory. The results show that formation of isolated Hm particles rarely occurs. However, once formed, interfacial gradients created by Hm-bound oxalate drive new Hm particles to repeatedly nucleate about 2 nm away from the new interface and then immediately undergo OA. Because Hm nucleation rates are statistically deterministic and direction-specific, the resulting mesocrystals are self-similar. Comparison to natural and synthetic systems suggests interface-driven pathways are widespread.

2.2 Introduction

The conventional view of OA is that nucleation and particle assembly are distinct events. That is, nucleation provides a supply of primary particles, which encounter other primary particles or particle aggregates via Brownian motion biased locally by attractive interparticle potentials. However, many mesocrystals exhibit highly regular morphologies and uniform size distributions, with shapes that appear similar irrespective of size or location, which calls into question how a random nucleation, diffusion and aggregation process can underlie their formation. (Random cluster-cluster aggregation is predicted to produce power-law cluster size distributions [59].)

Attempts to understand how the initial nuclei evolve to a mesocrystal via OA have been complicated by the fact that, in many mineral systems, the first particles to form during crystallization are often of a distinct phase from that of the stable bulk phase[1, 12, 60]. Consequently, OA often occurs in concert with a phase transformation such that the resulting mesocrystal consists of the bulk phase instead of the primary phase. Little is known about the role of starting primary phase, how or when phase transformation and ordering takes place. While some studies have proposed that particles convert before attachment[61], others have attributed conversion to the attachment process itself[27] and still others have concluded that transformation occurs after the mesocrystal exceeds a characteristic size[60, 62]. Figure 2.1 depicts many competing processes of the crystallization process. Still further confounding attempts to develop a predictive understanding of OA is the fact that nanoparticles, whether synthetic or natural, are typically coated with surface-bound ligands[63] and thus studies on bare nanoparticles provide limited insight into the vast majority of OA systems[9]. While all but a few of the above studies based their conclusions on morphological and structural data obtained post-synthesis, they nonetheless highlight the key knowledge gaps in understanding of OA mechanisms and pathways.

To address these gaps, we investigated mesocrystal formation of iron oxides, which are amongst the most important colloidal phases in natural environments[64-65]. Iron oxides present classic examples of systems that both form ubiquitous precursor phases and undergo OA accompanied by phase transformations to more stable forms[61, 65-67]. Moreover, in soils, where iron oxides are amongst the most common mineral phases, organic constituents, such as oxalate (Ox), are abundant and commonly associate with mineral surfaces, thus the role of organic adsorbates is of particular importance[68].

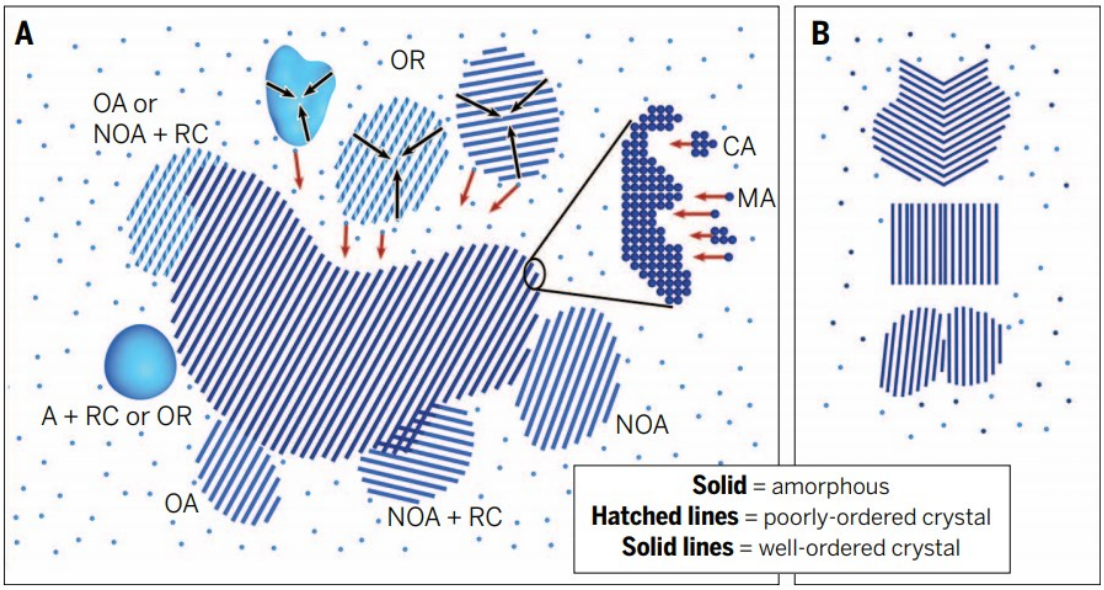

Figure 2.1. Multiple growth mechanisms can occur simultaneously within a single crystallizing system, depending on the values of global parameters such as supersaturation, local factors that include interface curvature, and materials parameters such as phase stability versus particle size. (A) In this diagram, the arrows indicate the direction of motion of monomers, clusters, or surfaces, and the dashed lines give the crystallographic orientations of nanocrystals. The expanded oval shows molecular-scale processes. OR, Ostwald ripening; MA, molecular attachment; CA, cluster attachment; A, amorphous addition; OA, oriented attachment; NOA, non- or semi-oriented attachment; RC, recrystallization. The phases are denoted by uniform blue for an amorphous crystal, wavy lines for a poorly ordered crystal, and solid lines for a well-ordered crystal. (B) Twins, stacking faults, and dislocations can result from the attachment of crystalline particles

2.3 Iron oxide

Iron oxide (including iron oxides and iron hydroxides) is a widespread material present in the Earth's crust, soils, and waterways. Iron oxides are of great interest particularly in geoscience, industry, corrosion science and biology[69-70]. In contrast to the metals and organics, metal oxides have distinct physical properties, a common occurrence of polymorphs, and phase/orientation dependent chemical properties. The iron oxides, in particular, have many polymorphs, very low solubility, polar metal oxide bonding (a mixture of covalent and metallic bonding) and complex surface structure especially when in aqueous solution. Phase transformation among different polymorphs within the iron oxide family is very common (Figure 2.2a), and less stable phases always precede the well-ordered and most stable crystalline phase (Ostwald step rule). [71] In our work of Hm crystallization, Fh forms first after mixing of the two reactant solutions. Hm gradually starts to form until all the Fh are transformed to Hm. Fh is typically small in size (<7 nm) with poor crystallinity. In fact, the structure of the Fh phase is still under debate.[72] It is thereby difficult to probe the mechanism of the Hm transformation from Fh. Hm is a more stable polymorph, and has a trigonal crystal system. It has four FeO_6 octahedron in its unit cell, and has cell parameters as a = 5.038 Å, b = 5.038 Å and c = 13.772 Å.[72]

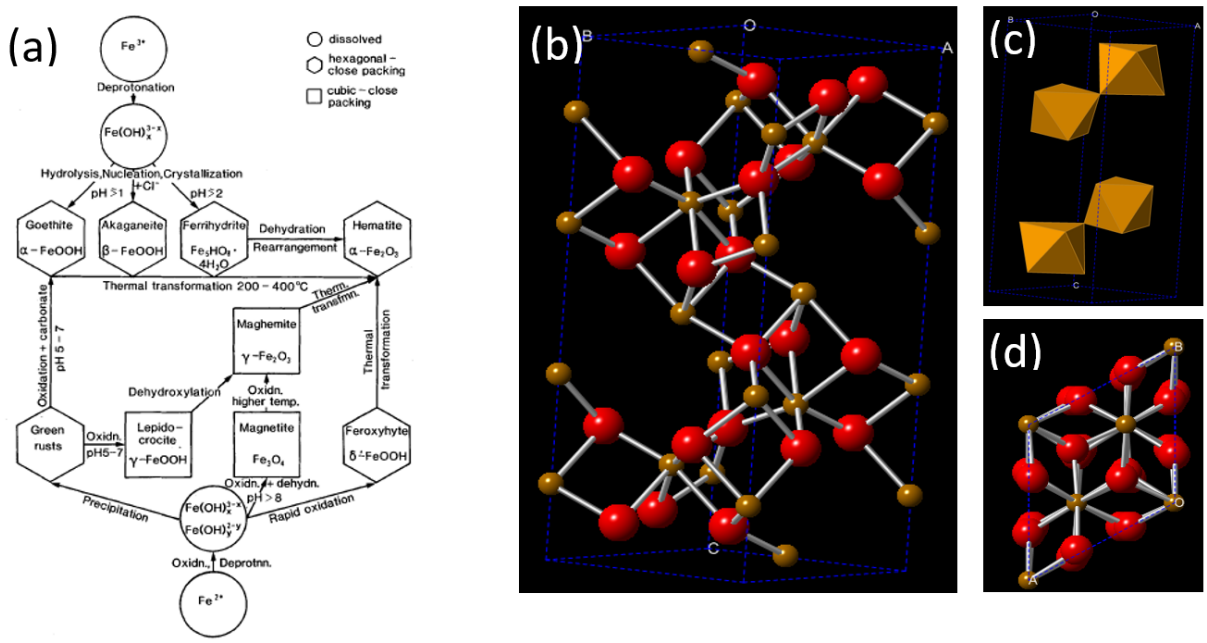

Figure 2.2. (a) Schematic of the phase transformation in the iron oxide family among different polymorph. We will focus on Fh to Hm phase transformation as an example. This kind of phase transformation is very typical in metal oxide. (b) Atomic model of Hm unit. (c) Polyhedral model of Hm unit showing four FeO_6 octahedron. (d) Top view of Hm along the c axis / [001]. [72]

In this work, Hm mesocrystal is formed with the addition of oxalate into the system. Hm mesocrystal has a spindle shape, with particle aggregated domains but are atomically aligned to each other making the final structure single crystalline. It is worth noting that, these morphological and structural characteristics are also observed in many other materials, such as zinc oxide and copper oxide. While those materials are believed to form via the oriented attachment growth mechanism, [28] alternatively, it is important to leave open the possibility that the Fh phase simply serves as a precursor to the hematite formation, either by direct conversion or through dissolution and precipitation. This divergence in potential pathways sets the stage to the key knowledge gaps and hypotheses of my research.

2.4 Syntheses and characterization methods

2.4.1 *Growth of rhom Hm with smooth facets*

The growth of rhombohedral Hm [64, 69, 73] was achieved by mixing 0.6 mL iron nitrate (72 mM) and 0.38 mL sodium hydroxide (0.32 M) solution, without oxalate in a 15ml Teflon container. The pH was adjusted to neutral using sodium hydroxide or nitric acid solution. The solution was then heated in the oven at 90 °C for 10 hours.

2.4.2 *Growth of Spindle Hm mesocrystal from Fh*

Spindle Hm was synthesized following a procedure adapted from Schwertmann and Fischer [64-65, 69, 74]. Briefly, 2-line ferrihydrite (Fu) was synthesized by mixing 0.6 mL iron nitrate (72 mM) and 0.40 mL sodium hydroxide (0.32 M) in a 15mL Teflon container. 15 µL sodium oxalate (0.253 M) was added to the mixed solution and the final oxalate concentration was kept around 2 mM. The final pH of the mixed solution was adjusted by adding sodium hydroxide solution and nitric acid solution and kept in the range of 6.0 - 8.0. The container was incubated in an oven at 90 °C for hours without any light illumination.

2.4.3 *Statistics of spindle growth*

Between 25-40 spindles were randomly chosen for the measurement of each time point. The error bars represent the standard deviation. For the early time points of 2 hours, because there were many Fh particles mixed in with the Hm, we acidified the solution to selectively dissolve the Fh in order to obtain better TEM image of Hm. The domain size was determined by measuring 5-10 individual domain particles in each spindle and averaged over all the spindles. To do so, we chose domain particles at the tip of each spindle. We assume the domain particles inside the spindle have similar dimension based on the cross section TEM imaging and 3D tomography. For each domain

particle, we identified its center and measured its length perpendicular to the c axis. We consistently used the same measurement protocol for all the time points. Domain # is approximately calculated by multiplication of length/domain and the square of width/domain.

Table 2.1. Statistics of length and width of spindles and the domains inside the spindle

Time (hour)	Average domain size (nm)	Average spindle width (nm)	Spindle length (nm)	Width/domain	Length/domain	domain #
2	3.3 ± 0.4	20.5 ± 3.9	44.6 ± 5.1	6.2 ± 2.0	13.5 ± 3.3	519 ± 271
4.5	4.8 ± 0.6	41.3 ± 9.7	92.5 ± 21.1	8.6 ± 3.2	19.3 ± 6.9	1426 ± 899
7	5.2 ± 0.8	40.5 ± 13.6	94.3 ± 29.6	7.8 ± 3.7	18.1 ± 8.3	1103 ± 904
12	6.0 ± 0.5	47.8 ± 12.3	111.4 ± 31.2	8.0 ± 2.7	18.6 ± 6.8	1188 ± 721
24	6.5 ± 0.6	43.2 ± 11.9	104.3 ± 24.3	6.7 ± 2.5	16.0 ± 5.3	720 ± 447
50	7.2 ± 1.0	42.6 ± 11.2	99.4 ± 21.3	6.0±2.3	13.8 ± 4.8	497 ± 323
100	7.6 ± 1.1	40.2 ± 10.2	93.5 ± 19.4	5.3 ± 1.9	12.3 ± 4.6	344 ±217
150	8.1 ± 1.1	37.3 ± 10.1	89.2 ± 18.3	4.6 ± 1.8	11.0 ± 4.2	234 ± 157
200	8.5 ± 1.2	32.4 ± 10.2	88.2 ± 18.4	3.8 ± 1.6	10.4 ± 4.1	151 ± 108
294	9.1 ± 1.4	26.4 ± 11.3	83.5 ± 15.7	2.9 ± 1.3	9.2 ± 3.8	77 ± 59

2.4.4 *Growth of spindle Hm over existing rhombohedral Hm seeds synthesis of rhom Hm without oxalate*

Rhom Hm seeds were obtained following the same method described above. The seeds were washed by adding 5 mL of water into the suspension and followed with centrifugation. The seeds were washed twice, and mixed with the solution for the synthesis of spindle Hm. Then the suspension was shaken and sonicated (Branson, 1800 series) for 1 min and placed into the oven at 90 °C. After 5 hours, spindle Hm could be obtained with rhom Hm seeds inside the spindle. Some of the spindle Hm particles could be formed without the rhom Hm seeds.

2.4.5 *Cryo-TEM to monitor the crystallization. synthesis of rhom Hm without oxalate*

Cryo TEM was performed in the Titan ETEM 80-300 kV and Tecnai G^2 F20. Samples (3 μL) were vitrified at different time points using an automated vitrification robot (FEIVitrobot™ Mark III, FEI Company), which is a commercial setup to make cryo samples by blotting the sample and quickly plunge them into liquid ethane cooled by liquid nitrogen. R2/2 Quantifoil Jena grids (Quantifoil Micro Tools GmbH, Germany) were surface plasma treated before the vitrification procedure using a Cressington 208 carboncoater. A continuous thin amorphous ice layer is the ideal case for cryo TEM imaging. A cryo holder (Gatan Inc., USA) operating at ~−170 °C was used. Further image analysis was performed using ImageJ (v1.43m), a public domain NIH image processing and analysis program written by Rasband.

2.4.6 *Reference TEM grids to investigate the Fh to Hm transformation*

Reference TEM grids made of molybdenum or gold (Ted Pella, 7GG300) were used. The reference grids are marked with alphabets and numbers. First, a 10 μL solution of 2-line Fh was dropped on the grid, and air dried. TEM was used to identify several regions of interests, and the grid was placed inside a reaction solution which contains oxalate at a concentration of 2 mM, and heated to 90 °C. After a few hours, take out the TEM grid and put it to the TEM and look at the same positions marked before. It is worth noting that Fh is not strongly bonded with the substrate at 90 °C, multiple regions need to be examined in order to improve the success rate.

2.4.7 *Cross section of spindle Hm using microtome*

Spindle Hm solution was infiltrated in LR White resin (Electron Microscopy Sciences, Hatfield, PA), and polymerized at 60 °C for 24 hr. The hardened blocks were sectioned to about 50 nm ultrathin sections on Reichert UCT microtome (Leica) by a 45 deg diamond knife

(Diatome). The sections were mounted on Ultrathin C Au grids (Ted Pella). A rough estimate of the thickness of the section can be achieved by comparison to the interference card which gives a color spectrum with the corresponding section thickness. Both the 3D tomography and image of the cross section confirm the porous structure of spindle Hm, which consists of crystallographically aligned primary particles.

2.4.8 *In situ Liquid phase TEM heating experiments*

LP-TEM was performed using an in situ fluid stage (Protochips) with heating control. The heating capability was previously demonstrated to give a stable performance [75]. Two silicon chips with silicon nitride membranes were used to encapsulate the liquid for TEM analysis. The thickness of spacers which were used to separate the two silicon chips were about 100 nm. The tip of the holder was cleaned by sonication in ethanol first, and then warm water (80 °C) for over half an hour before every experiment to remove possible contamination. Amorphous silicon nitride membranes with a thickness of about 50 nm spanned the opening in the center of the silicon chips to form the electron transparent window. The membrane was cleaned by being sequentially rinsed with acetone, isopropanol, and water. The solution was dropped onto the chips which were then assembled according to previous report [54]. The solution contained a mixture of rhombohedral Hm, Fh and oxalate, using the same conditions used for growing spindle Hm over existing rhombohedral Hm seeds. After loading into the TEM, several regions of interest were located and marked. We heated the solution at a rate of 1 °C/min to minimize stage drift and air bubble formation. During the experiment, the electron beam was blocked by blanking the beam, and the electron beam was only applied while searching the area of interest, adjust the focus, and acquire images.

A 200-kV FEI Tecnai G^2 microscopy was used with a 2048 × 2048-pixel charge-coupled device camera (FEI). TEM is operated at 3900 extracting voltage, with acceleration voltage of 200 KV, gun lens is 6.

During the in situ experiment, SiN chips act as a container that encloses the solution, which contains Fh. In order to exclude the influence of the container on the Hm crystallization, reference experiments were performed by adding the liquid cell chips into the solution for the synthesis of spindle Hm between 70 °C to 90 °C. Typical spindle Hm with the characteristics of mesocrystal were obtained, showing negligible effects of the liquid cell chips on crystallization of Hm from Fh.

2.4.9 *Cross section of spindle Hm using microtome*

Spindle Hm solution was infiltrated in LR White resin (Electron Microscopy Sciences, Hatfield, PA), and polymerized at 60 °C for 24 hours. The hardened blocks were sectioned to about 50 nm ultrathin sections on Reichert UCT microtome (Leica) by a 45 deg diamond knife (Diatome). The sections were mounted on Ultrathin C Au grids (Ted Pella). A rough estimate of the thickness of the section can be achieved by comparison to the interference card which gives a color spectrum with the corresponding section thickness. Both the 3D tomography and image of the cross section confirm the porous structure of spindle Hm, which consists of crystallographically aligned primary particles.

2.4.10 *In-situ FTIR study of oxalate adsorption on different Hm facets.*

Infrared (IR) spectra of oxalate adsorbed on Hm samples with predominately (001) and (012) crystal faces [76] were collected using a FastIR (Harrick Scientific) attenuated total reflection (ATR) cell with a custom built flow attachment and a single-reflection silicon internal reflection element

[77]. The Hm indexing is based on the hexagonal unit cell with cell parameters a = 5.038 Å, b = 5.038 Å, c = 13.772 Å, α = 90°, β = 90°, and ϒ = 120°. (001) is the c-cut of hematite, or (0001) if using bravais-miller indexing while (012) is the r-cut of hematite, or (1-102). The spectrometer was a Bruker Vertex 80v with an air-cooled source and a deuterated triglycine sulfate detector. Spectra were an average of 512 scans at 4 cm^{-1} resolution between 360 and 5000 cm^{-1}. The following procedure was used for each Hm sample. First, a background spectrum of the empty cell was collected. Second, a 4 g/L aqueous suspension was evaporated onto the ATR crystal under flow of dry N_2 (g), deionized H_2O was reintroduced into to the flow cell atop the mineral overlayer, and a sample spectrum of the Hm exposed to water was obtained. Third, a 2 mM solution of oxalate at pH 4 was flowed through the cell, and sample spectra of oxalate adsorbed to Hm were collected as a function of time until the adsorption reaction had come to equilibrium, as indicated by no further increase in the oxalate asymmetric CO stretching bands at 1680 cm^{-1}. Quantitative comparison of the spectra of oxalate adsorbed on each Hm was performed by normalizing the spectra using the Fe-O stretching band of the bulk mineral at 522 cm^{-1}.

Table 2.2. Experimental and calculated oxalate coverage (θ) on Hm (001) and Hm (012) surfaces. Maximum coverage corresponds to the density of surface adsorption sites and actual coverage reflects oxalate coverage.

	Oxalate coverage (sites/nm^2)		
	Experimental	Calculated*	
		maximum	actual
θ(001)	4.38	4.55	4.30
θ(012)	12.17	14.61	13.92
Ratio: θ(012) / θ(001)	2.78	3.21	3.24

2.4.11 *Simulation of potential of mean force of Fe ions and particle/particle interaction*

Classical density functional theory (cDFT). The focus of the theoretical simulations was on understanding the thermodynamic driving forces for the observed non-classical nucleation and

growth pathway. To achieve this goal, we used a DFT-based atomistic-to-mesoscale approach we developed [78]. The details of the cDFT approach used in this work were previously published elsewhere (see ref. [78] for full details and ref. [79] for numerical implementation) and provided below for completeness. The aqueous salt solution was modeled as a dielectric medium with 78.5, consisting of discrete charged spherical particles representing ions, and neutral spherical particles representing water molecules. The concentration of spherical "water molecules" was 55.5 M, chosen to model experimental water density. We used experimental crystalline ionic diameters for mobile ions equal to 0.146 nm for Fe^{3+}, 0.204 nm for Na^{+}, 0.358 nm for NO_3^- and van der Waals diameter for water molecules equal to 0.275 nm and oxalic acid equal to 0.655 nm. Ion charges reflected the dominant species in experimental pH interval of 5.5 to 7.5 and were equal to -2 for oxalic acid, -1 for NO_3^-, +1 for Na^{+}, +3 for Fe^{3+} ions and 0 for water. More detailed speciation of water was not considered in this study. The complexation between other species, e.g. Fe^{3+} and Ox^{2-}, in solution was not imposed *a priori*. Therefore, the formation of multispecies complexes through electrostatic and short-range interactions may occur as a result of optimization of the structure of interfacial solution. Short-range interactions were treated explicitly, as described above. Interactions of oxalic acid with bulk-terminated 1x1 Hm surface slabs were calculated using plane-wave DFT and the adsorption energies were found to be equal to 1.62 eV and 0.34 eV for (001) and (012) surfaces, respectively. Atomic positions of the surface iron atoms were used to define the spatial distribution of surface interaction sites for oxalate. Experimental enthalpies of hydration were used for short-range interactions of all ions and ligands with water. The model considers two Hm nanoparticles in aqueous solution containing 32 mM $Fe(NO_3)_3$, 100 mM NaOH and 3 mM oxalic acid, at interparticle separations varying from 0.5 nm to 7.0 nm.

Within cDFT, solvent density is optimized along with the densities of all other species and as such solvent structuring and solvation effects are intrinsically included in all components of the free energy. The total free energy functional will then have the contributions from Coulomb interactions (F_C^{ex}), electrostatic correlations (F_{el}^{ex}), hard sphere repulsion (F_{hs}^{ex}), short-range interactions (F_{sh}^{ex}) between the species, image interactions (F_{im}^{ex}) and ion-surface interactions (F_{ion-s}^{ex}):

$$F^{ex} = F_C^{ex} + F_{el}^{ex} + F_{hs}^{ex} + F_{sh}^{ex} + F_{im}^{ex} + F_{ion-s}^{ex}$$

All contributions to the excess free energy, except the short-range term, are calculated analytically from first principles using the Mean Spherical Approximation, the Fundamental Measure Theory and Lifshitz theory of dispersion interactions. The short-range interactions between all mobile species are given by

$$F_{sh}^{ex} = \frac{1}{2} \int_\Omega \int_\Omega dr\, dr' \, \Sigma \rho_\alpha(\Upsilon) \rho_\beta(r') \Phi_{\alpha\beta}(|\mathrm{r} - \mathrm{r}'|)$$

where $\Phi_{\alpha\beta}$ is the square-well potential with the depth equal to the equilibrium pair-wise interaction energies calculated using plane-wave DFT These interactions include ion-solvent interactions (solvation) and ion-surface chemical interactions. Particle-particle dispersion interactions treated using Lifshitz theory of dispersion forces.[80] The cDFT code is parallelized using the multigrid approach and a linear scaling with respect to the number of grid points has been achieved.[79] This allows modeling heterogeneous systems with the sizes up to a micron in 3D.

Chemical potential calculations utilize the notion that although the total chemical potential for each of the species is constant, individual components of chemical potential are position dependent, vary with local concentration and reflect the nature of the driving forces for nucleation and growth:

$$\mu^{bulk} = \mu^{id}(r) + \mu^{ex}(r)$$

Where $\mu^{id}(r)$ is the ideal chemical potential and

$$\mu^{ex}(r) = \mu_C^{ex}(r) + \mu_{el}^{ex}(r) + \mu_{hs}^{ex}(r) + \mu_{sh}^{ex}(r) + \mu_{im}^{ex}(r) + \mu_{ion-s}^{ex}(r)$$

The excess chemical potentials (potential of mean force) were averaged over the gap volume.

2.5 Results and discussion

2.5.1 *Time dependent ex-situ TEM/STEM characterization*

We started with a precursor consisting of aggregates of poorly crystalline two-line ferrihydrite ($Fe_2O_3 \cdot xH_2O$, Fh), as verified by the electron diffraction, which exhibited the two characteristic diffuse rings at approximately 1.5 Å and 2.5 Å (Figure 2.3a). In the absence of additives, single crystals of Hm (Fe_2O_3) with well faceted surfaces formed within 10 hours (Figure 2.4a, b and c). HRTEM imaging of the rhom Hm and its FFT suggest that the good crystallinity of the rhom Hm (Figure 2.4c). However, upon addition of 2 mM sodium oxalate (NaO_x), after two hours, spindle-shaped Hm began to appear within the Fh aggregates (Figure 2.3b). By 10 hours, all Fh disappeared, and only spindle-shaped Hm mesocrystals remained (Figure 2.3c and Figure 2.4d, e and f). So it appears that Hm crystallizes at the cost of Fh, but we don't know how Fh transform to Hm and how Hm mesocrystal form at nm or atomic scale.

We tried to identify the crystallographic direction of the long axis of the spindle. In order to do that, we first found an isolated Hm spindle in the TEM field of view (Figure 2.4g). We then rotated the sample to find a position in which the long axis of the particle was its maximum length in the projection. Finally, we performed electron diffraction on the spindle, and we then assigned the axis of elongation based on the diffraction pattern (Figure 2.4h). We found that 10 out of 10 particles were elongated along [001].

Primary particles within the spindle Hm is clearly identified (Figure 2.3d, e and f). The FFT enclosed shows the single crystalline nature of the spindle mesocrystal, although, the arc of the FFT spot suggests that there is probably some mismatch in the spindle. Dimensional analysis showed that the size of the primary particles increased from about 3.5 nm at 2 hours (Figure 2.3d), to 6.5 nm at 10 hours (Figure 2.3e) to 9.5 nm at 200 hours (Figure 2.3f). Notice the primary particles are similar but not identical. We measured the particle size by only measuring the size form the tip of the spindle to make the measurement consistent.

A plot of spindle length vs. width revealed a constant aspect ratio of about 2.15 ± 0.08 for all spindles and all times in multiple experiments, demonstrating the deterministic nature of spindle growth. Because the primary particles are approximately spherical and uniformly distributed, this constant aspect ratio implies the particle addition rate was ~ 2.2 times faster along the [001] than along the [hk0] directions. Moreover, this consistency was maintained even though the average spindle length and width both increased for the first 12 hours and decreased thereafter (Figure 2.3g and h).

The analysis also shows that spindle development proceeded in two stages: During the first stage, spindles grew in length, width and particle number. During the second stage, spindle size decreased, but the average primary particle size continued to grow while the total number of discernable particles decreased so that the total volume particles ins a spindle remained nearly constant (Figure 2.3i). The transition from the first to second stage correlated with disappearance of the Fh (Figure 2.3c and i). These results imply that the first stage is dominated by spindle growth through continual addition of Hm particles that form at a solution saturation state set by the more soluble Fh, which gradually decreases in mass. In contrast, the second stage is dominated by particle coarsening in a solution at equilibrium with respect to Hm and devoid of Fh.

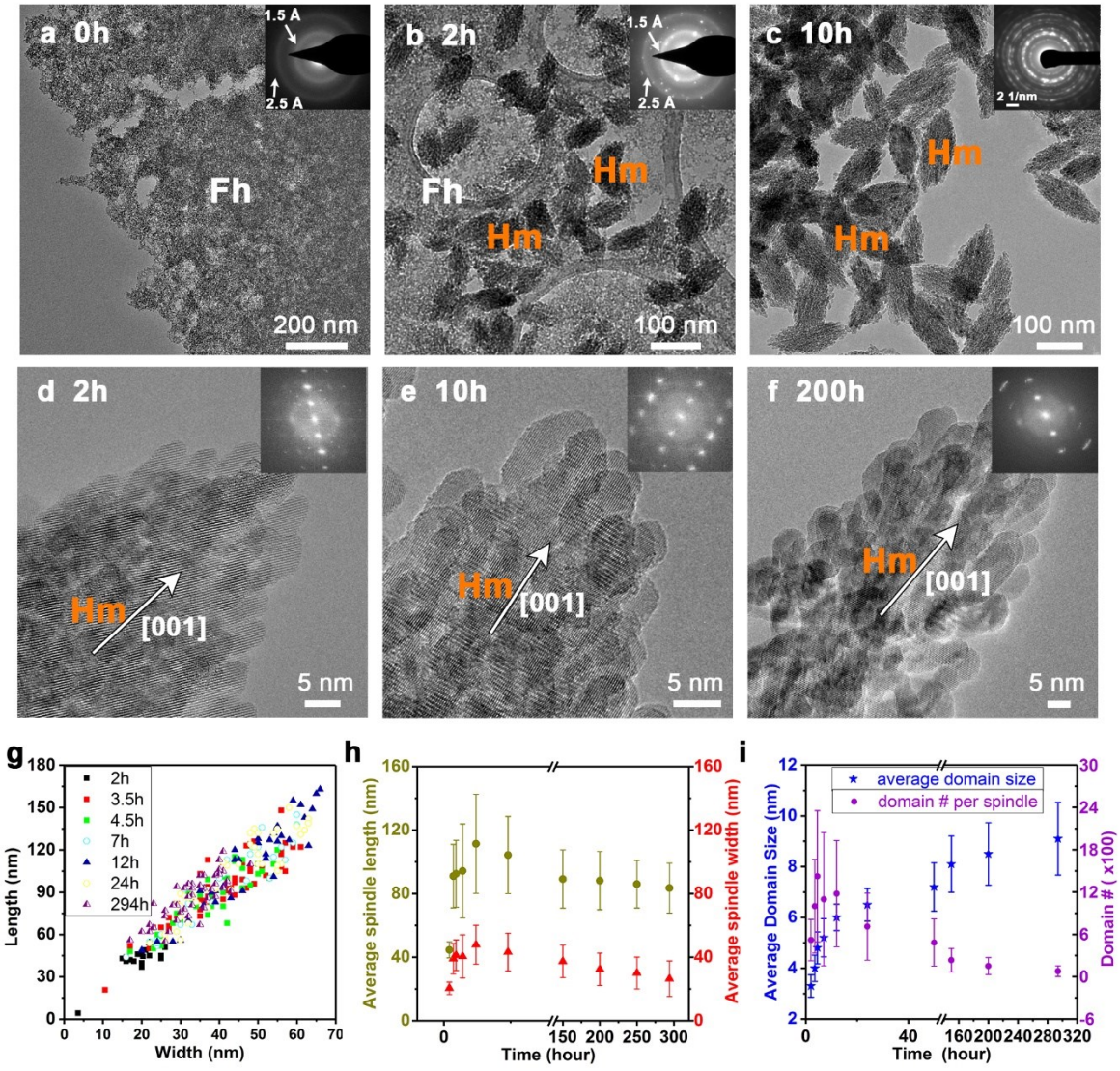

Figure 2.3. Formation of spindle-shaped Hm mesocrystals from Fh nanoparticles. a Ex situ TEM image of Fh aggregate, with selected area electron diffraction (SAED) showing two diffuse rings. b Spindle-shaped Hm appeared in 2 hours. c Transformation of all the Fh to Hm occurred by 10 hours. d-f HRTEM images of spindle-shaped Hm exhibiting crystallographically coaligned domains whose sizes increase with time. Insets: FFTs performed on whole images. g Spindle length vs. width, showing constant aspect ratio. h Plots of average spindle length (green color) and width (red color) as a function of time. i Plots of average domain size (blue color) and domain number per spindle (purple color) as a function of time. (After about 10 hours, the product of average domain volume and number is approximately constant.)

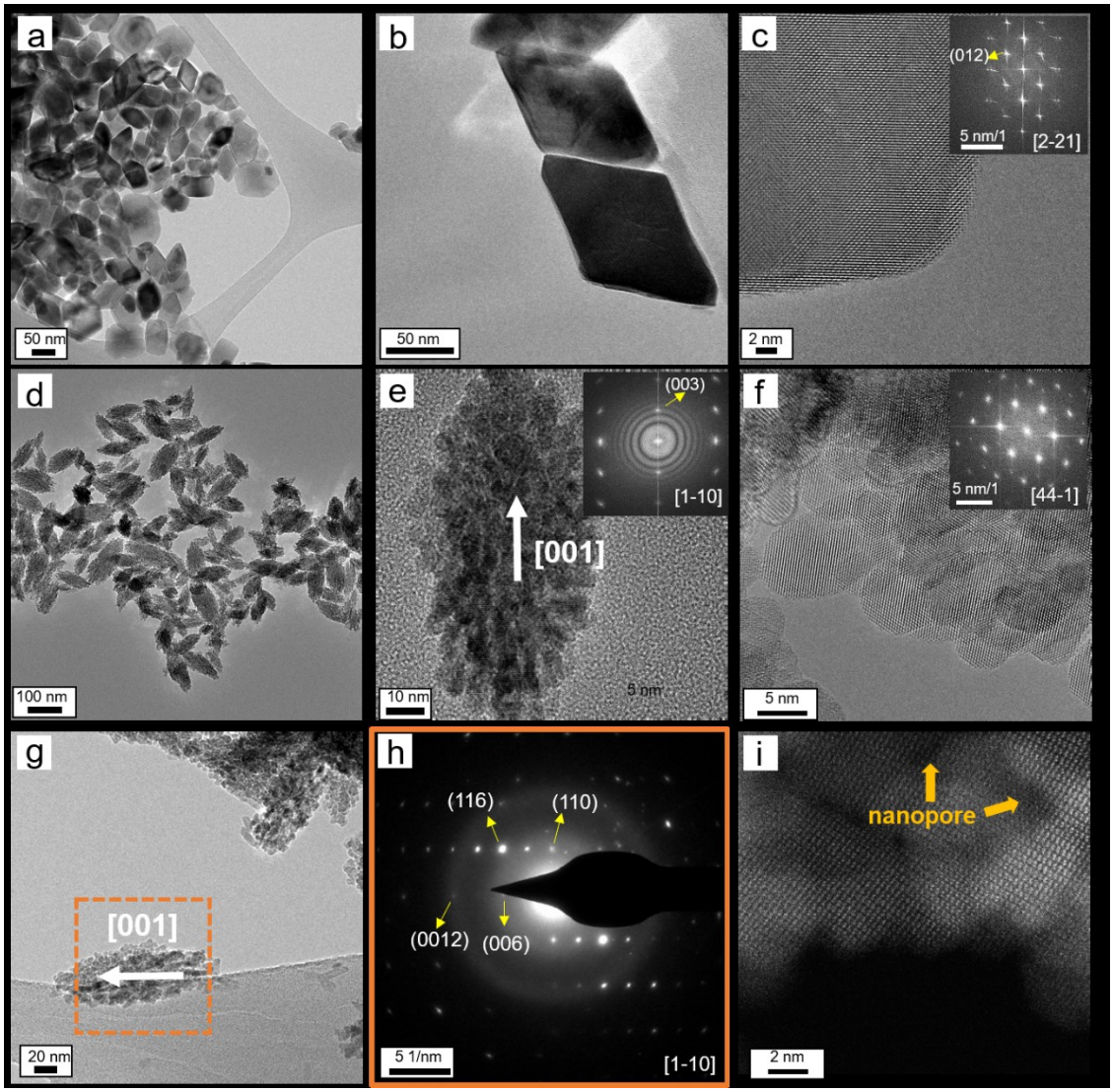

Figure 2.4. Characteristics of rhom Hm vs. spindle Hm. a, b, TEM image of rhom Hm, synthesized without adding oxalate. c, HRTEM image of the edge of rhom Hm showing a smooth surface with a perfect 2D lattice. d-f, TEM image of spindle Hm with a rough surface synthesized with addition of oxalate, showing the spindle is comprised of atomically aligned primary particles. g, h, Example of the use of electron diffraction to identify the elongation direction of the spindle. Similarly, FFT of the HRTEM image (e, inserted) were used to identify the elongation direction of the spindle, which is [001]. i, High resolution Scanning TEM image of the edge of the spindle highlighting the continuity of the lattice from particle to particle. Potential nanopores are indicated by the arrow in i.

Ex-situ TEM is a convenient tool for characterizing the morphology, however, drying effect during the TEM sample prep might compromise the results. Cryogenic Electron Microscopy (cryo-EM) is an EM technique applied on sample cooled to cryogenic temperature and embedded in a

vitreous water layer. The sample solution is applied to a grid-mesh and plunge-frozen in liquid ethane, which can preserve the native structure of the material in the solution. Figure 2.5 shows a time series of TEM images of the sample, which confirms the ex-situ TEM results are free of drying effect. Due to the vitreous water layer in the cryo TEM, the spatial resolution is compromised. We freeze dry the cryo TEM sample to evaporate the vitreous water to gain atomic information of the structure at the same time, which proves that the Hm mesocrystal is formed in the solution, but not a result of drying effect.

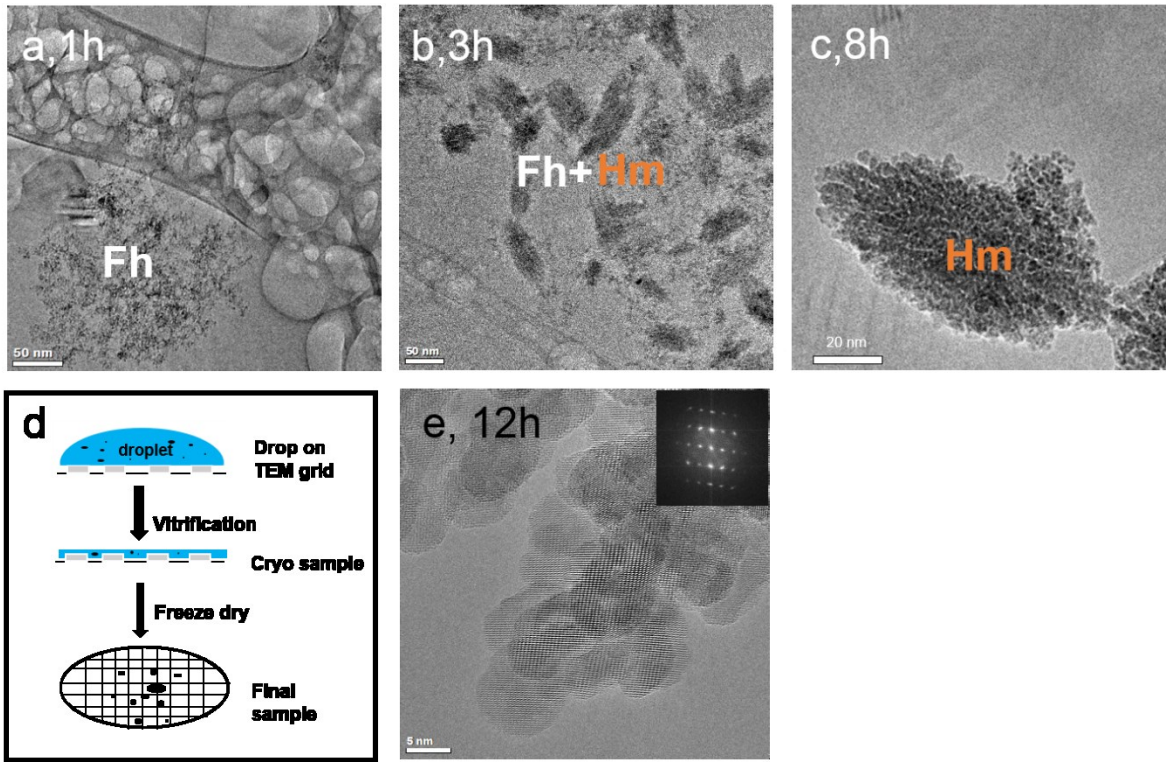

Figure 2.5. Cryo TEM investigation of the growth of spindle-shaped Hm mesocrystal from Fh at 90 degree. **a,** Loose aggregates of Fh at 1 hour. **b,** Spindle Hm appears among Fh aggregates after 3 hours. **c,** Spindle Hm after 8 hours. **d,** Schematic of cryo sample preparation and sublimation of the vitrified ice to remove the background from the ice. **e,** HRTEM of the spindle to confirm the formation of Hm.

2.5.2 *Cross section and 3d tomography of spindle Hm*

In order to characterize whether the particle structure is on the surface or throughout the spindle in 3d. We used microtome method to make thin section of the sample down to to ~ 20 nm in thickness. Cross section of the spindle along different direction is shown in figure 2.6, where you can both identify particle structures inside the spindle. The size of the particle structure is close to the ones from the surface. Scanning TEM (STEM) imaging is easier interpreted compared to TEM imaging, as the contrast is proportional to the mass thickness of the sample. The STEM images in Figure 2.6 suggest that this is a porous structure, while, the 3d tomography of the spindle (Figure 2.7 c) again confirms that the structure is porous. Overall, by combining cross section TEM , STEM imaging and tomography, we confirm that the spindle is porous, and particle domains are inside the spindle.

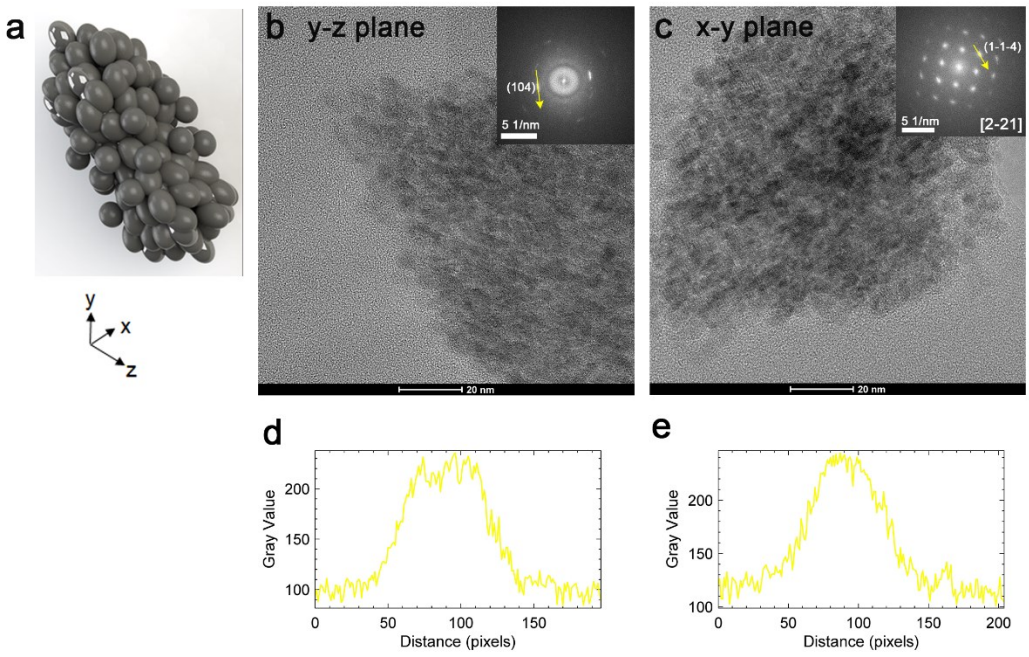

Figure 2.6. TEM imaging of Cross section of spindle Hm. **a,** Schematic of a spindle consisting of an aggregate of primary particles. **b,** TEM image of the cross section through a cut parallel to a y-

z plane, with the insert showing the FFT of the structure. **c,** Cross section of a cut parallel to an x-y plane, with the insert showing the FFT of the structure. **d,** Line profile along the (104) plane in the b, inserted. **e,** Line profile along the (1-1-4) plane in the c, inserted. The elongation can be used to measure the particle misorientation.

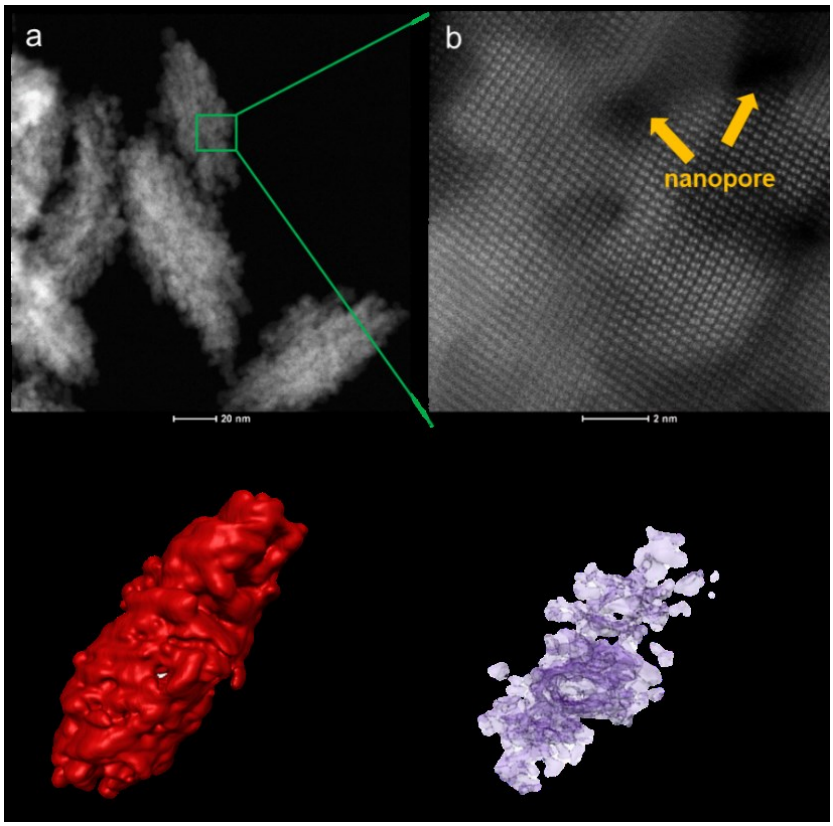

Figure 2.7. STEM image of the spindle Hm. b, High resolution scanning TEM image of the Hm spindle highlighting the nanopore inside the Hm. c, 3D tomography of the spindle Hm. Worth noting that this is a coarse version of the tomography, but to demonstrate that the spindle is porous. d, A rough estimation of the nanopore distribution inside the spindle Hm based on the 3D tomography.

2.5.3 *Reference grid keeping track of crystallization*

In addition to ex-situ TEM imaging of the evolution of Fh and Hm over time, we developed a "freeze and look" method by loading indexed TEM grids with Fh and imaged the grids over time. The Fh-loaded grids were then placed into Ox-containing solution at 90 °C. The grids were returned to the TEM for imaging in the same regions after a few hours of reaction (Figure 2.8a and Figure 2.9). Fh on the indexed TEM grid was observed to consist initially of large aggregates

(Figure 2.8b). After 3 hours, the overall morphology of the Fh aggregates was preserved and the first Hm particles began to appear, but were only found amongst the Fh aggregates (Figure 2.8c). Given that the solution must be in equilibrium with Fh, the fact that Hm only exists in association with the Fh implies that the initial Hm particles must form either through transformation of Fh or heterogeneous nucleation at the Fh/solution interface.

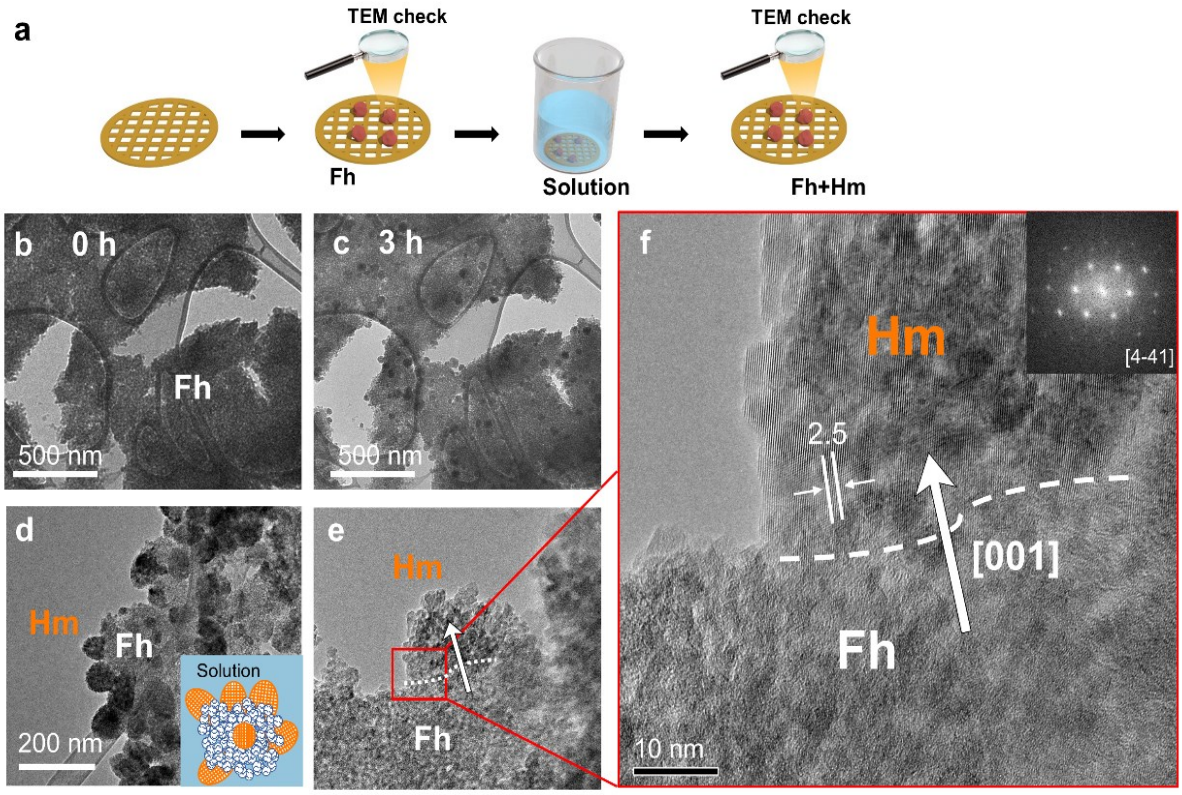

Figure 2.8. Relationship between developing Hm spindles and Fh precursor. a Schematic of experimental approach using indexed TEM grids to follow the reaction at a given location over time. **b** Aggregates of Fh deposited on an indexed lacy carbon TEM grid. **c** Appearance of Hm particles among the Fh aggregates after 3 hours. **d** Representative images of Hm particles and half-spindles on the edge of the Fh aggregates. Inset illustrates the aggregates of Fh (blue) with half spindles (red) growing on the top and pointing towards the solution. **e, f** TEM images of a half-spindle Hm pointing away from the Fh and into the solution, with crystallographically coaligned domains. The Fh-Hm boundary is marked by the dashed line.

A closer examination of the Hm particles showed that they exhibited a half-spindle shape with all of the Hm half-spindles pointing towards solution rather than into the Fh aggregate (Figure 2.8d and Figure 2.9 c and d). HRTEM near the spindle-Fh interface (Figure 2.8e, f and Figure 2.9e)

shows the primary Hm particles are crystallographically coaligned (see inset FFT pattern) and spindles formed in this manner are also elongated along the c axis. If the Hm spindles were growing through direct addition of Fh, which then transformed to Hm, we would expect the spindle to be growing into the aggregate of Fh particles, i.e., the tip of the spindle would advance toward the source of the Fh particles. The fact that the spindle tip advances towards the Fh source and into the bulk solution implies that the Hm primary particles are instead crystallized from the surrounding solution, so this suggests that the Fh is dissolving back to the solution to provide solutes for the Hm crystallization.

Compared to ex-situ TEM results, this same TEM grid method can provide quasi in situ data about the crystallization, dissolution, phase transformation, etc. So it has a big potential application in investigating structural change after reaction. It will be particularly valuable for system that involving different phases at a mild condition. Reaction at room temperature is ideal as the TEM grids might influence the system under high temperature.

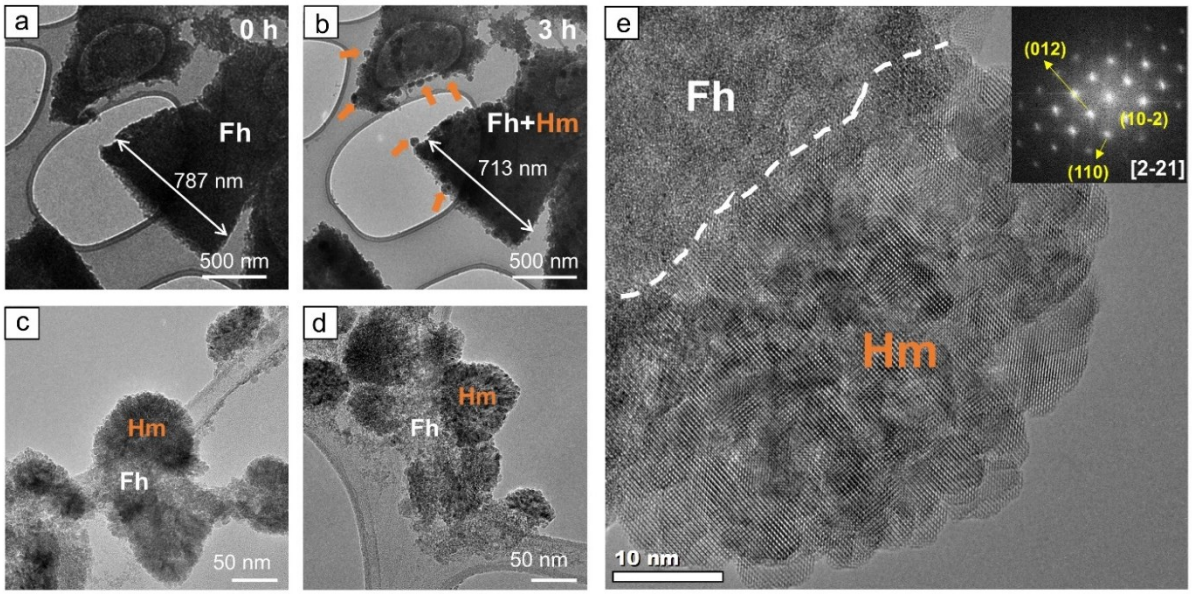

Figure 2.9. More examples of applying reference TEM grids to follow the growth of Hm on Fh as protruding half-spindles pointing towards the solution. a, Initial Fh aggregates. b, TEM image showing half-spindles of Hm growing on the original Fh aggregates in a. Shrinkage of the Fh

aggregates in a from 787nm to 713nm is highlighted. Arrows highlight the Hm growth over the Fh. c, d, Multiple examples of TEM imaging of half spindle Hm. e, HRTEM showing a half spindle Hm mesocrystal, the initial Fh, and the boundary between the two. Upon examination of over 30 half spindles, all were found to point away from the Fh and into the solution. The inset is an FFT of the Hm. Note that only Hm spindles on the edges of the Fh aggregates can be used to determine whether or not the spindles point towards the solution, due to the nature of the 2D projection in TEM.

2.5.4 *Apply rhom Hm seeds as a marker to monitor crystallization*

We used the reference TEM grid to monitor the phase transformation from Fh to Hm. We can also use rhom Hm seeds as reference to probe the phase transformation from Fh to Hm. Since rhom Hm seeds all have similar smooth surface, we can identify the change of the structure by comparison to the beginning rhom seeds with smooth surface. We start with rhom Hm seeds (Figure 2.10a and d), then mix it with the precursor for the synthesis of spindle Hm and heat it up to 90 degree. After a few hours, primary particles with a size of around 4 nms start to grow on the

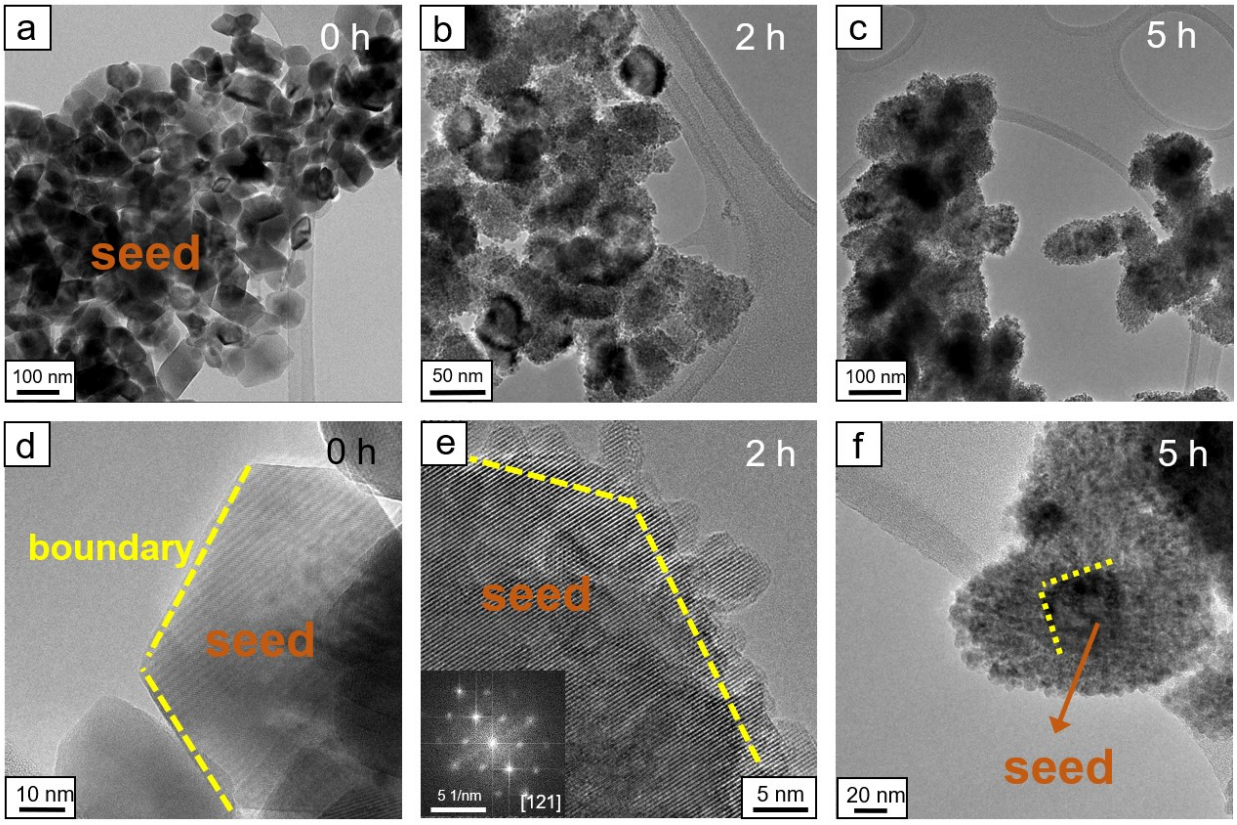

Figure 2.10. TEM imaging of Hm spindles grown over rhom Hm seeds. **a, d**, Rhom Hm particles with a smooth surface are used as seeds. **b, e,** Primary Hm particles that have grown over the seeds after 2 hours where inset FFT in (e) shows that the seed and the primary particles are crystallographically aligned. **c**, **f,** Formation of spindle Hm after 5 hours with the rhom Hm seeds still seen inside the spindles. The yellow dashed lines mark the boundaries of the rhom Hm seeds.

rhom Hm seeds (Figure 2.10b and e), and a clear boundary between the new formed primary particles and the Hm seeds is visible, as highlighted by the yellow dashed line in Figure 2.10e. The rhom Hm seeds act as a preferential substrate for the crystallization of Hm. The new forming particles are atomically aligned with the rhom Hm seeds. And eventually, spindle Hm will form with rhom Hm seeds in the middle of the spindle Hm. (Figure 2.10c and f) Based on this, we can arguably say that the addition of rhom seeds wouldn't affect the formation pathway of spindle Hm mesocrystal. We will later apply this procedure for our in situ LP-TEM experiments to investigate the crystallization pathway of Hm mesocrystal, since we can take the rhom Hm seeds as reference particles and keep track of their evolution.

2.5.5 *In situ liquid phase TEM/STEM investigate Hm crystallization*

We used different TEM imaging modes (TEM ad STEM) to probe the crystallization, which is a good way to validate the in situ results. In the STEM mode (Figure 2.11), we can resolve both the Fh and Hm. The Fh gradually dissolve over time, and new particles start to form on the Hm seeds. In the TEM mode, Fh particles are difficult to resolve due to their low contrast in the TEM mode, but the spatial resolution for the Hm is much better (0.3nm/pixel vs. 1.7nm/pixel). We find that the Hm particle didn't form directly on the Hm seed surface, but certain distance away from the surface and then attach to the seeds. One good example of this gap is highlighted in figure 2.12 c, in which, at 7s, one particle nucleates (indicated by the arrow) some distance away from the HM/solution interface. The gap distance is highlighted in the enclosed image, about 2.4nm. The gap eliminates as the nuclei particle attached to the seed particle at 9s. The contact angle between the seed and the nuclei is over 90° at 9s, and the structure relaxes over time, and eventually the nuclei became a hemisphere structure at 14s. The growth of spindle takes longer time, and we were not able to image that long continuously due to the concern of beam influence, so we block the electron beam most of times, and only take a few snapshots in the middle to image the system as shown in Figure 2. 12e. It highlights the nucleation of tiny particles a few nms away from the Hm/solution interface and attach to the seed particles, before it grows toa spindle Hm (15min). Due to the 2D projection nature of TEM and limitation of spatial resolution in the liquid phase TEM, we are not able to identify every new-born particle. So we can't exclude the possibility of heterogeneous nucleation over the seed particle. Nevertheless, some of the nucleation events are clearly captured to be a few nm away from the Hm/solution interface, followed up with attachment to the seed particle. Whether the new Hm particles are coaligned upon nucleation, align during attachment, or attach with some misalignment followed by elimination of defects, as documented

in other cases of OA [10, 81], cannot be discerned from these experiments. In conclusion, by applying LP-TEM we have revealed a new crystallization pathway which involves near interface nucleation and attachment during the formation of spindle Hm mesocrystal. The near-interface nucleation happens not on the Hm surface, or in the bulk, but about a few nms away from the Hm/solution interface.

The Fh seems to act as buffer to provide the source and set the concentration of solute ions from which new Hm primary particles form based on the in situ results and referenced TEM grid results. As long as Fh particles are present, the solute concentration remains fixed at the solubility of Fh ensuring that the Hm particles form at constant supersaturation as the Fh dissolves to replace the ions taken up by the growing Hm.

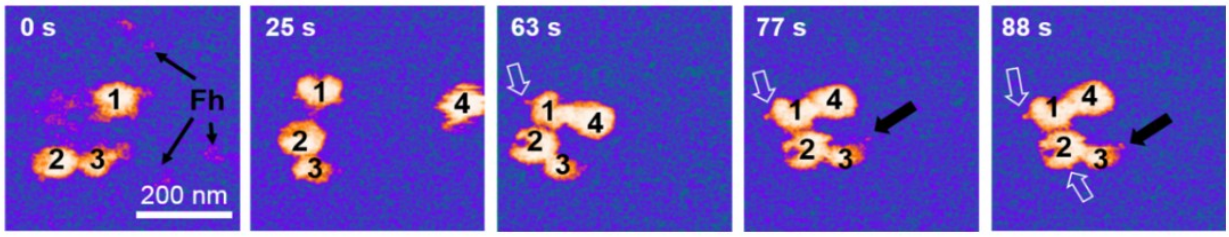

Figure 2.11. STEM observation of dissolution of Fh and growth of domain particles close to the Hm/solution interface. Fh is visible in the beginning as highlighted at 0s, New Hm particles appear in the field of view as highlighted by the number 1-4. The arrows indicate the new-born Hm formation close to Hm seed.

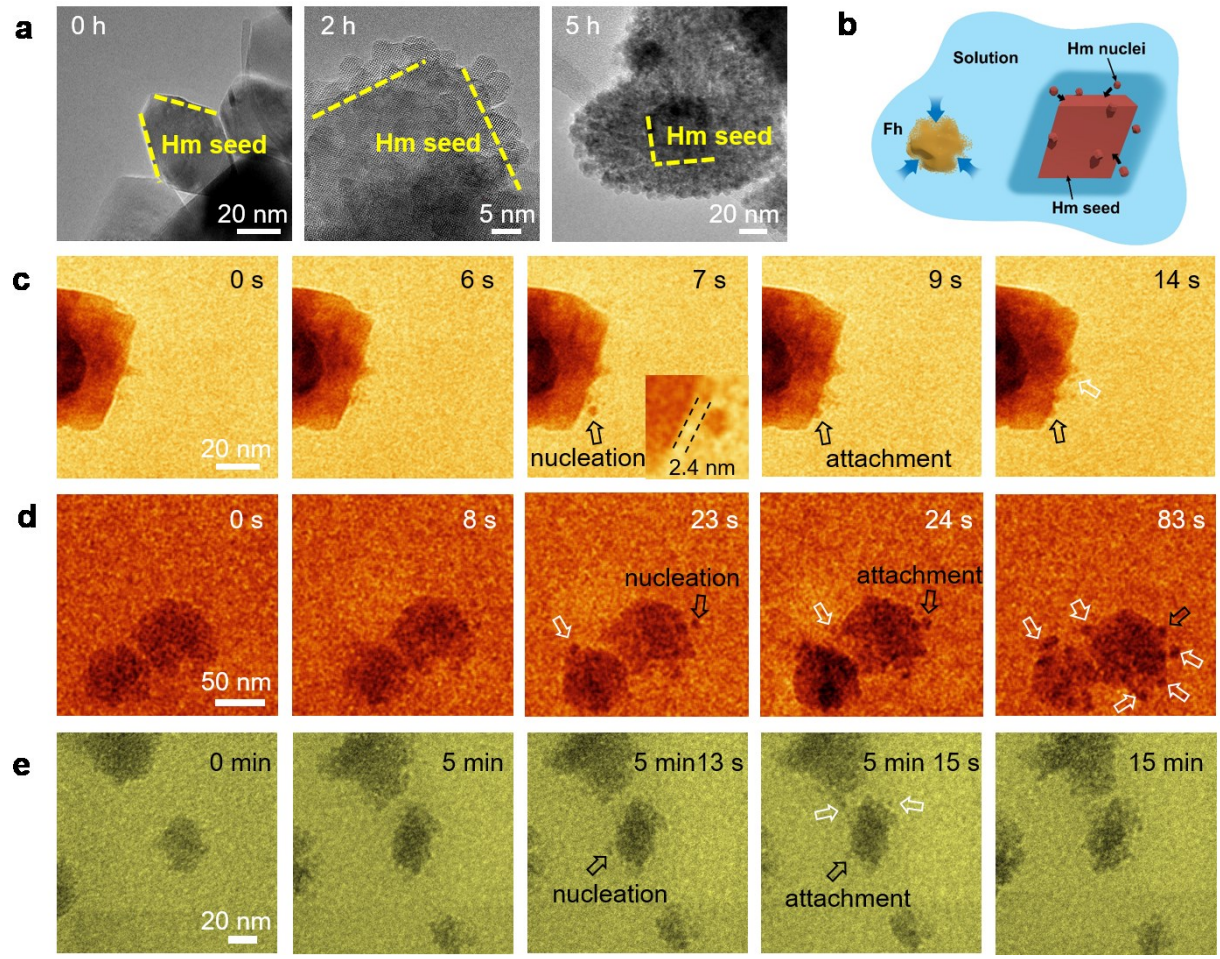

Figure 2.12. LP- TEM observation of Hm nucleation close to the seeded Hm/solution interface and followed-up attachment at 80 °C. a, Hm seeds with a smooth surface in the beginning and decorated with primary particles after 2 hours, which is confirmed by ex situ TEM. b, Cartoon showing the dissolution of Fh, and near-interface Hm nucleation and attachment to Hm seeds. c and d, TEM observation of Hm nucleation close to the Hm/solution interface and aggregation. The distance of about 2.4 nm is highlighted in the b, 7s. The black arrow indicates the same Hm nuclei from nucleation to aggregation to the big particle. The while arrows highlight other new-born particles. e, TEM observation of growth of a spindle Hm. Electron beam was blocked most of time in the experiment, while, only applied occasionally to take snapshots of the system.

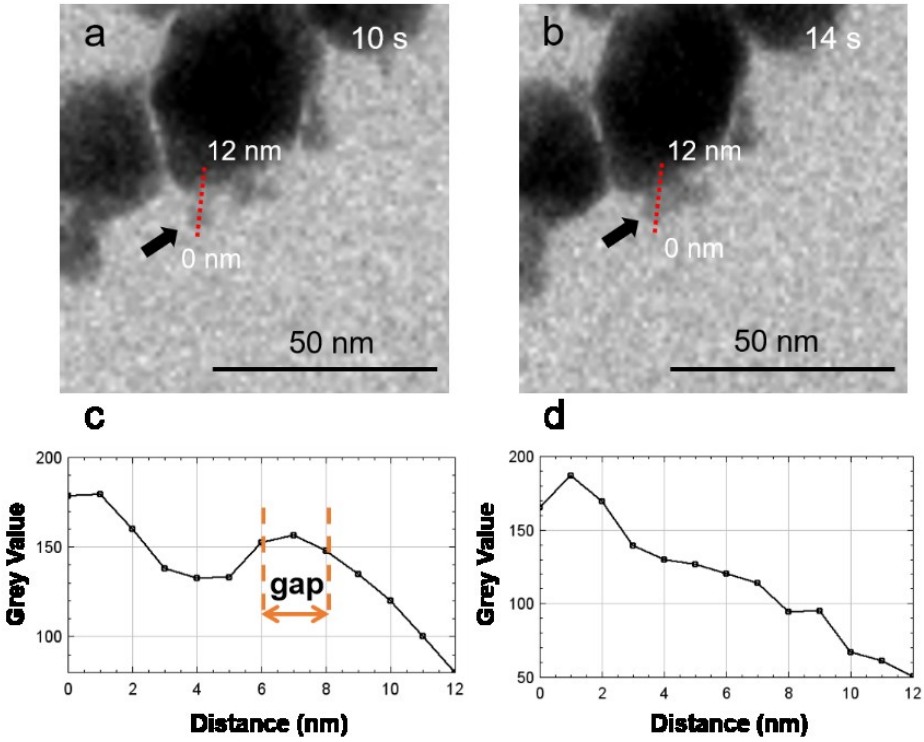

Figure 2.13. Analysis of the gap size between a Hm seed and a nucleus and its elimination over time during in situ TEM. a, TEM image of spheroidal nucleus occurs close to the seed surface indicated by the arrow. b, TEM image of the nucleus attaching to the seed particle over time. c, Line profile along the red dash line in a, measuring the gap size between the nucleus and the seed. d, Line profile along the red dash line in b, demonstrating elimination of the gap over time.

As the thickness of the liquid impacts in situ electron diffraction (ED) and energy-dispersive X-ray spectroscopy (EDX) measurement of the system, we carefully disassembled the windows (enclosing the samples) after the in situ experiment, air-dried the silicon nitride chip, and put it back to TEM for more analyses. The spindle Hm are clearly demonstrated in the STEM imaging (Figure 2.14a). The chemical composition of the spindle is iron and oxygen, as shown in the EDX mapping (Figure 2.14b and c). We also performed ED on the spindle aggregates, which shows the diffraction ring of Hm (104) and Hm (012) as shown in Figure 2.14e.

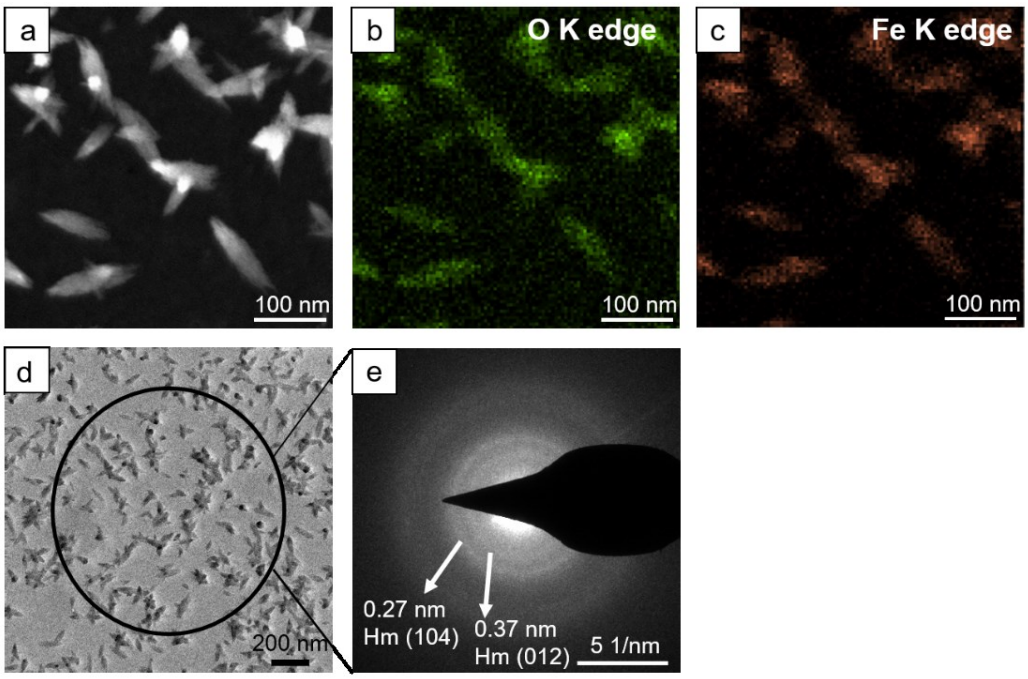

Figure 2.14. Post-mortem analyses of products after disassembly of the liquid cell chips. The liquid cell chamber was aged at 80 °C for 5 hours in the TEM. a, STEM image of spindle Hm; the porous structure can be observed, but with poor contrast due to the background from the 50 nm SiN window. b, c, STEM-EDX mapping of the spindles in (a) showing oxygen and iron distributions only. d, TEM image of spindle Hm at low magnification showing uniform distribution of spindle Hm on the SiN window. e, Corresponding selected area diffraction from spindles in (d) highlighting two diffraction rings of Hm from (012) and Hm (104) planes with an inter-plane distance of 0.37 nm and 0.27 nm, respectively.

What is the role of Ox then? In solution, Ox binds with Fe^{3+} to make Ox complexes the dominant Fe-species down to pH values well below those used here [82]. Ox is therefore capable of accelerating Fh dissolution, though it does not appreciably shift the bulk Fe^{3+} activity, which still remains fixed at the solubility of Fh. However, the difference in Hm growth with and without Ox shows it also acts at the Hm surface: In the absence of Ox, Hm forms large faceted crystals (Figure 2.10a and d, and Figure 2.12a), while in its presence only spheroidal particles that do not advance beyond ~ 5nm in diameter are formed. Consequently, one role of Ox is to stabilize Hm nanoparticles and inhibit their growth. Moreover, in the absence of Ox, we find no evidence for

aggregation of Hm particles, suggesting that Ox resides at the Hm particle surface and biases the local chemistry to promote Hm nucleation and possibly assist in OA.

To test the above hypothesis, we first measured the degree to which Ox binds to the common (001) and (012) faces of Hm using attenuated total reflection Fourier transform infrared (ATR-FTIR) spectroscopy and ion chromatography[77]. (Figure 2.15a) The results show that the Hm (001) and (012) surfaces develop high Ox coverages of 4.38 and 12.17 Ox molecules per nm^2. Calculations using plane wave density functional theory gave similar results of 4.30 and 13.92 Ox anions per nm^2 at full coverage with Ox exhibiting strong bidentate end-on mononuclear binding on both Hm faces consistent with prior analyses[83-84].

We then performed classical density functional theory (cDFT) calculations, which are ideal for modeling the chemical potential of ions within complex multicomponent electrical double layers, to determine the impact of Ox on the Fe^{3+} concentrations near the interface (Figure 2.15c), as well as the corresponding Hm-Hm interparticle forces (Figure 2.15d). Following an approach that separates contributions to the total chemical potential describing entropy of mixing (ideal chemical potential) and all interfacial interactions (potential of mean force), our cDFT analyses show that the driving forces for Fe^{3+} accumulation at the surface of a Hm particle exhibit a qualitative difference in Fe^{3+} potential of mean force with and without Ox in solution. Without Ox, potential of mean force is dominated by the short-range Fe/surface interactions and the shape of its distance dependence predicts a barrier-free process of ion addition.

2.5.6 *ATR-FTIR and simulation about ion distribution near interface*

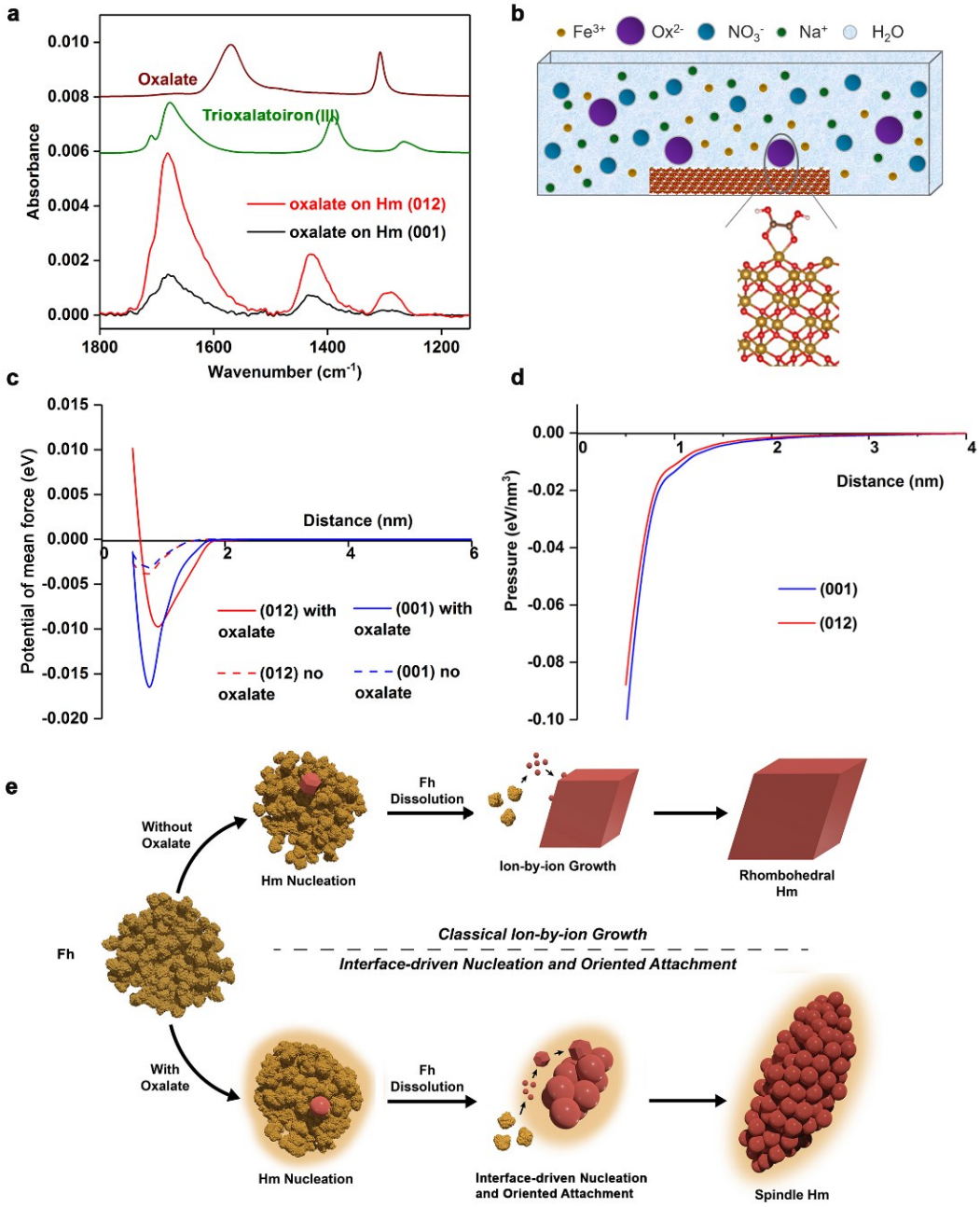

Figure 2.15. Structure and thermodynamics of Hm/solution interface. a ATR-FTIR spectra of Ox adsorbed on Hm (001) vs. Hm (012). The offset spectra of trioxalatoiron (III) and the aqueous Ox anion are models for inner-sphere bidentate-mononuclear and outer-sphere water-separated binding, respectively (24). Comparison of the spectra of adsorbed Ox to these reference spectra indicates that Ox is predominantly bound to Hm through direct surface Fe (III) coordination in a bidentate mononuclear fashion. b Schematic of the solution speciation and simulation set-up. c Average potential of mean force of Fe ions vs. distance away from the surface with and without

Ox. d Distance dependence of particle-particle interaction showing barrier free attraction, which biases the aggregation. e Schematic of ion-by-ion growth vs. interface driven nucleation and oriented attachment, without oxalate and with oxalate, respectively. In the latter case, the process is as follows: Hm first nucleates within the Fh aggregate leading to depletion of solute ions in the solution. Thus Fh begins to dissolve to maintain the equilibrium solution speciation. The oxalate/Hm/solution interface then drives nucleation of new Hm particles near interface and the newly formed particles undergo OA to attach to the growing spindle, while. Fh continues to dissolve to maintain equilibrium. After all the Fh is consumed, the Hm particles in the spindle continues to coarsen.

In contrast, in the presence of Ox surface complexes, which create a layer of negatively charged discrete sites, the potential of mean force of Fe^{3+} is dominated by the entropic ion correlation interactions, which stabilize the interfacial diffuse layer of solvated Fe^{3+} hindering diffusion and deposition on the surface. Solvation interactions contribute to the chemical potential barrier. These two factors lead to Fe^{3+} accumulation approximately 1 nm away from the surface, which is approximately the same region in which nucleation of new Hm particles is observed (Figure 2.15c). While the chemical potential of Fe^{3+} relative to bulk Hm must be constant throughout a well-mixed system, these results predict that the solution chemistry in the interfacial region differs from that of the bulk and the greatest difference occurs about 1 nm from the surface. Nucleation rates in the interfacial region may be enhanced for both kinetic and thermodynamic reasons, which have been discussed in detail below.

2.5.7 *Rationalization of the enhanced near interface nucleation and growth*

The rate of nucleation within the framework of classical nucleation is given by:

$$J = \beta Z C_0 e^{\left(-\frac{\Delta G^*}{kT}\right)}$$

where, for spherical particles:

$$\Delta G^* = \frac{16}{3}\pi\alpha^3(\Omega/\Delta\mu)^2$$

$$\Delta\mu = \mathrm{kT}\sigma$$

Here β is a kinetic pre-factor, Z is the Zendelovich factor, C_0 is the equilibrium solute concentration, ΔG^* is the height of the free energy barrier, k is Boltzmann's constant, T is the temperature, α is the interfacial free energy, Ω is the molecular volume in the solid, Δμ is the chemical potential of the solution relative to the solid. For Hm, $\Omega = 25.2$ Å^3.

The value of σ for precipitation of Hm in the bulk solution (σ_b) is set by the solubility of Fh [85]:

$\log(\text{Ksp(Fh)}) = -38.6 \pm 0.6$;

$\log(\text{Ksp(Hm)}) = -41.99 \pm 0.39$

$\sigma_b = ln\left[\frac{Ksp(Fh)}{Ksp(Hm)}\right] \approx ln\left(\frac{C_{Fh}}{C_{Hm}^b}\right) \approx \ln(1000) = 6.9$

where C_{Fh} and C_{Hm}^b are the solubilities of Fh and Hm in the bulk solution. Thus the chemical potential relative to Hm in the bulk solution is:

$$\Delta\mu_b = 6.9kT$$

Three different factors could lead to enhancement of the nucleation rate near the interface: 1) a decrease in α, 2) an increase in Δμ, and 3) an increase in β.

Nucleation enhancement due to the interfacial energy differences. If we assume that the difference in solution chemistry in the bulk from that in the interfacial region leads to a reduced value of *a*, and all terms in *J* are the same except for α. Thus the ratio of the nucleation rate at the interface to that in the bulk solution becomes:

$$\frac{J_i}{J_b} = e^{B\alpha_b^3\left(1-\frac{\alpha_i^3}{\alpha_b^3}\right)}$$

$$B = \frac{\frac{16}{3}\pi\Omega^2}{(kT)^3\sigma^2}$$

For the pH of our experiments, this approach gives a value of α_b = 0.3 J/m^2, which is considerably smaller than estimates from literature, which is around 0.75 J/m^2 .[62] However, larger values of α_b will cause the magnitude of the enhancement to be even larger, in this case, by many orders of magnitude. Consequently, we take the smaller value to calculate a conservative estimate of the degree of enhancement. If we take α_b = 0.3 J/m^2 we get an estimate for ΔG of 83.6 kT. We calculate that if α_i is 1% smaller than α_b, $\frac{J_i}{J_b} = e^{2.6}$ or 13, and if the difference is 5%, the ratio becomes $e^{19.6}$ or 3.3 E8, which is enormous difference and may lead to the preferential nucleation close to the interface.

Nucleation enhancement due to the solubility difference. There are a number of studies that suggest the solubility of material in a confined space can be reduced. I) When an AFM tip is brought to the surface of a KH_2PO_4 (KDP) crystal at moderate humidity, a micron-scale meniscus forms at the contact, while the rest of the surface is covered with one to two monolayers of water. The result is deposition of KDP within the meniscus showing that that equilibrium activity differs in the bulk fluid of the meniscus than in the confined water film. Similarly, placing the tip over groves leads to the grooves filling in [86]. II) Using surface X-ray scattering measurements, Deng et al found that in barium carbonate solutions, barite nanoparticles form on negatively charged self-assembled monolayers when the solution itself is undersaturated with respect to Barite. The organic-water interface was believed to induce the enrichment of ions close to the interface and increase the local saturation state [87]. III) Using liquid phase TEM, Jin et al found that, during aggregation of Au nanoparticles, necks between particles form while the particles are still separated by around 1 nm by, which suggests a local supersaturation enhancement [88]. The same effect is seen with ZnO (Liu et al., In review). Because the chemical potential of a solution species

must be the same everywhere, the implication of these studies is that the solubility of the solid is different in the confined regions than in the bulk.

Assuming C_{Hm}^{i} (Hm solublity close to the interface) is smaller than C_{Hm}^{b} (Hm solubility in the bulk), we have that $\sigma_b = ln(C_{Fh}/C_{Hm}^{b})$ while $\sigma_i = ln(C_{Fh}/C_{Hm}^{i})$. Then the degree of enhancement becomes:

$$\frac{J_i}{J_b} = e^{\frac{B\alpha_b^3}{\sigma_b^2}\left(1-\frac{\sigma_b^2}{\sigma_i^2}\right)}$$

Where B is defined above. Taking α_b is 0.3 J/m^2 as described above, if C_{Hm}^{i} is 5% smaller than C_{Hm}^{b}, $\frac{J_i}{J_b} = e^5$ or 148, while if C_{Hm}^{i} is 10% smaller than C_{Hm}^{b}, J reaches e^{10} or 22,000.

Nucleation enhancement due to differences in kinetic pre-factor. We assume the kinetic pre-factor is linearly related to the concentration of the solute, because the collision rate of ions with a cluster will be proportional to their concentration. For the Hm-oxalate interface, the solute concentration is increased over that in the bulk, so the degree of enhancement is:

$$\frac{J_i}{J_b} = \frac{C_{Hm}^{i}}{C_{Hm}^{b}}$$

The increase in concentration can be calculated from potential of mean force obtained from the cDFT calculations. For the bulk, $\Delta\mu_b = kTln\left(\frac{C_{Fh}}{C_{Hm}^{b}}\right) = 6.91kT$. The decrease in potential of mean force due to the Ox-solution interface increases this driving force for the (012) and (001)

faces, respectively, by 0.009eV and 0.017eV, leading to $\Delta\mu(012) = kTln\left(\frac{C_{Fh}}{C_{Hm}^{012}}\right) = 7.27kT$, and $\Delta\mu(001) = kTln\left(\frac{C_{Fh}}{C_{Hm}^{011}}\right) = 7.57\ kT$. The resulting values of $\frac{J_i}{J_b}$ are then $e^{0.36} = 1.4$ and $e^{0.66} = 1.9$ for (012) and (001), respectively, showing that this effect is minor.

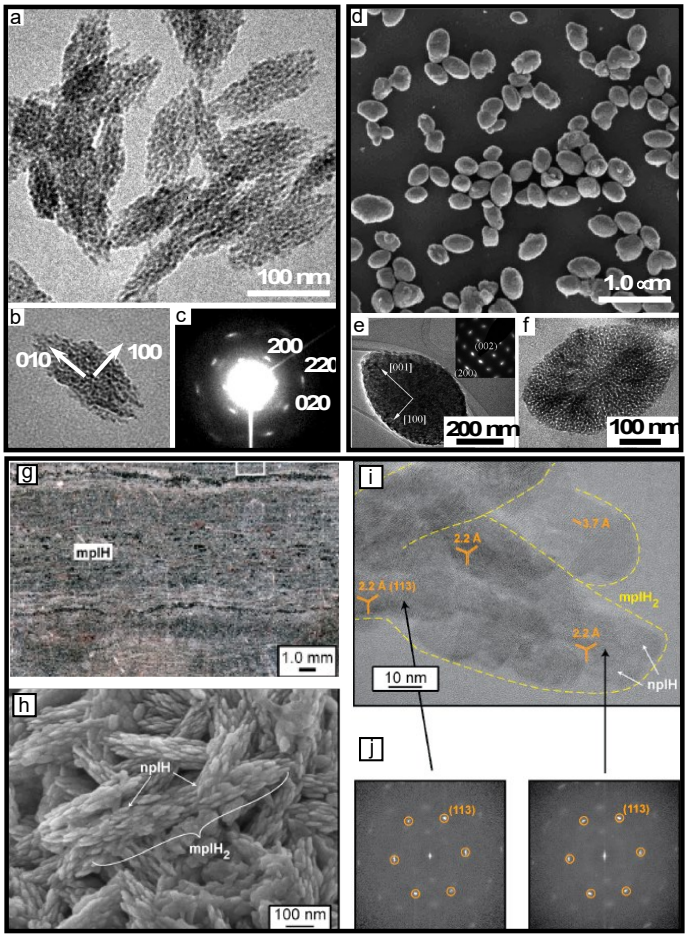

Figure 2.16. Literature examples of spindle-shaped mesocrystals in both functional materials (a-f) and geological field samples (g-j). **a, b,** TEM images of CuO mesocrystals[89]. **c,** Selected area electron diffraction (SAED) from particle in (b). **d-f,** TEM images of TiO_2 (anatase) mesocrystals [90]. (Inset of e shows SAED from the particle in (e). **g,** Optical micrograph of band comprised of hematite mesocrystals found in a banded iron formation in Hamersley Province (Australia)[91]. **h, i,** TEM images of the spindle-shaped hematite within the band in (a). **j,** FFT patterns from particles in (i).

Evidence for interfacially driven nucleation due to local chemical gradients has been reported for other systems. An investigation of Au nanoparticle growth concluded that when these pH

sensitive chemical gradients become comparable, near-surface nucleation followed by particle attachment becomes the dominant growth pathway[92]. The effect of organic films at mineral interfaces on concentrating cations was also invoked to explain the formation of barite in the oceans, which are globally undersaturated with respect to the mineral[87]. Nucleation and growth of barite nanoparticles was shown to occur in slightly undersaturated solutions on COOH- and SH-terminated films due to concentration of Sr^{2+} at the charged organic interface. A number of other studies have attributed heterogeneous nucleation due to chemical transformations of precursors near the interface, including reduction of Au and Pd during seeded nanoparticle synthesis [93] and Ni films during electrodeposition from NiCl solutions[51].

Our results also provide a possible explanation for unusual morphologies of naturally occurring iron oxides. The most obvious examples are the strikingly similar spindle-shaped mesocrystalline Hm recently discovered in the classic Precambrian banded iron formations of Australia[91] , as well as the so called, “rainbow Hm”, whose name reflects the natural iridescence of the mineral, is composed of spindle-shaped Hm 200-300 nm in length and 50-60nm in width[70]. (Figure 2.16 g-i) Other studies on iron oxide-rich tropical soils reported Hm and goethite consisting of nanoparticle aggregates, including spindles of similar dimensions[94]. In our study, spindle-shaped Hm formed at temperatures as low as 40°C, suggesting that the process observed here is feasible in these natural settings, where organic constituents, including oxalate, are abundant.

2.6 Conclusion

In an oxalate free solution, the resulting Hm crystals are well faceted Rhombohedron, but in the presence of oxalate, Hm forms a nanoporous spindle-shaped mesocrystal elongated along [001]. The nanometer sized domains are atomically aligned to each other forming a single crystalline porous structure. We have applied in situ heating liquid phase TEM to investigate the process of

Hm crystallization from Fh. We directly observed the nucleation of new Hm close to the Hm/solution interface with a gap, and followed by attachment to the Hm seed at a solution temperature of 80 degree Celsius. The measured gap size is around 2nm. By blocking the beam most of times, we are able to observe the growth of the spindle in situ. Post analyses after disassembling the liquid cell by using EDX mapping and electron diffraction confirmed the growth of spindle Hm in the liquid phase TEM. In addition, we developed a freeze-and-look approach using indexed TEM grids to cycle samples between the growth reactor and the TEM in order to track the pathway of crystallization over time, the results were consistent with those of the in situ experiments and confirmed that the Fh serves as a buffer and the Hm grow by creation of new particles in the solution near the Hm interface. Based on ATR FTIR measurements of the relative binding strength of oxalate to the (001) and (012) faces, and calculations of chemical potential gradients near the interface, we propose that oxalate plays the role of inhibiting classical monomer-by-monomer growth of the Hm particles while promoting the nucleation of new Hm particles at the Hm/solution interface. Consequently, by inhibiting classical growth and driving all nucleation to occur near existing Hm particles, the ligands bias the growth process towards oriented attachment. Looking beyond iron oxide, the findings reported here and the comparisons to other systems suggest that an interface-driven process of CPA may be a widespread phenomenon in both synthetic and natural environments.

Chapter 3. Addressing some of the technical challenges associated with liquid phase S/TEM studies of particle nucleation, growth and assembly

3.1 Introduction

In situ liquid phase scanning/transmission electron microscopy (S/TEM) was developed to image materials in their hydrated state [39-40, 95]. A typical fluid cell design provides a nm-scale thick water layer sandwiched between Si wafers, which include electron transparent Si3N4 windows separated by a spacer of similar thickness. The cell is sealed by either O-ring or glue to make it compatible with the high vacuum of the electron microscope. Many exciting studies have been pursued in a wide range of fields, including nucleation and growth of crystals [41, 96-98], etching [42-44], particle assembly and fusion [45-47], bubble formation and dynamics [48-49], electrochemistry [50-51], and biomolecule interactions [52-53].

Though powerful, many artifacts and uncertainties are associated with LP-TEM and limit the interpretation of the results from in situ experiments. Woehl and coworkers [99] systematically documented many of the artifacts induced by beam water interactions i.e. radiolysis and recommended limits on dose rates for minimizing these effects. Abellan and coworkers [100] presented several factors influencing quantitative results from LP-TEM, including electron dose applied, imaging mode, acceleration voltage, beam-induced solution chemistry changes, and the specifics of solution reactivity. More importantly, they established some methods to achieve more reliable and quantitative results, highlighting the need for methods of measuring the amount of radiation damage and the importance of establishing equivalent settings for the electron optics amongst different instruments. Parent and coworkers [101] applied anomalous diffusive motion

analysis to analyze video graphic data on particle motion. They highlighted the inhibited nature of the particle dynamics in LP-S/TEM and careful analyses required to reach a sound conclusion.

3.2 Syntheses and methods

3.2.1 *Synthesis of hematite (Hm) and akageneite*

The synthesis of akaganeite nanorod and rhombohedral shaped Hm is by aging a 0.02 M $FeCl_3$ solution at 100 °C in a Teflon bottle. Akaganeite nanorod forms first before transformation to rhom Hm. The bottle is well sealed to minimize water evaporation. Synthesis in glass bottles were also performed and compared but found detectable amount of silicon incorporated. The solution after aging at 100 °C for 10 hours is a mixture of akaganeite and Hm. [102]

3.2.2 *Synthesis of gold nanoparticle for the immobilization and the silanization of SiN windows*

Au nanoparticles (20 and 50 nm diameter) were synthesized by boiling a freshly prepared 50 ml $HAuCl_4$ solution (0.01% by weight), then adding 0.5 to 1.0 ml sodium citrate solution (1% by weight)[103]. Au nanoparticle seeds (3-5 nm diameter) were grown by preparing a 20 ml $HAuCl_4$ (2.5×10^4 M) and sodium citrate (2.5×10^4 M) solution, followed by the rapid addition of 0.6 ml ice-cold $NaBH_4$ (0.1 M) solution while stirring [104]. A 3% by volume solution of APTES in water was prepared and heated to 75 °C. SiN windows were cleaned and activated/hydrolyzed by oxygen plasma etching for 5 min at 10.5 W, before immediately being immersed in the prepared APTES solution and left for one hour. [105]

3.2.3 *Synthesis of gold nanoparticle for the flowing LP-TEM experiment*

In a glass vial with Snap-on caps (100 ml volume) aqueous CTAB solution (7.5 ml, 0.1 M) and chloroauric acid (250 µl, 0.01 M) were mixed and tempered in a water bath to exact 29 °C. In a typical synthesis, the solution is allowed to rest for more than one hour to ensure the correct temperature. Afterward, ice-cold $NaBH_4$ solution (600 µl, 0.1 M) was added under vigorous stirring, and the stirring bar was removed after 1.0 min. The seed solution was allowed to rest for another 3 hours to decompose excess $NaBH_4$. The seed solution was diluted ten times (300 µl seed solution into 3.0 ml Milli-Q water) before use. In a glass vial with snap-on caps (100 ml volume) Milli-Q water (32.0 ml), CTAB solution (6.4 ml, 0.1 M) and chloroauric acid (800 µl) were mixed and tempered in a water bath to exact 26.0 °C. Usually, the solution was allowed to rest for more than one hour to ensure the correct temperature. Afterward, 30.0 µl of the diluted seed solution was added under vigorous stirring. The stirring bar was removed after 2 min, and the reaction dispersion was kept tempered overnight.

3.2.4 *LP-TEM assembly and imaging*

LP-TEM was performed with an aberration corrected FEI Titan at 300 kV and a FEI Tecnai G^2 F20 at 200 KV. The dose for the microscopy were calibrated using a Faraday cup. The calibration is based on the difference between the current on the Faraday cup and the current on the phosphor screen in the TEM. The tip of the holder is carefully cleaned in the beginning of experiments. The cleaning strategy is varied based on the history of the chemicals used. Generally, it is sonicated in HNO_3 (0.1 mM) and H_2O repeatedly for several times, and finally immersed in the H_2O at 80 degree for 1 hour. Details of the LP-TEM procedure can be found from previous work [54].

LP-TEM was performed with an aberration corrected objective FEI Titan at 300 kV and a FEI Tecnai G^2 F20 at 200 KV. The dose for the microscopy is calibrated using a Faraday cup. The calibration is based on the difference between the current on the Faraday cup and the current on the phosphor screen in the TEM. The tip of the holder is carefully cleaned in the beginning of experiments. The cleaning strategy is varied based on the history of the chemicals used. Generally, it is sonicated in HNO_3 (0.1 mM) and H_2O repeatedly for several times, and finally immersed in the H_2O at 80 degree for 1 hour. Details of the LP-TEM procedure can be found at [54].

For the flowing LP-TEM experiment, a Hummingbird holder with dual inlet and one outlet were used. A collection vial connected to the outlet was used to collect the solution. The flowing rate is 5 μl / min for the EG, which has been tested in the vacuum pumping before every flowing LP-TEM experiment in the TEM. After the in situ experiment, we carefully disassemble the two chips by immersing them into the water, and shaking the container gently. The chips are then put into a specific TEM holder for post analyses, including electron diffraction, HRTEM and EDX mapping. Optical microscopy is used to help identify the exact location of the TEM viewing areas (50 x 50 μm) on the SiN window (250 x 50 μm). For the heating LP-TEM experiments, two different methods have been used. First one is to use a k-kit glued liquid chamber combined with a Gatan heating holder. The glued chamber is sealed first and put to a vacuum chamber to degas for 2 hours. The loading of the chamber onto the Gatan heating holder is very similar to the loading of a normal TEM grid. Second one is to use a heating holder from Protochip and Hummingbird Scientific, the configuration of which is very similar to a normal LP-holder. The only difference is that the heating holder needs chips with heating elements embedded in the chips and a controller box to tune the temperature [58, 106].

3.3 Results and conclusion

3.3.1 *TEM/STEM mode in liquid phase TEM*

As has been discussed previously [101], the optimum imaging mode used in LP-TEM experiments depends on a number of factors. TEM generally gives higher time resolution than STEM, but STEM is preferred when dealing with high Z elements, which have enhanced contrast in STEM mode. For a thick liquid layer, useful images are difficult to obtain by TEM, but can be obtained using STEM if the sample of interest has high Z elements. However, for a thin liquid layer, TEM has better temporal and spatial resolution, which is likely the main reason why most LP-TEM studies have been done in this mode.

Figure 3.1 illustrates an example of the differences in the effect of beam irradiation in STEM and TEM mode for the growth of Au nanoparticles in a solution $HAuCl_4$ and trisodium citrate. The particles tended to grow with a dendritic morphology (Figure 3.1A) in STEM mode with a beam current of 0.31 nA (pixel size of 1.9 nm^2, pixel dwell time of 1 μs, frame time of 0.3 s, and average dose rate of 496 $e/nm^2/s$). However, after switching to TEM mode with a beam current of 0.70 nA (exposure time per frame of 1.05 s and dose rate of 221 $e/nm^2/s$), the particle growth morphology changed to polyhedral (Figure 3.1B). Two representative particles from each case are highlighted in Figure 3.1C, where the time dependence of the contour of the particle is drawn. Plots of the projected area of the gold particles as a function of time (Figure 3.1D) show that growth in STEM mode is faster than that in TEM mode.

Previous studies on noble metal nanoparticle growth showed that the electron beam creates a number of solution species, including hydrated electrons and various radicals, which can act to

reduce metal ions and create a locally high supersaturation [55, 96]. Considering the fact that STEM uses a highly focused electron beam — and thus the instantaneous dose rate is several orders of magnitude higher than that in TEM mode — it is not surprising that the solution reaches supersaturations for which mass transport is inadequate to keep pace with surface kinetics, leading to surface instabilities that are well known to drive dendritic growth, particularly in the diffusively constrained environment of the TEM liquid cell. In contrast, for TEM mode, the parallel, continuous flux of electrons delivered to the sample gives an instantaneous dose rate several orders

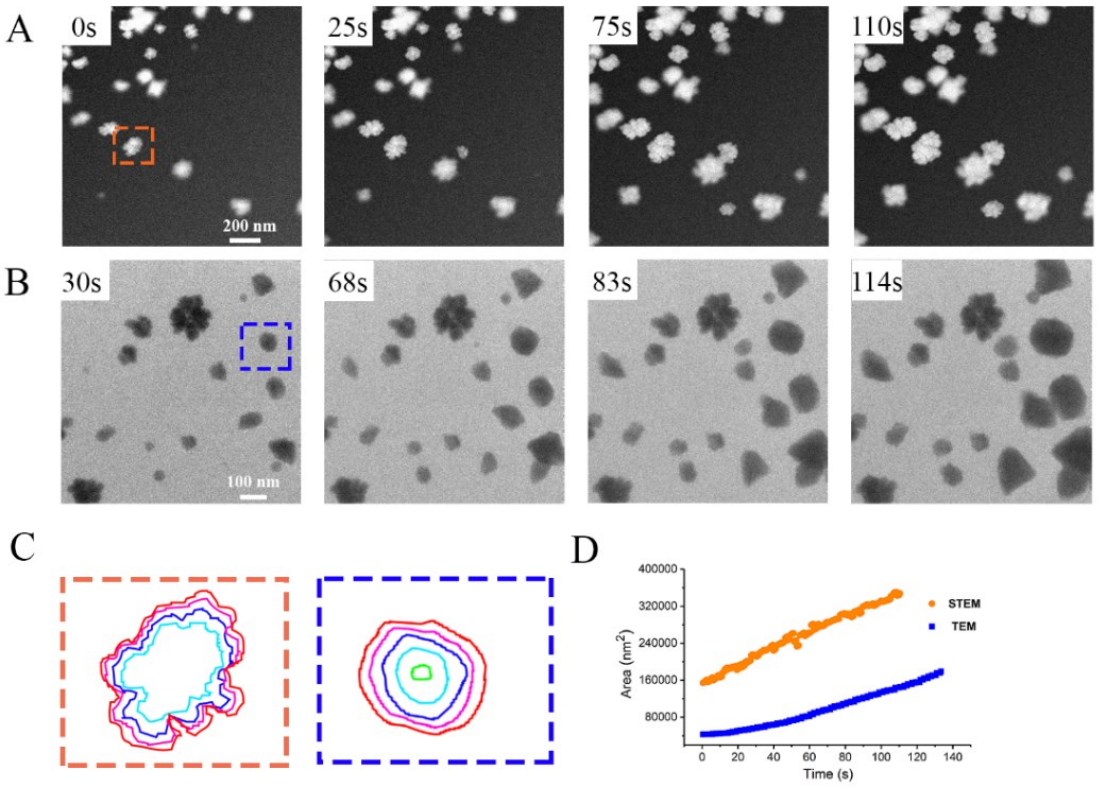

Figure 3.1. Growth of gold nanostructures in STEM and TEM mode. The initial solution is a mixture of $HAuCl_4$ (6.7 mM) and trisodium citrate solution (13.4 mM). (A) Dendritic Au growth in STEM mode. Accelerating voltage is 200 kV with an electron beam current of 0.31 nA, a 1 µs pixel-dwell time and a pixel size of 1.9nm2, giving an average dose rate of 496 e/nm^2/s and an instantaneous dose rate of 1.0 x10^9 e/nm^2/s. (B) Effect of switching to TEM mode right after the dendritic growth in the STEM leading to polyhedral Au particle growth with an accelerating voltage of 200 kV, beam current of 0.7 nA, exposure time per frame of 1.05 s and dose rate of 221 e/nm^2/s. (C) Contour maps showing growth of the dendritic (left, STEM mode) and polyhedral

(right, TEM mode) gold particles highlighted in (A) and (B). (D) Projected area verse time for the growth in STEM and TEM modes from (A) and (B).

of magnitude smaller than STEM, making it difficult to reach the high supersaturation needed for such instabilities. In the experiment summarized in Figure 3.1, although the average dose rates noted above are the same to within about a factor of two (221 vs 496 e/nm^2/s), the transient dose rate in STEM mode is more than six orders of magnitude larger at 1.0 ×10^9 e/nm^2/s. The observed instability in nanoparticle growth is related to the higher metal nanoparticle nucleation rates observed for STEM mode vs TEM mode at similar average dose rates described by Abellan et al.,[100] who made an extensive comparison between the dose rates during TEM and STEM imaging.

The results show that the change from STEM to TEM leads to different growth modes, with STEM driving interface instabilities that lead to dendritic morphologies, even though the accelerating voltages are the same in both cases and the beam current is two times larger in TEM mode. Consequently, different imaging modes are recommended to apply to the system to gain better understanding about how different parameters (dose, dose rate, ways of electron delivered, magnification, etc) affect the system.

3.3.2 *Mitigating beam-induced dissolution*

While the beam can drive growth front instabilities of metal nanoparticles during nanoparticle growth when the dose rate is sufficiently high, for many materials the effect can be exactly the opposite with the beam driving nanoparticle dissolution upon exposure to the beam. This problem is especially problematic for oxides — including oxides of iron, aluminum, cerium and vanadium — which commonly dissolve rapidly during LP-TEM [42, 107]. However, this effect is particularly detrimental for research into crystal growth mechanisms, whether by classical ion-by-ion addition, or through attachment of higher order species, including solution clusters or full-formed particles.

Consequently, systematic research on the mechanism of dissolution and approaches to mitigating the effect is needed.

Here, we use iron oxides as a model system to investigate beam-induced dissolution and ways to prevent or inhibit it. Iron oxides are amongst the most important near-surface minerals, they form many polymorphs and often exhibit replacement reactions, making a comparison of dissolution rates amongst the different polymorphs a potential window into the source of dissolution. Specifically, a mixture of hematite (Fe_2O_3) rhombohedrons and akaganeite (FeO(OH,Cl) nanorods shown in the ex-stiu TEM image of Figure 3.2A was exposed to the electron beam and tracked over time. At a dose of 96.2 e/nm^2/s, the akaganeite dissolved rapidly, but the hematite remained nearly undissolved (Figure 3.2B). Due to the thick liquid layer and fast movement of the nanorods during dissolution, we did not attempt to quantify the dissolution rate.

The atomic-scale mechanism of dissolution in these experiments is not known, but based on previous studies of akageneite dissolution using *ex situ* techniques [108], we assume that attack of the akageneite lattice by protons plays a role and that dissolution happens on the akaganeite /solution interface. Consequently, we pursued two strategies to inhibit dissolution. The first was to raise the pH to reduce the concentration of protons (Figure 3.2C). At pH 10.5, a regime in which akageneite is stable indefinitely at room temperature in the absence of the beam, barely any dissolution was detected for times up to hundreds of seconds. The second approach was to add the surfactant polyvinylpyrrolidone (PVP), which might be adsorbed on the crystal surfaces, thereby preventing proton assisted dissolution (Figure 3.2D).

As Figure 3.2 demonstrates, both of these approaches were successful in mitigating beam-induced dissolution. Although both hematite and akageneite exhibited significant degradation within the first 30 s of exposure at pH 5.5 in the absence of additives, increasing the pH to 10.5

prevented dissolution for hundreds of seconds — and even enabled growth to occur — while the introduction of PVP slowed the dissolution rate considerably. The results show that a rudimentary understanding of the mechanism of dissolution and phase stability can enable design of strategies to avoid dissolution either by adjusting the pH or by adding surface-active molecules.

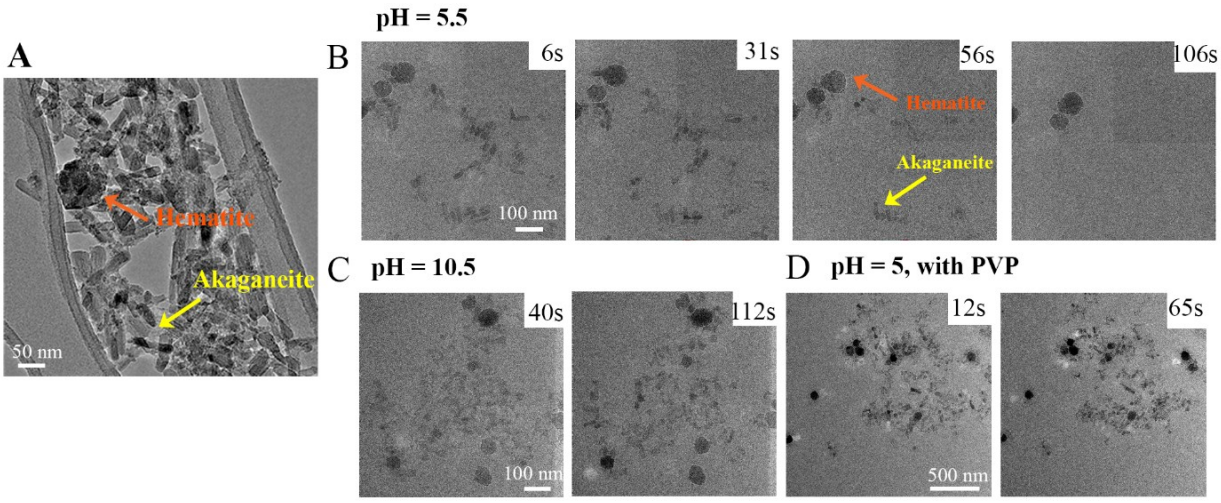

Figure 3.2. Comparison of dissolution behaviors in different solution chemistries. Beam current is 0.332 nA, giving a dose rate of 96.2 e/nm^2/s. (A) Ex-situ TEM images showing the nano-rods of akaganeite and polyhedral hematite. (B) Dissolution of akaganeite nanorods at initial pH value of 5.0 in TEM mode. (C) Changing the initial pH from 5.5 to 10.5 inhibits the dissolution of akaganeite (D) Adding PVP at a concentration of 0.5 % (w/v) into the initial solution also inhibits dissolution.

3.3.3 *Modifying particle adhesion to SiN windows in liquid phase TEM*

While numerous LP-TEM studies have been performed to explore nanoparticle growth and dissolution, many others have focused on the dynamics of nanoparticle aggregation or assembly. Although, in some cases, the electron beam is intentionally used to drive aggregation [47], its role in the aggregation dynamics has generally been the subject of debate [101]. A major challenge, both in resolving the role of the beam and in developing a general understanding of nanoparticle assembly is that nanoparticle mobility is typically hampered by their adhesion to the liquid cell membranes. One way to address this problem is to flow solution into the liquid cell that provides control over

particle mobility. Gold nanoparticles coated with Cetyltrimethylammonium bromide (CTAB) in water were first deposited onto the membrane of a liquid cell. Initially, the particles were largely immobile at a dose rate of 10.0 e/nm^2/s (Figure 3.3A-C). We then used a holder that allowed for liquid flow into the cell (Figure 3.3D) to introduce ethylene glycol (EG), which is a good solvent for CTAB. Approximately 40s after initiating the flow of EG to the fluid cell, which is the approximate time expected for flow to reach the tip of the holder in our system, we observed rapid movement of the particles making their trajectories difficult to track. A series of images showing the movements of the particles after flowing EG into the cell is shown in Figure 3.3E-G. The impact of flowing EG into the cell on the number of particles in the viewing area becomes obvious when the number of particles and clusters of particles in the viewing area is plotted vs. time (Figure 3.3H). As Fig. 3.3H shows, the number of particles and clusters of particles rapidly drops once EG flows to the liquid cell, dropping by 50% over the course of ~25 s after being stable for 125 s.

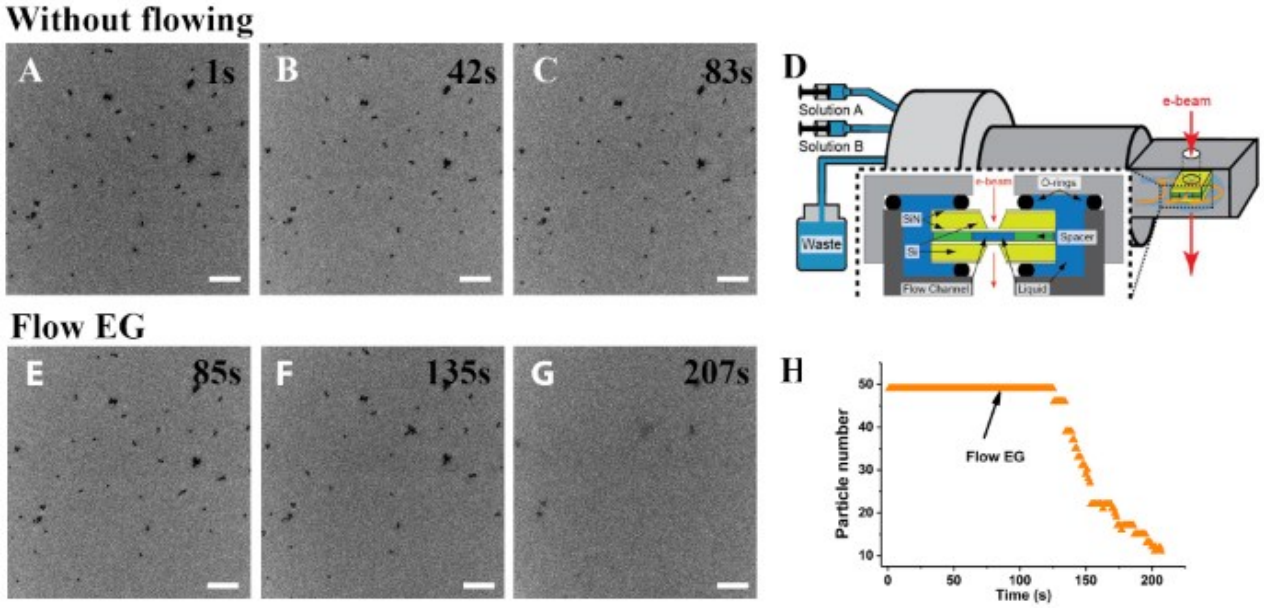

Figure 3.3. Flowing ethylene glycol (EG) into the fluid cell to control the mobility of CTAB coated gold particles. Accelerating voltage: 4500 V; beam current: 0.9 nA; dose rate: 10.0 e/nm^2/s. (A-C) Without flowing EG, the gold nanoparticles are immobile. (D) Liquid flow holders combine separate fluid lines into a single solution stream near the inlet to the cell. Solution flows through a

channel patterned in the liquid cell and around the outside of the cell. (Inset) Liquid flow cell components are pressed together by O-rings which provide a vacuum-tight seal [109]. Permission from Elsevier. (E-G) Fast movement of gold nanoparticles is activated by the injection of EG, which can dissolve the CTAB surfactant layer, and facilitate particle movement. (H) Time dependence of the number of particles in the viewing area.

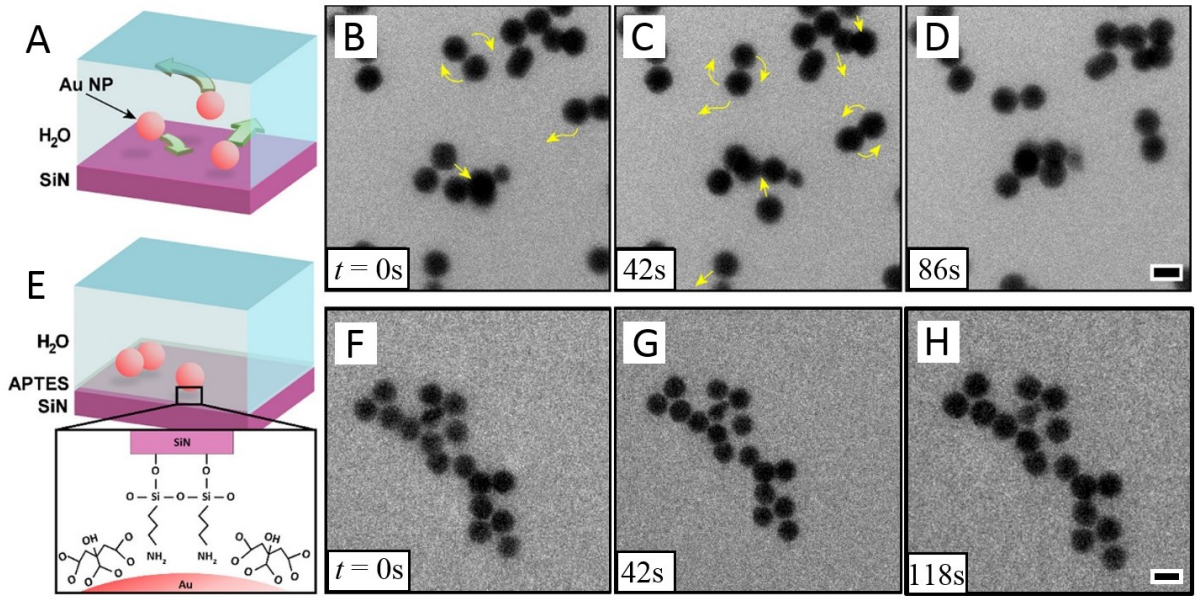

Figure 3.4. (A) Schematic of a standard liquid cell chamber containing citrate stabilized Au nanoparticles in water. (B-D) LP-TEM images of mobile Au nanoparticles (~40 nm diameter) contained between non-treated silicon nitride windows at a dose rate of 5.9×10^3 e nm^{-2} s^{-1}. (E) Schematic of a liquid cell chamber with an APTES monolayer coating one of the SiN membranes. The positive amino groups strongly interact with the negatively charged Au nanoparticles by charge-charge interaction, immobilizing them on the coated SiN. (F-H) LP-TEM images of static Au nanoparticles (~25 nm diameter) fixed by APTES functionalization to the SiN at the same dose rate as in B-D. Scale bars are 50 nm.

We attribute the initial immobilization to a strong interaction between the (hydrophilic) CTAB-coated particles and the SiN windows. Flow of EG led to desorption of the particles from the windows, likely due to dissolution of some of the CTAB from the surface of the gold particles. However, a previous study concluded that, upon exposure to the electron beam, SiN membranes will repel positively charged nanoparticles, raising the possibility that some reduction of particle adhesion may be a consequence of membrane charging. Nonetheless, the introduction EG is likely the main driver of desorption because, at the low electron dose rates used in the experiments (10

$e \bullet nm^{-2}s^{-2}$), no particle desorption was observed in the absence of EG. Thus the results reported here demonstrate that by flowing EG into the liquid cell, the initially immobile CTAB coated gold particles desorb from the window and become mobile for studies of particle dynamics. Because most nanoparticle systems are typically stabilized by surface ligands, this approach to achieving mobility may be broadly applicable, enabling investigation of particle assembly dynamics at electron beam dose rates that are too low to trigger particle release from the membranes.

While achieving release of nanoparticles is important for studying particle aggregation and assembly dynamics, there are also many instances in which particles need to be immobilized to observe their evolution over time [110]. Chemical functionalization of the LP-phase SiN windows is another method that has been used to prevent the adhesion of nanoparticles to the liquid phase windows [47, 105, 111]. We recently showed that this approach can also be used to achieve robust nanoparticle immobilization [105]. Negatively charged citrate stabilized Au nanoparticles were drop-cast on silanized SiN windows and then mounted into the liquid-cell holder along with an opposing SiN window and deionized water. The mobility of APTES immobilized Au nanoparticles was compared to that of Au nanoparticles in water between two non-treated SiN windows (Figure 3.4 A-D). For the case of non-treated windows, the Au particles initially stuck to the windows, however they were observed to move freely under the electron beam, as indicated by the yellow arrows, and could detach from the window. In contrast, Au nanoparticles on the APTES treated window (Figure 3.4 E-H) were observed to stay immobile over extended imaging times at moderate beam current densities.

While studies of nanoparticle assembly by LP-TEM require particles to be mobile, immobilization is preferred for studies of growth, dissolution and phase transformation. Even in the case where assembly dynamics is the focus of experiments, an ability to release or immobilize

particles at will allows assembly to be triggered only when the appropriate imaging conditions have been established. On the flip side, the ability to immobilize the particles enables high resolution imaging of structure when diffusion rates in the released state are too fast to allow for such imaging. The effects discussed here created by introducing EG and by functionalizing the SiN membranes with APTES demonstrates two distinct strategies for controlling nanoparticle mobility. Additives that act as solvents to remove ligands from the particles enable the timed release of the particles from the membrane even at low beam dose rates, while functionalization of the membranes with monolayers that strongly bind the particles ensures robust adhesion even at high dose rates. Taken together, these strategies add to the toolbox of methods for targeting LP-TEM experiments towards data that depends on the state of particle mobility.

3.3.4 *Impurity effects and the importance of post-mortem analyses*

Impurities in the fluid cell, even at very low levels, can interfere with LP-TEM studies. The impurities can be either directly reduced by the electrons, leading to their precipitation or reaction with the sample, or act as an additive to influence the progression of the targeted phenomenon. Impurities can come from residue left on the tip of the holder, which is often shared by multiple users for several different materials systems. For example, we observed the growth of gold nanoparticles under a large dose rate of 937 e/nm2/s, (Figure 3.5A) in solutions that only consisted of iron nitrate and sodium hydroxide. (The gold nanoparticles were identified by performing ex-situ analyses using HRTEM and EDX mapping (Figure 3.5B and C). The gold impurity probably comes from residue left on the inlet of the holder following numerous in situ studies of gold formation. While quantitative investigations into the effectiveness of particular cleaning procedures have not been reported and the cleaning procedure required will likely be material-specific, the results shown here demonstrate the importance of developing rigorous cleaning

procedures to be employed before the experiments, as well as the necessity of performing post LP-TEM analyses on samples obtained in situ, due to the higher quality of diffraction and spectroscopy data obtained ex situ.

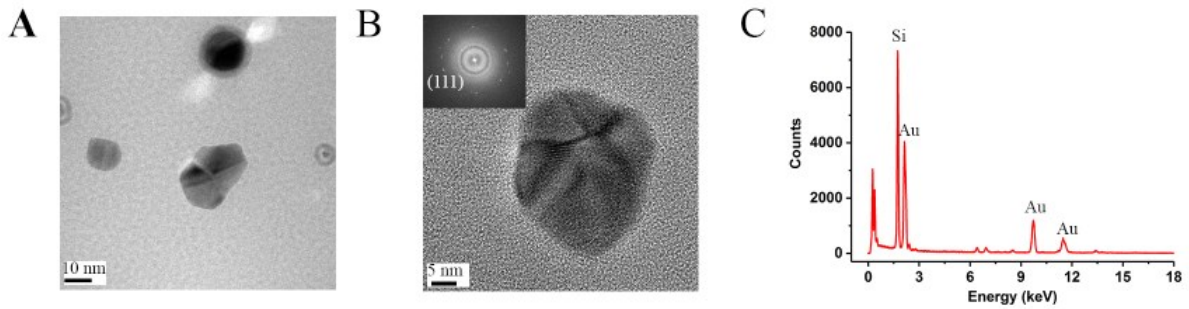

Figure 3.5. Ex situ characterization after the in situ experiments to further identify the products. Here, unexpected gold nanocrystals are formed due to impurity contamination. (A) Snapshot of gold polyhedral nanocrystal growth from an in situ LP-TEM session where only iron nitrate and sodium hydroxide are applied. (B) Post ex situ HRTEM characterization of the particle after the disassembly of the liquid phase chips. Gold (111) facets are highlighted in the fast Fourier transform (FFT). (C) EDX characterization of the particle further proves the identity of the gold nanocrystal.

3.3.5 *Heating as an alternative stimulus for driving targeted reaction*

Most of this chapter has presented examples for which the electron beam is responsible for inducing a process in LP-TEM, often with deleterious effects. Ideally, the only role of the electrons is to detect structure and dynamics via images, diffraction patterns, spectra, etc. However, many (if not most) of the phenomena studied to date by LP-TEM have been activated or accelerated by the electron beam, rendering conclusions about the natural progression of these phenomena questionable. There are three ways to address this problem. The first is to have a sufficiently quantitative understanding of the effects of electron beam irradiation on the physical and chemical state of the sample to be able to include those effects in the analysis of the data. A handful of studies have attempted to provide a quantitative understanding of the interaction between the electron beam and the sample, but the main focus has been either on defining the radiolysis

products formed in pure water [55], or on empirically determining how the rate of a targeted process, like nucleation, depends on electron beam dose rate [96]. More recently this approach has also been used to understand oxide formation [100], the influence of the solid-solution interface on the distribution of hydrolysis products [112] and the use of scavengers to minimize the beam effects [99, 113]. A lack of detailed knowledge about the impact of the beam on interfacial solution structure, the production and annihilation of species in samples with complex chemistries (e.g., iron oxide solutions), or the activation barriers and transition rate coefficients make this approach difficult to institute in a general manner.

The second approach is to identify model systems for which the inherent kinetics are sufficiently fast and insensitive to the beam that low dose imaging techniques (e.g., the beam is blocked most of the time and is only applied to the sample periodically) can be found for which beam effects are negligible [106]. The third approach is to apply a quantifiable external stimulus that activates the process of interest at a rate far beyond that produced by the beam such as flowing reactive reagents into the cell [12, 57], or heating the solution in the liquid cell to drive a thermally activated process [58], that is otherwise inaccessible on experimental timescales, even with the electron beam. In all cases, varying the microscope parameters like dose rate, accelerating voltage, frequency of beam-blocking and imaging mode, is important for understanding of the influence of the beam on the phenomenon of interest.

Heating provides an important stimulus for the activation of processes of interest in LP-TEM experiments. In many cases involving nucleation, growth, assembly or transformation of nanoparticles, the observed phenomena are more representative of processes occurring outside the liquid cell, because colloidal synthesis procedures often require elevated temperatures. However, very few LP-TEM studies involving heating have been reported due to the technical challenges

associated with heating the liquid layer in the TEM [58, 106]. There are two ways to perform heating LP-TEM. One is to combine a glue sealed liquid cell (Figure 3.6A) with a traditional heating holder, the other is to apply heating microchips in a specific liquid holder (Figure 3.6B). Here we illustrate the use of the latter approach by observing the reversible control of bubble dynamics through precise control of the temperature in the liquid cell. (The temperature in the liquid cell was determined from the calibration curve for heater resistance vs. temperature provided by the manufacturer.)

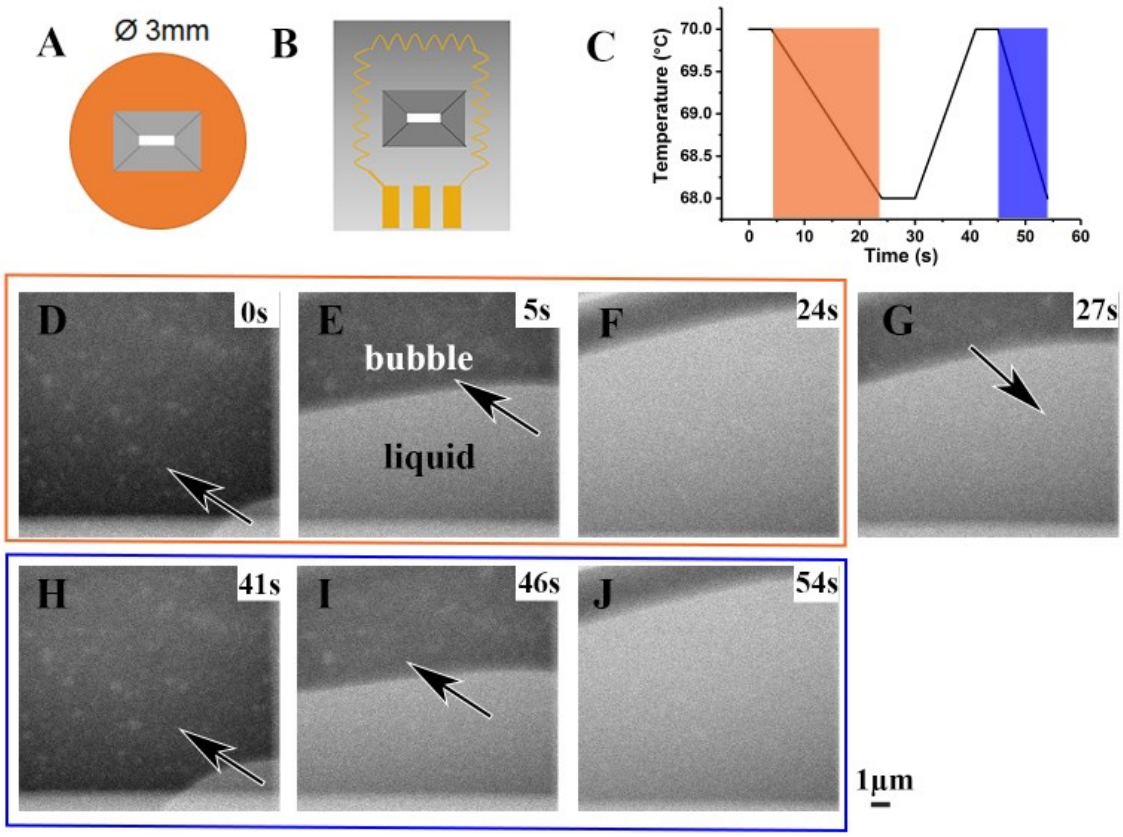

Figure 3.6. Two different configurations for LP-TEM heating experiments. (A) A liquid cell sealed with vacuum compatible glue having dimensions similar to that of a normal TEM grid [114]. We combine this with a Gatan heating holder to perform in-situ heating experiments. (B) A resistively heated microchip with the resistors and electrodes located on the bottom silicon wafer [106]. (C) Temperature vs. time for the bubble dynamics experiment in D-J. The response of the bubbles to heating is fast and robust. (D-J) STEM observation of bubble response to the temperature change shown in (C). Specifically, (D-F) shows bubble shrinkage due to a temperature drop from 70 to 68 °C. (F-G) shows the expansion of the bubble due to the temperature increase from 68 to 70 °C,

while (H-J) shows a similar progression to that seen in (D-F). STEM mode was used due to its negligible influence on the bubble dynamics in this experiment.

Bubble formation is very common in solutions undergoing heating due to the lowered solubility of air in water, as well as by exposure of water to an electron beam. We observed the shrinkage of bubbles created either by initial heating or the electron beam when we lowered the temperature from 70 to 68 °C (Figure 3.6D-F). The likely reason for this effect is that, when the temperature dropped, the gas in the bubble began to dissolve into the liquid, which led to the shrinkage of the bubble. And when the temperature was then increased from 68 to 70 °C, the bubble expanded, and pushed the liquid to the corner of the cell (Figure 3.6F-G). When the temperature was then lowered back to 68 °C, the bubble immediately shrank again due to the rapid temperature change. The corresponding temperature/time curve is shown in Figure 3.6C. In previous studies, control over bubble dynamics by variations in electron beam intensity was reported [48-49]. Here, the precise change of temperature provides the control mechanism.

3.3.6 *Thoughts on replication challenge in liquid phase TEM*

Another challenge in LP-TEM is the experimental difficulties to replicate certain experimental results. It all comes down to the technical design of the system. First, liquid thickness is difficult to control in the experiment. Usually we use 100nm spacer chip, so ideally the thickness of the liquid should be about 100nm all over the observation area. In reality, the thickness can be affected by the assembly (particles in the solution and dusts can change the thickness of the original spacing), bulging of the window, bubble formation (bubble formation could lead to an ultrathin liquid layer to enable atomic resolution). A schematic in Figure 3.7 illustrates the formation of a big bubble inside the chamber and the bulging of the windows, which lead to various regions of

different liquid thickness. A rigorous SiN window assembly and solution filtering can minimize the influence of dust and particles in the solution on the thickness of the liquid.

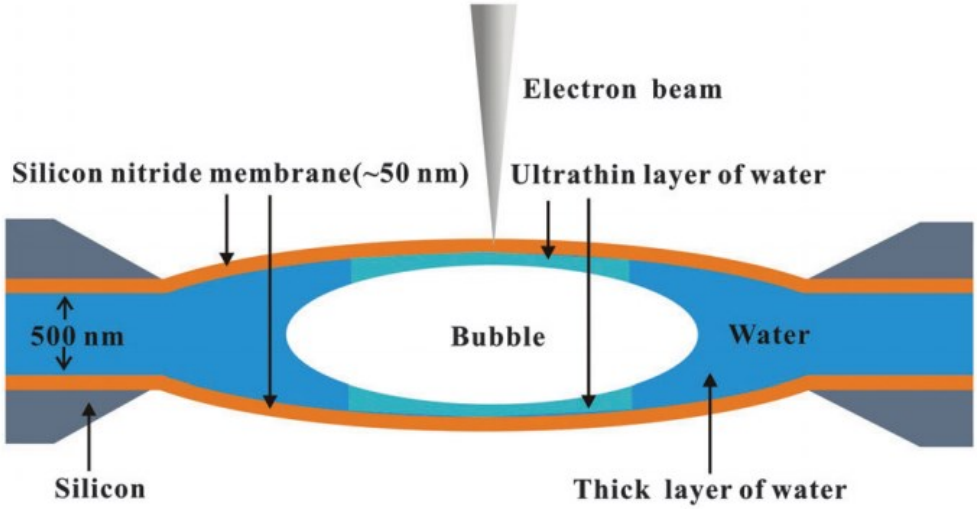

Figure 3.7. Cross-sectional schematic of the assembled chips with liquid enclosed. Liquid (water) is sealed within two SiN membranes, which are highlighted in yellow color. The formation the bubble and the bulging leads to various liquid thickness. The electron beam will pass through the SiN window and liquid, and potentially bubble.

Second, nature of solution/SiN window interface is not known and difficult to control. Most of the phenomena of interest happens close to the solid/solution interface. Many reports have demonstrated the drastically reduced mobility of particles in the LP-TEM due to the mitigation of the interface on the particle mobility. The SiN window is the most widely used material in the LP-TEM, and usually plasmon cleaned before loading the solution. So the surface chemistry of the SiN window before and after plasmon cleaning might play a big role on changing the solution/window interface, and therefore influence the system. New window materials might be needed to compare with the results from the SiN window. In addition, complementary techniques like AFM and spectroscopy are needed to probe the nature and influence of the window/solution interface on the system.

Third, electron beam effects on the system. This has been discussed a lot in the literature, while some of the researchers take the e beam as an input, which mimics the role of other stimulus in the ex situ studies, others try to minimize the beam effects as much as possible to achieve “beam-free” results. We think both are legitimate approaches. Regarding the aforementioned approach utilizing e beam, we think it is also important to separate the influence by the radiation chemistry and beam sample interaction. Many works have been reported on the difference of the phenomena inside the beam irradiation area vs. outside irradiation area. We know there is a gradient of the radicals between irradiation area and non-irradiation area. So a careful study of the results outside the irradiation area is important in distinguishing the role of beam sample interaction and radical chemistry. The later might be easier comparable to ex-situ solution chemistry. The e beam effect can be coupled with the window/solution interface and liquid thickness, making it challenging to control the parameters. So regarding the approach of utilizing e beam, a rigorous control over windows, liquid thickness, and some other parameters like (irradiation history, evaporation of the liquid during the assembly, etc) is critical in replication of the experiments.

3.4 Conclusion

In situ LP-TEM has emerged as a powerful tool for mechanistic investigations of a wide range of processes and materials impacting multiple fields. However, there are still many technical challenges associated with this technique. Here we highlighted several common challenges associated with LP-TEM including beam induced growth, dissolution, particle mobility and aggregation, the effects of impurity contamination and replication challenges. A range of methods were applied to better control the processes of interest occurring during LP-TEM, including modifying the solution and/or window chemistry, applying flow during LP-TEM, performing post characterization on the samples, and driving targeted phenomena through controlled heating. The

results of these and other studies illustrate the potential that LP-TEM offers for future impactful research through careful cell design, modifications of surface and solution chemistry, controls over purity, and introduction of external stimuli to drive targeted processes.

Chapter 4. Structure and properties of Hm Mesocrystal

The above-mentioned is the majority of my PhD study, which is to gain fundamental insight on the growth mechanism of mesocrystal. In addition, I will give two preliminary examples of applying in situ TEM to link the properties of the material to the microstructure of the material. Together, my long-term vision is to explore the synthesis-structure-property (SSP) relationship of material by applying and developing novel TEM related techniques.

4.1 Dissolution in Hm mesocrystal vs. rhom Hm

Dissolution is ubiquitous in the world including weathering, corrosion, material degrading, drug releasing and crystallization. To understand the fundamentals of dissolution is important in designing corrosion resistant materials and understanding crystallization. However, little is known about the dissolution details in the atomic scale. Here I will apply in situ LPTEM at certain solution chemistry condition to directly probe the dynamics of dissolution at nm scale.

I first synthesized Hm particles with two different structures, of which, rhom Hematite has a rhombohedral shape with smooth surface (Figure 4.1a). Its electron diffraction (Figure 4.1b) has a sharp diffraction peak (Figure 4.1b inserted) indicates good crystallinity, which is further verified by high resolution TEM (Figure 4.1c) and STEM (Figure 4.1d). The other one is spindle Hm mesocrystal, which has a porous structure consisting of primary particles as building blocks shown in the STEM imaging (Figure 4.1e). Its elongated electron diffraction patterns (same zone axis of [24-1] as compared to rhom Hm) (Figure 4.1f) suggest the misorientation of the building blocks. We further apply HRTEM (Figure 4.1g) and HRSTEM (Figure 4.1h) to characterize the atomic structure of the mesocrystal, which shows continuous lattice match but with slight misorientation

between particles. A line dislocation is highlighted in Figure 4.1h. The very distinct contrast in the STEM image suggests the existence of nanopores inside the mesocrystal (Figure 4.1h).

By applying in situ LPTEM, we investigated the dissolution dynamics of rhom Hm and Hm mesocrystal. The dissolution of two connected rhom Hm particles in Figure 4.1i showcases a typical classic dissolution behavior, in which edge dissolves faster than face, and particle becomes rounder overtime until fully dissolved. The hollow structure inside the rhom Hm might origin from defects, which dissolves faster and contribute to the contrast. In comparison, the Hm mesocrystal dissolves preferentially over certain area and transitions to a dendritic skeleton. Surprising Rod-like structure is manifested over the dissolution, and rod-like structure persists in the end until fully dissolved in the end (Figure 4.1j).

Since the dissolution position reflects chemical activity of the material, the anisotropic dissolution behaviors of the Hm mesocrystal suggests the hierarchical nature of the spindle. By mapping out the sequence of the dissolution, we are able to map out the chemical activity of the hierarchical structure. In addition, the detailed analyses of the image show that primary particle will detach from each other and led to acceleration of the dissolution (not shown here). Overall, we have shown there that by applying in situ LPTEM we are able to directly investigate the dynamics of the dissolution behavior of rhom Hm vs. Hm mesocrystal. Their distinctive dissolution behavior was rationalized by detailed characterization of their microstructure (not shown here).

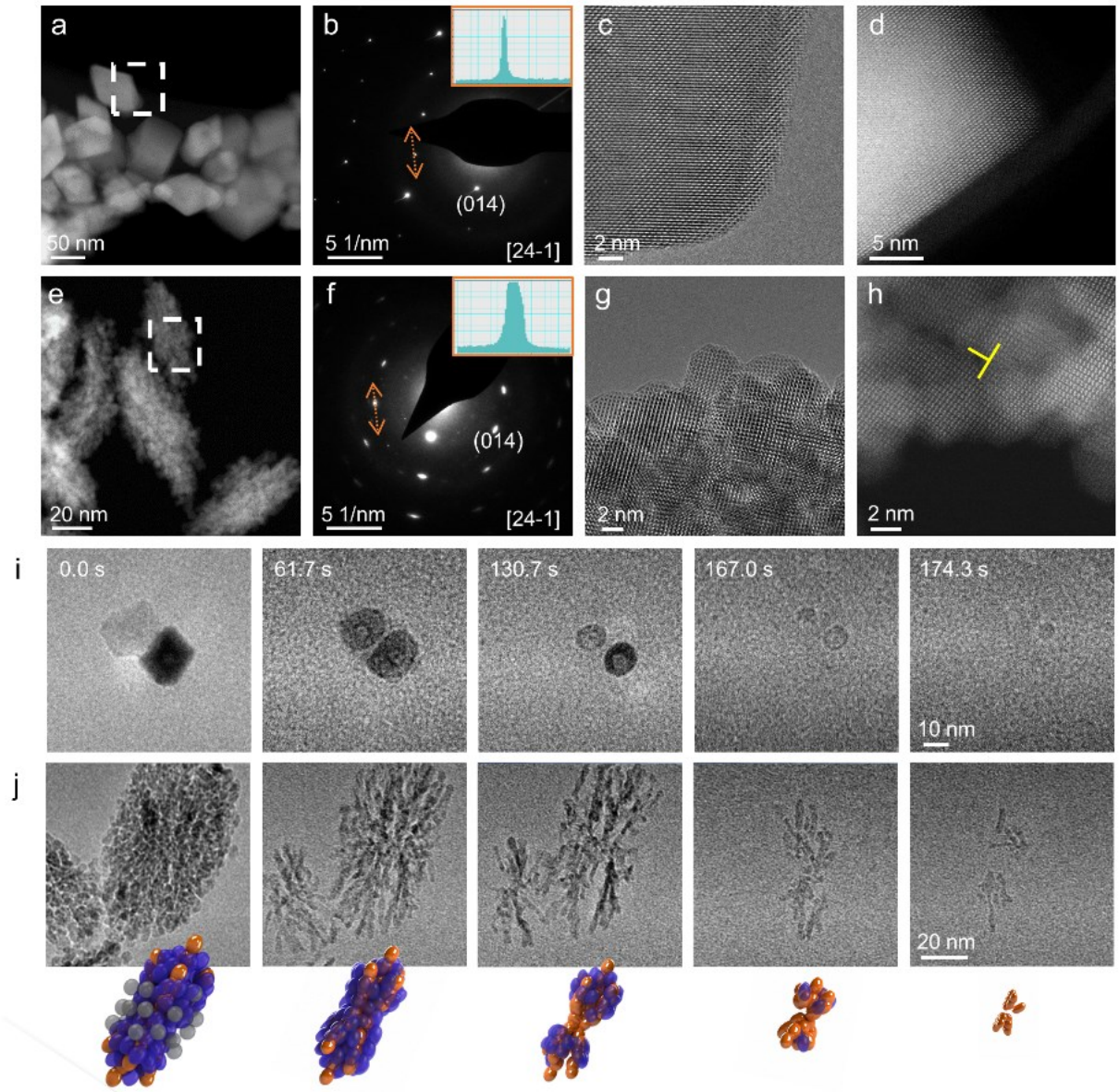

Figure 4.1. Structural Difference of rhom Hm and spindle Hm mesocrystal and their different dissolution behavior. a, e, Low magnification STEM image of rhom Hm and Hm mesocrystal. b, f, corresponding electron diffraction of rhom Hm and Hm mesocrystal at same zone axis in a and e, which is highlighted by the dashed square. c, g, HRTEM image of rhom Hm and Hm mesocrystal. d, h, HRSTEM image of rhom Hm and Hm mesocrystal. Line dislocation was highlighted in h. Comparison of a-d and e-h manifests that rhom Hm has a higher crystallinity with a smooth surface, while Hm mesocrystal consists of primary particles, and there is a mismatch between particles. i, sequential TEM images of the dissolution of rhom Hm at low pH. The particle rounded up and shrank over time until total dissolution. j, sequential TEM images of the dissolution of Hm mesocrystal. As highlighted by the cartoon, certain parts of the spindle preferentially dissolve and left with a skeleton made of rod like structure.

4.2 Deformation in Hm mesocrystal vs. rhom Hm

Deformation is the change of an object's shape due to the application of a force. It is an important engineering characteristic of the mechanic strength of a material. Here we will use in situ TEM-STM, which will allow us to manipulate a tungsten needle at sub angstrom precision to compress rhom Hm and Hm mesocrystal to gain insights on their deformation mechanism. We first loaded the rhom Hm particle on a substrate (Figure 4.2a, the top part is the substrate). We then compressed the Hm by manipulating the STM probe (bottom part of the figure a-e) towards the rhom Hm. Extra mass accumulated on the surface during the deformation as highlighted by the arrow in c-e and h. The final compressed Hm is still a single crystal shown by the insert FFT in image h.

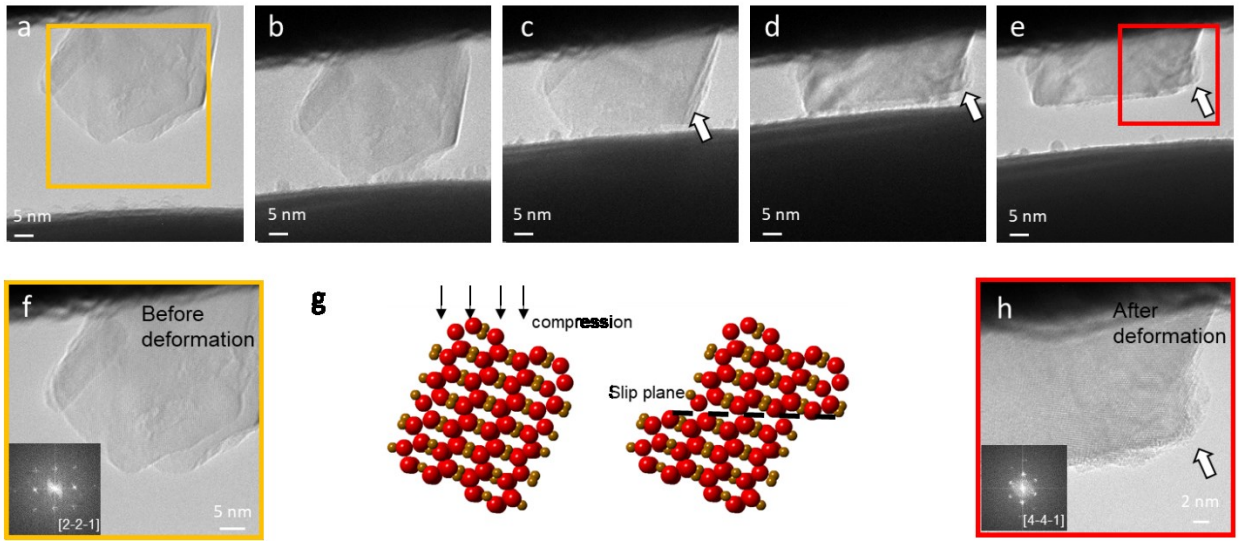

Figure 4.2. Deformation of rhom Hm in the TEM. a-e sequential TEM images of the rhom Hm plastic deformation by utilizing a TEM-STM in situ holder. f, TEM image of the beginning of the rhom Hm demonstrating its single crystalline nature (inserted, FFT). g, schematic of the deformation process through motion of dislocation and slip plane. h, TEM image of the rhom Hm after deformation, still showing single crystalline nature. Extra Hm mass was transferred to the surface as indicated by the arrow during the deformation.

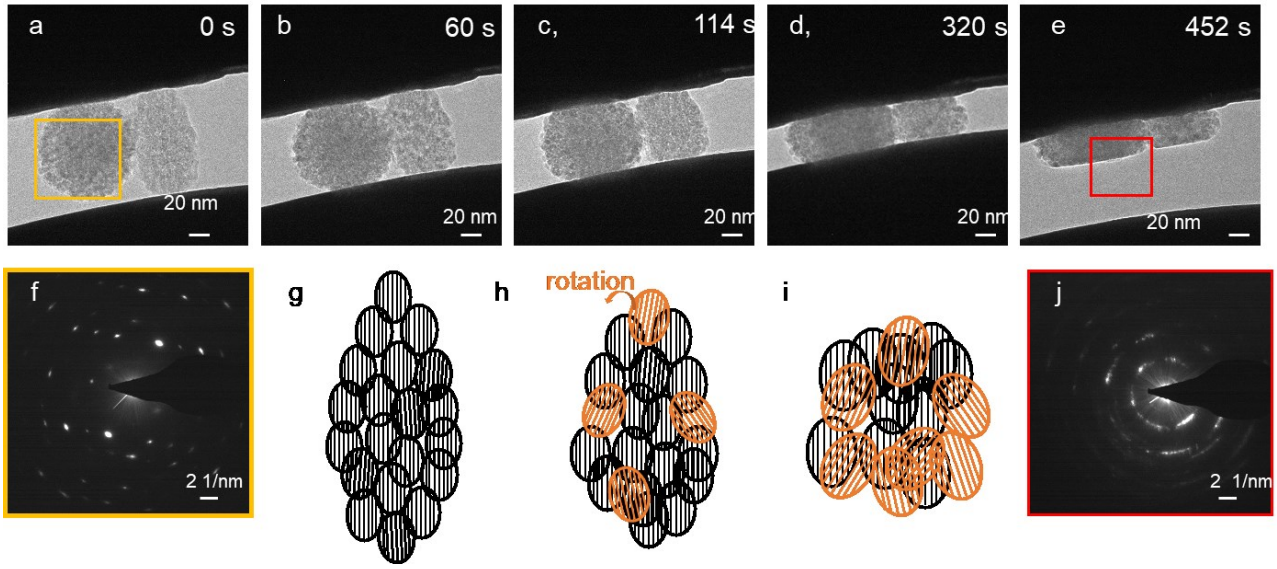

Figure 4.3. Deformation of Hm mesocrystal in the TEM. a-e, sequential TEM images of plastic deformation process of the Hm mesocrystal. f, ED pattern of the Hm mesocrystal, from the area which is highlighted in a yellow box in image a. g-i, schematic of the particle rotation during the deformation. j, ED of the Hm mesocrystal after deformation, showing the change from single crystal to polycrystal after deformation

For comparison, we loaded Hm mesocrystal on the substrate and compressed it by manipulating the STM probe (Figure 4.3a). Similarly the mesocrystal underwent a plastic deformation, leading to the dramatic shape change from a spindle to a plate (Figure 4.3a-e). However, ED pattern (Figure 4.3j) shows that the deformed structure becomes polycrystalline. This suggests that the deformation has some other mechanism in addition to the conventional dislocation and slip plane movement. Guessing from the structure of the spindle, which comprise of primary particles connecting each other with necks. The rotation of those particles may be significant during the deformation, thereby leading to the polycrystalline transformation.

Chapter 5. Summary and outlook

5.1 Summary

In my PhD, I focused on utilizing primarily TEM techniques, especially in situ heating LPTEM, to understand crystallization mechanism of mesocrystal. In situ techniques are indispensable to the investigation of crystallization pathway. Through a combination of in situ and ex situ TEM, we find that the primary phase, Fh, dissolves into the solution to provide solutes for the Hm formation. Hm grows from solution rather than directly from Fh. Hm grows through preferentially nucleation a few nms away from the Hm/solution interface, and then attach to the Hm seed particle through oriented attachment. The gap of the nuclei and the seed is about 2nm. The result is rationalized by simulation and ATR-FTIR which conclude that there is a gradient of Fe ions close to the Hm/solution interface. It is this chemical difference close to the Hm/solution interface that drives the preferential nucleation in this region. The collective findings reported here converge on an important new pathway of CPA that resolves some key questions about mesocrystal formation. This proposed pathway may be able to account for many occurrences of mesocrystal formation.

In situ LPTEM, as a distinct technique in facilitating our understanding of fundamentals has its own limitation, especially regarding the concern of beam effects. I have tried new methods to validate the results, such as applying different beam mode and parameters, applying other stimuli such as heating, and blocking the beam. We anticipate that it would provide more insight in material synthesis, electrochemistry, catalyst and biology in the near future.

5.2 Outlook

We need new materials and structures with diverse properties to meet the challenge of the world with rising demand on clean energy, computing, infectious disease, pollution and climate change. My vision is to gain fundamental insights about material synthesis (crystallization) and its synthesis-structure-property (SSP) relationship, which lay the fundamental to speed up new material syntheses with unique structure and exceptional properties in various fields. TEM and in situ TEM have been evolving constantly and combined with new technological advancement in computational science and detector technology, they will continue playing tremendous roles in fundamental insight into material science and engineering. I aim to utilize and develop in situ (microscopy) methods to understand the pathway of material synthesis and their SSP relationship.

Appendix A

Publications

1. **Zhu, G.**, Sushko, M., Loring, J., Legg, B., Song, M., Solits, J., Huang, X. P., Rosso, K. , de Yoreo, J., 2020, ***Nature***, in press.
2. **Zhu, G.**, De Yoreo, J.J., et al. Direct observation of dissolution by particle detachment. *in prep.*
3. **Zhu, G.**, Reiner, H., Cölfen, H. and De Yoreo, J.J., 2019. Addressing some of the technical challenges associated with liquid phase S/TEM studies of particle nucleation, growth and assembly. ***Micron***, *118*, pp.35-42.
4. Robertson, A.W.,* **Zhu, G.**,* Mehdi, B.L., Jacobs, R.M., De Yoreo, J. and Browning, N.D., 2018. Nanoparticle immobilization for controllable experiments in liquid-cell transmission electron microscopy. ***ACS applied materials & interfaces***, *10*(26), pp.22801-22808.
5. Cheng, Y., Tao, J., **Zhu, G.,** Soltis, J.A., Legg, B.A., Nakouzi, E., De Yoreo, J.J., Sushko, M.L. and Liu, J., 2018. Near surface nucleation and particle mediated growth of colloidal Au nanocrystals. ***Nanoscale***, *10*(25), pp.11907-11912.
6. **Zhu, G.**, Solits, J., Tao, J., Legg, B., Wang, C. and de Yoreo, J., 2018. Alternate Path to the Formation of Co-aligned Hierarchical Mesocrystals. *APS*, *2018*, pp.C13-009.
7. Bard, A.B., Zhou, X., Xia, X., **Zhu, G.,** Lim, M.B., Kim, S.M., Johnson, M.C., Kollman, J.M., Marcus, M.A., Spurgeon, S.R. and Perea, D.E., 2020. A Mechanistic Understanding of Nonclassical Crystal Growth in Hydrothermally Synthesized Sodium Yttrium Fluoride Nanowires. ***Chemistry of Materials***, *32*(7), pp.2753-2763.
8. Jiang, Y., **Zhu, G.,** Dong, G., Lin, F., Zhang, H., Yuan, J., Zhang, Z. and Jin, C., 2017. Probing the oxidative etching induced dissolution of palladium nanocrystals in solution by liquid cell transmission electron microscopy. ***Micron***, *97*, pp.22-28.
9. Kim, S.J., Mahmood, J., Kim, C., Han, G.F., Kim, S.W., Jung, S.M., **Zhu, G.,** De Yoreo, J.J., Kim, G. and Baek, J.B., 2018. Defect-free encapsulation of Fe0 in 2D fused organic networks as a durable oxygen reduction electrocatalyst. ***Journal of the American Chemical Society***, *140*(5), pp.1737-1742.

10. Song, J., Xiao, D., Jia, H., **Zhu, G.,** Engelhard, M., Xiao, B., Feng, S., Li, D., Reed, D., Sprenkle, V.L. and Lin, Y., 2019. A comparative study of pomegranate Sb@ C yolk–shell microspheres as Li and Na-ion battery anodes. ***Nanoscale***, *11*(1), pp.348-355.
11. Liang, X., Post, J.E., Lanson, B., Wang, X., Zhu, M., Liu, F., Tan, W., Feng, X., **Zhu, G.,** Zhang, X. and De Yoreo, J.J., 2020. Coupled morphological and structural evolution of δ-MnO 2 to α-MnO2 through multistage oriented assembly processes: the role of Mn (iii). ***Environmental Science: Nano***, *7*(1), pp.238-249.
12. De Siena, M.C., Creutz, S.E., Regan, A., Malinowski, P., Jiang, Q., Kluherz, K.T., **Zhu, G.,** Lin, Z., De Yoreo, J.J., Xu, X. and Chu, J.H., 2020. Two-Dimensional van der Waals Nanoplatelets with Robust Ferromagnetism. ***Nano Letters***, 20(3), pp.2100-2106.

Academic activities

1. **Co-chair**, 2021, Gordon Research Conference Seminar (GRS) on *Crystal Growth and Assembly,* June 19-20, Southern New Hampshire University.
2. **Co-chair**, 2020, Symposium on *Clay Mineral Nucleation, Crystallization, and Aggregation*. 57th CMS conference, Oct. 18-23, Richland, Pacific Northwest National Laboratory.
3. **Co-chair**, 2018, Symposium on *Biomineralization & Biocompatible Minerals*, 255th ACS conference, Mar. 18-22, New Orleans.
4. MRS University Chapter member, University of Washington.

VITA

I am Guomin Zhu, born in Hangzhou, China. I obtained my master's degree in Materials Science and Engineering with a specialty in transmission electron microscopy (TEM) at Zhejiang University, China. Afterward, I decided to pursue my career in the United States. I spent my first PhD year on courses/languages at University of Washington (UW) campus in Seattle. Studying at UW has been so joyful a period that I sincerely appreciated it and will always remember those days filled with joy and adventures. Afterward, I moved to Pacific Northwest National Laboratory (PNNL), which is located in a small town called Richland in the east of Washington. Compared to universities, national labs have more resources and more focused on team project. I have been involved in several projects, but mainly focusing on my PhD project, which is to understand Hematite mesocrystal formation. Working in PNNL has been an uplifting and productive experience for me.

BIBLIOGRAPHY

1. De Yoreo, J. J.; Gilbert, P. U.; Sommerdijk, N. A.; Penn, R. L.; Whitelam, S.; Joester, D.; Zhang, H.; Rimer, J. D.; Navrotsky, A.; Banfield, J. F.; Wallace, A. F.; Michel, F. M.; Meldrum, F. C.; Colfen, H.; Dove, P. M., CRYSTAL GROWTH. Crystallization by particle attachment in synthetic, biogenic, and geologic environments. *Science* **2015,** *349* (6247), aaa6760.

2. Sturm , E. V.; Cölfen, H., Mesocrystals: Past, Presence, Future. *Crystals* **2017,** *7* (7), 207.

3. Cho, K. S.; Talapin, D. V.; Gaschler, W.; Murray, C. B., Designing PbSe nanowires and nanorings through oriented attachment of nanoparticles. *J Am Chem Soc* **2005,** *127* (19), 7140-7.

4. Yang, J.; Zeng, Z.; Kang, J.; Betzler, S.; Czarnik, C.; Zhang, X.; Ophus, C.; Yu, C.; Bustillo, K.; Pan, M.; Qiu, J.; Wang, L. W.; Zheng, H., Formation of two-dimensional transition metal oxide nanosheets with nanoparticles as intermediates. *Nat Mater* **2019,** *18* (9), 970-976.

5. Whitham, K.; Yang, J.; Savitzky, B. H.; Kourkoutis, L. F.; Wise, F.; Hanrath, T., Charge transport and localization in atomically coherent quantum dot solids. *Nat Mater* **2016,** *15* (5), 557-63.

6. Boneschanscher, M. P.; Evers, W. H.; Geuchies, J. J.; Altantzis, T.; Goris, B.; Rabouw, F. T.; van Rossum, S. A.; van der Zant, H. S.; Siebbeles, L. D.; Van Tendeloo, G.; Swart, I.; Hilhorst, J.; Petukhov, A. V.; Bals, S.; Vanmaekelbergh, D., Long-range orientation and atomic attachment of nanocrystals in 2D honeycomb superlattices. *Science* **2014,** *344* (6190), 1377-80.

7. Banfield, J. F.; Welch, S. A.; Zhang, H.; Ebert, T. T.; Penn, R. L., Aggregation-based crystal growth and microstructure development in natural iron oxyhydroxide biomineralization products. *Science* **2000,** *289* (5480), 751-4.

8. Penn, R. L.; Banfield, J. F., Imperfect oriented attachment: dislocation generation in defect-free nanocrystals. *Science* **1998,** *281* (5379), 969-71.

9. Colfen, H.; Antonietti, M., Mesocrystals and nonclassical crystallization. **2008**.

10. Li, D.; Nielsen, M. H.; Lee, J. R.; Frandsen, C.; Banfield, J. F.; De Yoreo, J. J., Direction-specific interactions control crystal growth by oriented attachment. *Science* **2012,** *336* (6084), 1014-8.

11. Yin, Y.; Alivisatos, A. P., Colloidal nanocrystal synthesis and the organic-inorganic interface. *Nature* **2005,** *437* (7059), 664-70.

12. Nielsen, M. H.; Aloni, S.; De Yoreo, J. J., In situ TEM imaging of CaCO(3) nucleation reveals coexistence of direct and indirect pathways. *Science* **2014,** *345* (6201), 1158-62.

13. Wang, Z. L., Transmission Electron Microscopy of Shape-Controlled Nanocrystals and Their Assemblies. *The Journal of Physical Chemistry B* **2000,** *104* (6), 1153-1175.

14. Thanh, N. T.; Maclean, N.; Mahiddine, S., Mechanisms of nucleation and growth of nanoparticles in solution. *Chemical reviews* **2014,** *114* (15), 7610-30.

15. De Yoreo, J. J., Principles of Crystal Nucleation and Growth. *Reviews in Mineralogy and Geochemistry* **2003,** *54* (1), 57-93.

16. Tao, J.; Fijneman, A.; Wan, J.; Prajapati, S.; Mukherjee, K.; Fernandez-Martinez, A.; Moradian-Oldak, J.; De Yoreo, J. J., Control of Calcium Phosphate Nucleation and Transformation through Interactions of Enamelin and Amelogenin Exhibits the "Goldilocks Effect". *Cryst Growth Des* **2018,** *18* (12), 7391-7400.

17. Van Driessche, A. E. S.; Sazaki, G.; Otálora, F.; González-Rico, F. M.; Dold, P.; Tsukamoto, K.; Nakajima, K., Direct and Noninvasive Observation of Two-Dimensional Nucleation Behavior of Protein Crystals by Advanced Optical Microscopy. *Crystal Growth & Design* **2007,** *7* (10), 1980-1987.

18. Ihli, J.; Wong, W. C.; Noel, E. H.; Kim, Y.-Y.; Kulak, A. N.; Christenson, H. K.; Duer, M. J.; Meldrum, F. C., Dehydration and crystallization of amorphous calcium carbonate in solution and in air. *Nature Communications* **2014,** *5*, 3169.

19. Michel, F. M.; Ehm, L.; Antao, S. M.; Lee, P. L.; Chupas, P. J.; Liu, G.; Strongin, D. R.; Schoonen, M. A.; Phillips, B. L.; Parise, J. B., The structure of ferrihydrite, a nanocrystalline material. *Science* **2007,** *316* (5832), 1726-9.

20. Legg, B. A.; De Yoreo, J. J., The energetics of prenucleation clusters in lattice solutions. *J Chem Phys* **2016,** *145* (21), 211921.

21. Habraken, W. J.; Tao, J.; Brylka, L. J.; Friedrich, H.; Bertinetti, L.; Schenk, A. S.; Verch, A.; Dmitrovic, V.; Bomans, P. H.; Frederik, P. M.; Laven, J.; van der Schoot, P.; Aichmayer, B.; de With, G.; DeYoreo, J. J.; Sommerdijk, N. A., Ion-association complexes unite classical and non-classical theories for the biomimetic nucleation of calcium phosphate. *Nat Commun* **2013,** *4*, 1507.

22. Beniash, E.; Aizenberg, J.; Addadi, L.; Weiner, S., Amorphous calcium carbonate transforms into calcite during sea urchin larval spicule growth. *Proceedings of the Royal Society of London. Series B: Biological Sciences* **1997,** *264* (1380), 461-465.

23. Gong, Y. U.; Killian, C. E.; Olson, I. C.; Appathurai, N. P.; Amasino, A. L.; Martin, M. C.; Holt, L. J.; Wilt, F. H.; Gilbert, P. U., Phase transitions in biogenic amorphous calcium carbonate. *Proc Natl Acad Sci U S A* **2012,** *109* (16), 6088-93.

24. Mahamid, J.; Sharir, A.; Addadi, L.; Weiner, S., Amorphous calcium phosphate is a major component of the forming fin bones of zebrafish: Indications for an amorphous precursor phase. *Proc Natl Acad Sci U S A* **2008,** *105* (35), 12748-53.

25. Killian, C. E.; Metzler, R. A.; Gong, Y. U.; Olson, I. C.; Aizenberg, J.; Politi, Y.; Wilt, F. H.; Scholl, A.; Young, A.; Doran, A.; Kunz, M.; Tamura, N.; Coppersmith, S. N.; Gilbert, P. U., Mechanism of calcite co-orientation in the sea urchin tooth. *J Am Chem Soc* **2009,** *131* (51), 18404-9.

26. Dillaman, R.; Hequembourg, S.; Gay, M., Early pattern of calcification in the dorsal carapace of the blue crab, Callinectes sapidus. *J Morphol* **2005,** *263* (3), 356-74.

27. Baumgartner, J.; Dey, A.; Bomans, P. H.; Le Coadou, C.; Fratzl, P.; Sommerdijk, N. A.; Faivre, D., Nucleation and growth of magnetite from solution. *Nat Mater* **2013,** *12* (4), 310-4.

28. Penn, R. L.; Banfield, J. F., Morphology development and crystal growth in nanocrystalline aggregates under hydrothermal conditions: insights from titania. *Geochimica et Cosmochimica Acta* **1999,** *63* (10), 1549-1557.

29. Penn, R. L.; Soltis, J. A., Characterizing crystal growth by oriented aggregation. *CrystEngComm* **2014,** *16* (8), 1409.

30. Liao, H. G.; Cui, L.; Whitelam, S.; Zheng, H., Real-time imaging of Pt3Fe nanorod growth in solution. *Science* **2012,** *336* (6084), 1011-4.

31. Sturm Nee Rosseeva, E. V.; Colfen, H., Mesocrystals: structural and morphogenetic aspects. *Chem Soc Rev* **2016,** *45* (21), 5821-5833.

32. Kim, Y. Y.; Schenk, A. S.; Ihli, J.; Kulak, A. N.; Hetherington, N. B.; Tang, C. C.; Schmahl, W. W.; Griesshaber, E.; Hyett, G.; Meldrum, F. C., A critical analysis of calcium carbonate mesocrystals. *Nat Commun* **2014,** *5*, 4341.

33. Smeets, P. J. M.; Cho, K. R.; Sommerdijk, N. A. J. M.; De Yoreo, J. J., A Mesocrystal-Like Morphology Formed by Classical Polymer-Mediated Crystal Growth. *Advanced Functional Materials* **2017,** *27* (40), 1701658.

34. Ruska, E., The emergence of the electron microscope: Connection between Realization and First Patent Application, Documents of an Invention. *Journal of Ultrastructure and Molecular Structure Research* **1986,** *95* (1), 3-28.

35. Williams, D. B.; Carter, C. B., The Transmission Electron Microscope. **1996**, 3-17.

36. Kim, J. S.; Lagrange, T.; Reed, B. W.; Taheri, M. L.; Armstrong, M. R.; King, W. E.; Browning, N. D.; Campbell, G. H., Imaging of transient structures using nanosecond in situ TEM. *Science* **2008,** *321* (5895), 1472-5.

37. Taheri, M. L.; Stach, E. A.; Arslan, I.; Crozier, P. A.; Kabius, B. C.; LaGrange, T.; Minor, A. M.; Takeda, S.; Tanase, M.; Wagner, J. B.; Sharma, R., Current status and future directions for in situ transmission electron microscopy. *Ultramicroscopy* **2016,** *170*, 86-95.

38. Ross, F. M.; Minor, A. M., In Situ Transmission Electron Microscopy. **2019**, 101-187.

39. de Jonge, N.; Ross, F. M., Electron microscopy of specimens in liquid. *Nat Nanotechnol* **2011,** *6* (11), 695-704.

40. Ross, F. M., Opportunities and challenges in liquid cell electron microscopy. *Science* **2015,** *350* (6267), aaa9886.

41. Zheng, H.; Smith, R. K.; Jun, Y. W.; Kisielowski, C.; Dahmen, U.; Alivisatos, A. P., Observation of single colloidal platinum nanocrystal growth trajectories. *Science* **2009,** *324* (5932), 1309-12.

42. Jiang, Y.; Zhu, G.; Lin, F.; Zhang, H.; Jin, C.; Yuan, J.; Yang, D.; Zhang, Z., In situ study of oxidative etching of palladium nanocrystals by liquid cell electron microscopy. *Nano Lett* **2014,** *14* (7), 3761-5.

43. Ye, X.; Jones, M. R.; Frechette, L. B.; Chen, Q.; Powers, A. S.; Ercius, P.; Dunn, G.; Rotskoff, G. M.; Nguyen, S. C.; Adiga, V. P.; Zettl, A.; Rabani, E.; Geissler, P. L.; Alivisatos, A. P., Single-particle mapping of nonequilibrium nanocrystal transformations. *Science* **2016,** *354* (6314), 874-877.

44. Jiang, Y.; Zhu, G.; Dong, G.; Lin, F.; Zhang, H.; Yuan, J.; Zhang, Z.; Jin, C., Probing the oxidative etching induced dissolution of palladium nanocrystals in solution by liquid cell transmission electron microscopy. *Micron* **2017,** *97*, 22-28.

45. Tan, S. F.; Raj, S.; Bisht, G.; Annadata, H. V.; Nijhuis, C. A.; Kral, P.; Mirsaidov, U., Nanoparticle Interactions Guided by Shape-Dependent Hydrophobic Forces. *Adv Mater* **2018,** *30* (16), e1707077.

46. Liao, H. G.; Zheng, H., Liquid cell transmission electron microscopy study of platinum iron nanocrystal growth and shape evolution. *J Am Chem Soc* **2013,** *135* (13), 5038-43.

47. Chen, Q.; Cho, H.; Manthiram, K.; Yoshida, M.; Ye, X.; Alivisatos, A. P., Interaction Potentials of Anisotropic Nanocrystals from the Trajectory Sampling of Particle Motion using in Situ Liquid Phase Transmission Electron Microscopy. *ACS Cent Sci* **2015,** *1* (1), 33-9.

48. Vance, J. R.; Dillon, S. J., Thermally driven bubble evolution at a heater wire in water characterized by high-speed transmission electron microscopy. *Chem Commun (Camb)* **2017,** *53* (36), 4930-4933.

49. Shin, D.; Park, J. B.; Kim, Y. J.; Kim, S. J.; Kang, J. H.; Lee, B.; Cho, S. P.; Hong, B. H.; Novoselov, K. S., Growth dynamics and gas transport mechanism of nanobubbles in graphene liquid cells. *Nat Commun* **2015,** *6*, 6068.

50. Mehdi, B. L.; Qian, J.; Nasybulin, E.; Park, C.; Welch, D. A.; Faller, R.; Mehta, H.; Henderson, W. A.; Xu, W.; Wang, C. M.; Evans, J. E.; Liu, J.; Zhang, J. G.; Mueller, K. T.; Browning, N. D., Observation and quantification of nanoscale processes in lithium batteries by operando electrochemical (S)TEM. *Nano Lett* **2015,** *15* (3), 2168-73.

51. Chen, X.; Noh, K. W.; Wen, J. G.; Dillon, S. J., In situ electrochemical wet cell transmission electron microscopy characterization of solid–liquid interactions between Ni and aqueous NiCl2. *Acta Materialia* **2012,** *60* (1), 192-198.

52. de Jonge, N.; Peckys, D. B.; Kremers, G. J.; Piston, D. W., Electron microscopy of whole cells in liquid with nanometer resolution. *Proc Natl Acad Sci U S A* **2009,** *106* (7), 2159-64.

53. Mirsaidov, U. M.; Zheng, H.; Casana, Y.; Matsudaira, P., Imaging protein structure in water at 2.7 nm resolution by transmission electron microscopy. *Biophys J* **2012,** *102* (4), L15-7.

54. Zhu, G.; Jiang, Y.; Huang, W.; Zhang, H.; Lin, F.; Jin, C., Atomic resolution liquid-cell transmission electron microscopy investigations of the dynamics of nanoparticles in ultrathin liquids. *Chem Commun (Camb)* **2013,** *49* (93), 10944-6.

55. Schneider, N. M.; Norton, M. M.; Mendel, B. J.; Grogan, J. M.; Ross, F. M.; Bau, H. H., Electron–Water Interactions and Implications for Liquid Cell Electron Microscopy. *The Journal of Physical Chemistry C* **2014,** *118* (38), 22373-22382.

56. Grogan, J. M.; Schneider, N. M.; Ross, F. M.; Bau, H. H., Bubble and pattern formation in liquid induced by an electron beam. *Nano Lett* **2014,** *14* (1), 359-64.

57. Smeets, P. J.; Cho, K. R.; Kempen, R. G.; Sommerdijk, N. A.; De Yoreo, J. J., Calcium carbonate nucleation driven by ion binding in a biomimetic matrix revealed by in situ electron microscopy. *Nat Mater* **2015,** *14* (4), 394-9.

58. Chee, S. W.; Tan, S. F.; Baraissov, Z.; Bosman, M.; Mirsaidov, U., Direct observation of the nanoscale Kirkendall effect during galvanic replacement reactions. *Nat Commun* **2017,** *8* (1), 1224.

59. Sposito, G., Scaling invariance of the von Smoluchowski rate law. *Colloids and Surfaces A: Physicochemical and Engineering Aspects* **1997,** *120* (1), 101-110.

60. Van Driessche, A. E.; Benning, L. G.; Rodriguez-Blanco, J. D.; Ossorio, M.; Bots, P.; Garcia-Ruiz, J. M., The role and implications of bassanite as a stable precursor phase to gypsum precipitation. *Science* **2012,** *336* (6077), 69-72.

61. Yuwono, V. M.; Burrows, N. D.; Soltis, J. A.; Penn, R. L., Oriented aggregation: formation and transformation of mesocrystal intermediates revealed. *J Am Chem Soc* **2010,** *132* (7), 2163-5.

62. Navrotsky, A.; Mazeina, L.; Majzlan, J., Size-driven structural and thermodynamic complexity in iron oxides. *Science* **2008,** *319* (5870), 1635-8.

63. Boles, M. A.; Engel, M.; Talapin, D. V., Self-Assembly of Colloidal Nanocrystals: From Intricate Structures to Functional Materials. *Chem Rev* **2016,** *116* (18), 11220-89.

64. Cornell, R. M.; Schwertmann, U., The iron oxides: structure, properties, reactions, occurences and uses, second edition. **2003**.

65. Fischer, W. R., The Formation of Hematite from Amorphous Iron(III)Hydroxide. *Clays and Clay Minerals* **1975,** *23* (1), 33-37.

66. Frandsen, C.; Legg, B. A.; Comolli, L. R.; Zhang, H.; Gilbert, B.; Johnson, E.; Banfield, J. F., Aggregation-induced growth and transformation of β-FeOOH nanorods to micron-sized α-Fe2O3spindles. *CrystEngComm* **2014,** *16* (8), 1451-1458.

67. Sugimoto, T.; Itoh, H.; Mochida, T., Shape Control of Monodisperse Hematite Particles by Organic Additives in the Gel-Sol System. *J Colloid Interface Sci* **1998,** *205* (1), 42-52.

68. Graustein, W. C.; Cromack, K., Jr.; Sollins, P., Calcium oxalate: occurrence in soils and effect on nutrient and geochemical cycles. *Science* **1977,** *198* (4323), 1252-4.

69. Schwertmann, U.; Cornell, R. M., Iron Oxides in the Laboratory. **2000**.

70. Lin, X.; Heaney, P.; E. Post, J., Iridescence in Metamorphic "Rainbow" Hematite. *Gems & Gemology* **2018,** *54*.

71. Frandsen, C.; Legg, B. A.; Comolli, L. R.; Zhang, H.; Gilbert, B.; Johnson, E.; Banfield, J. F., Aggregation-induced growth and transformation of β-FeOOH nanorods to micron-sized α-Fe2O3 spindles. *CrystEngComm* **2014,** *16* (8), 1451-1458.

72. Schwertmann, U.; Cornell, R. M., Iron Oxides in the Laboraory: Preparation and Characterization **2000**.

73. Sugimoto, T.; Muramatsu, A.; Sakata, K.; Shindo, D., Characterization of Hematite Particles of Different Shapes. *Journal of Colloid and Interface Science* **1993,** *158* (2), 420-428.

74. Soltis, J. A.; Feinberg, J. M.; Gilbert, B.; Penn, R. L., Phase Transformation and Particle-Mediated Growth in the Formation of Hematite from 2-Line Ferrihydrite. *Crystal Growth & Design* **2016,** *16* (2), 922-932.

75. Zhu, G.; Reiner, H.; Colfen, H.; De Yoreo, J. J., Addressing some of the technical challenges associated with liquid phase S/TEM studies of particle nucleation, growth and assembly. *Micron* **2019,** *118*, 35-42.

76. Huang, X.; Hou, X.; Song, F.; Zhao, J.; Zhang, L., Ascorbate Induced Facet Dependent Reductive Dissolution of Hematite Nanocrystals. *The Journal of Physical Chemistry C* **2017,** *121* (2), 1113-1121.

77. Loring, J. S.; Simanova, A. A.; Persson, P., Highly mobile iron pool from a dissolution-readsorption process. *Langmuir* **2008,** *24* (14), 7054-7.

78. Sushko, M. L.; Rosso, K. M., The origin of facet selectivity and alignment in anatase TiO2 nanoparticles in electrolyte solutions: implications for oriented attachment in metal oxides. *Nanoscale* **2016,** *8* (47), 19714-19725.

79. Meng, D.; Zheng, B.; Lin, G.; Sushko, M. L., Numerical Solution of 3D Poisson-Nernst-Planck Equations Coupled with Classical Density Functional Theory for Modeling Ion and Electron Transport in a Confined Environment. *Communications in Computational Physics* **2014,** *16* (5), 1298-1322.

80. Zhang, X.; He, Y.; Sushko, M. L.; Liu, J.; Luo, L.; De Yoreo, J. J.; Mao, S. X.; Wang, C.; Rosso, K. M., Direction-specific van der Waals attraction between rutile TiO2 nanocrystals. *Science* **2017,** *356* (6336), 434-437.

81. Nielsen, M. H.; Li, D.; Zhang, H.; Aloni, S.; Han, T. Y.-J.; Frandsen, C.; Seto, J.; Banfield, J. F.; Cölfen, H.; De Yoreo, J. J., Investigating Processes of Nanocrystal Formation and Transformation via Liquid Cell TEM. *Microscopy and Microanalysis* **2014,** *20* (2), 425-436.

82. Lee, S. O.; Tran, T.; Jung, B. H.; Kim, S. J.; Kim, M. J., Dissolution of iron oxide using oxalic acid. *Hydrometallurgy* **2007,** *87* (3-4), 91-99.

83. Zhang, Y.; Kallay, N.; Matijevic, E., Interaction of metal hydrous oxides with chelating agents. 7. Hematite-oxalic acid and -citric acid systems. *Langmuir* **1985,** *1* (2), 201-206.

84. Situm, A.; Rahman, M. A.; Allen, N.; Kabengi, N.; Al-Abadleh, H. A., ATR-FTIR and Flow Microcalorimetry Studies on the Initial Binding Kinetics of Arsenicals at the Organic–Hematite Interface. *The Journal of Physical Chemistry A* **2017,** *121* (30), 5569-5579.

85. Stefansson, A., Iron (III) hydrolysis and solubility at 25 degrees C. *Environ Sci Technol* **2007,** *41* (17), 6117-23.

86. Elhadj, S.; Chernov, A. A.; De Yoreo, J. J., Solvent-mediated repair and patterning of surfaces by AFM. *Nanotechnology* **2008,** *19* (10), 105304.

87. Deng, N.; Stack, A. G.; Weber, J.; Cao, B.; De Yoreo, J. J.; Hu, Y., Organic-mineral interfacial chemistry drives heterogeneous nucleation of Sr-rich (Ba x , Sr1-x)SO4 from undersaturated solution. *Proc Natl Acad Sci U S A* **2019,** *116* (27), 13221-13226.

88. Jin, B.; Sushko, M. L.; Liu, Z.; Jin, C.; Tang, R., In Situ Liquid Cell TEM Reveals Bridge-Induced Contact and Fusion of Au Nanocrystals in Aqueous Solution. *Nano Lett* **2018,** *18* (10), 6551-6556.

89. Zhang, Z.; Sun, H.; Shao, X.; Li, D.; Yu, H.; Han, M., Three-Dimensionally Oriented Aggregation of a Few Hundred Nanoparticles into Monocrystalline Architectures. *Advanced Materials* **2005,** *17* (1), 42-47.

90. Ye, J.; Liu, W.; Cai, J.; Chen, S.; Zhao, X.; Zhou, H.; Qi, L., Nanoporous anatase TiO2 mesocrystals: additive-free synthesis, remarkable crystalline-phase stability, and improved lithium insertion behavior. *J Am Chem Soc* **2011,** *133* (4), 933-40.

91. Egglseder, M. S.; Cruden, A. R.; Tomkins, A. G.; Wilson, S. A.; Dalstra, H. J.; Rielli, A.; Li, C.; Baumgartner, J.; Faivre, D., Tiny particles building huge ore deposits – Particle-based crystallisation in banded iron formation-hosted iron ore deposits (Hamersley Province, Australia). *Ore Geology Reviews* **2019,** *104*, 160-174.

92. Cheng, Y.; Tao, J.; Zhu, G.; Soltis, J. A.; Legg, B. A.; Nakouzi, E.; De Yoreo, J. J.; Sushko, M. L.; Liu, J., Near surface nucleation and particle mediated growth of colloidal Au nanocrystals. *Nanoscale* **2018,** *10* (25), 11907-11912.

93. Laramy, C. R.; Fong, L.-K.; Jones, M. R.; O'Brien, M. N.; Schatz, G. C.; Mirkin, C. A., Understanding nanoparticle-mediated nucleation pathways of anisotropic nanoparticles. *Chemical Physics Letters* **2017,** *683*, 389-392.

94. Anand, R. R.; Gilkes, R. J., Variations in the properties of iron oxides within individual specimens of lateritic duricrust. *Soil Research* **1987,** *25* (3), 287-302.

95. De Yoreo, J. J.; Sommerdijk, N. A. J. M., Investigating materials formation with liquid-phase and cryogenic TEM. *Nat Rev Mater* **2016,** *1* (8), 16305.

96. Woehl, T. J.; Evans, J. E.; Arslan, I.; Ristenpart, W. D.; Browning, N. D., Direct in situ determination of the mechanisms controlling nanoparticle nucleation and growth. *ACS Nano* **2012,** *6* (10), 8599-610.

97. Patterson, J. P.; Abellan, P.; Denny, M. S., Jr.; Park, C.; Browning, N. D.; Cohen, S. M.; Evans, J. E.; Gianneschi, N. C., Observing the growth of metal-organic frameworks by in situ liquid cell transmission electron microscopy. *J Am Chem Soc* **2015,** *137* (23), 7322-8.

98. Yuk, J. M.; Park, J.; Ercius, P.; Kim, K.; Hellebusch, D. J.; Crommie, M. F.; Lee, J. Y.; Zettl, A.; Alivisatos, A. P., High-Resolution EM of Colloidal Nanocrystal Growth Using Graphene Liquid Cells. *Science* **2012,** *336* (6077), 61-64.

99. Woehl, T. J.; Jungjohann, K. L.; Evans, J. E.; Arslan, I.; Ristenpart, W. D.; Browning, N. D., Experimental procedures to mitigate electron beam induced artifacts during in situ fluid imaging of nanomaterials. *Ultramicroscopy* **2013,** *127*, 53-63.

100. Abellan, P.; Woehl, T. J.; Parent, L. R.; Browning, N. D.; Evans, J. E.; Arslan, I., Factors influencing quantitative liquid (scanning) transmission electron microscopy. *Chem Commun (Camb)* **2014,** *50* (38), 4873-80.

101. Parent, L. R.; Bakalis, E.; Proetto, M.; Li, Y. W.; Park, C.; Zerbetto, F.; Gianneschi, N. C., Tackling the Challenges of Dynamic Experiments Using Liquid-Cell Transmission Electron Microscopy. *Accounts Chem Res* **2018,** *51* (1), 3-11.

102. Sugimoto, T.; Wang, Y.; Itoh, H.; Muramatsu, A., Systematic control of size, shape and internal structure of monodisperse α-Fe2O3 particles. *Colloids and Surfaces A: Physicochemical and Engineering Aspects* **1998,** *134* (3), 265-279.

103. Frens, G., Controlled Nucleation for the Regulation of the Particle Size in Monodisperse Gold Suspensions. *Nature Physical Science* **1973,** *241* (105), 20-22.

104. Jana, N. R.; Gearheart, L.; Murphy, C. J., Wet Chemical Synthesis of High Aspect Ratio Cylindrical Gold Nanorods. *The Journal of Physical Chemistry B* **2001,** *105* (19), 4065-4067.

105. Robertson, A. W.; Zhu, G.; Mehdi, B. L.; Jacobs, R. M. J.; De Yoreo, J.; Browning, N. D., Nanoparticle Immobilization for Controllable Experiments in Liquid-Cell Transmission Electron Microscopy. *ACS Appl Mater Interfaces* **2018,** *10* (26), 22801-22808.

106. Smith, B. J.; Parent, L. R.; Overholts, A. C.; Beaucage, P. A.; Bisbey, R. P.; Chavez, A. D.; Hwang, N.; Park, C.; Evans, A. M.; Gianneschi, N. C.; Dichtel, W. R., Colloidal Covalent Organic Frameworks. *ACS Cent Sci* **2017,** *3* (1), 58-65.

107. Lu, Y.; Geng, J.; Wang, K.; Zhang, W.; Ding, W.; Zhang, Z.; Xie, S.; Dai, H.; Chen, F. R.; Sui, M., Modifying Surface Chemistry of Metal Oxides for Boosting Dissolution Kinetics in Water by Liquid Cell Electron Microscopy. *ACS Nano* **2017,** *11* (8), 8018-8025.

108. Schwertmann, U., Solubility and Dissolution of Iron-Oxides. *Plant and Soil* **1991,** *130* (1-2), 1-25.

109. Tao, J.; Nielsen, M. H.; De Yoreo, J. J., Nucleation and phase transformation pathways in electrolyte solutions investigated by in situ microscopy techniques. *Current Opinion in Colloid & Interface Science* **2018,** *34*, 74-88.

110. Gilmore, L. B.; Tanner, R. J.; McKell, O. A.; Boudreaux, E. C.; Dukes, J. M.; McDonald, M. S.; Kelly, F. D., Molecular Surveillance of Viral Processes Using Silicon Nitride Membranes. *Micromachines* **2013,** *4* (1).

111. Liu, Y.; Lin, X. M.; Sun, Y.; Rajh, T., In situ visualization of self-assembly of charged gold nanoparticles. *J Am Chem Soc* **2013,** *135* (10), 3764-7.

112. Gupta, T.; Schneider, N. M.; Park, J. H.; Steingart, D.; Ross, F. M., Spatially dependent dose rate in liquid cell transmission electron microscopy. *Nanoscale* **2018,** *10* (16), 7702-7710.

113. Sutter, E.; Jungjohann, K.; Bliznakov, S.; Courty, A.; Maisonhaute, E.; Tenney, S.; Sutter, P., In situ liquid-cell electron microscopy of silver-palladium galvanic replacement reactions on silver nanoparticles. *Nat Commun* **2014,** *5*, 4946.

114. Hong, Y. J.; Tai, L. A.; Chen, H. J.; Chang, P.; Yang, C. S.; Yew, T. R., Stable water layers on solid surfaces. *Phys Chem Chem Phys* **2016,** *18* (8), 5905-9.